Magma Genesis, Degassing, and Mixing in Rifts and Arcs

by

Thomas R. Hudgins

A dissertation submitted in partial fulfillment
of the requirements for the degree of
Doctor of Philosophy
(Geology)
in the University of Michigan
2015

Doctoral Committee:

Associate Professor Adam C. Simon, Chair
Professor Kristina I. Håkansson
Professor Rebecca A. Lange
Research Scientist Gordon Moore

ACKNOWLEDGEMENTS

I would like to thank my advisor, Adam Simon, for his continuing support and mentorship throughout the three years we have worked together. He has helped shape my views of igneous petrology and geochemistry from rifts to arcs to ore deposits. I could not have accomplished any of what is presented here without his continuous support, financial and intellectual, and the numerous opportunities to travel and present this research at conferences. I am honored to have been accepted into his research group and to have been allowed to grow as an academic under his supervision. I would also like to thank Sam Mukasa for my initiation into a PhD program, as well as the exciting research opportunities presented in my first two years at the University of Michigan. During these two years I learned a great deal about how to ask the right questions, develop research goals, and see them through. I owe many thanks to Gordon Moore for our conversations about anything igneous, which provided a great deal of expansion of my own ideas. I also have learned more about analytical methods talking to and teaching under Gordon than I ever did by using the instruments. I would like to thank Becky Lange for always challenging my views and assumptions, providing me with new outlooks and perspectives on ideas that I thought I understood. Thanks to my committee, Gordon, Becky, and Kicki Håkansson, for their countless hours of defense and dissertation discussion, as well as working with me to get everything done on time.

I owe thanks and so much more to Laura Waters for our countless discussions, all of which provided new insight and perspectives on geochemistry and petrology, for improving my ability to conduct research, and for being an incredible friend. Thanks to Udo Becker for many

interesting conversations about potential career paths, publishing advice, and other topics unrelated to academia; to the past and current members of my extended research group: Chris Stefano, Stephen Crabtree, Laura Waters, Laura Bilenker, Adrian Fiege, Jaayke Knipping, Liz Tanis, Brian Konecke, Tristan Childress, Xiaofei Pu, James Jolles, Sean Hurt, Daniel Korfeh; to the staff members who seem to keep this crazy department functioning, Anne Hudon and Bill Wilcox.

I owe a special thanks to my family, who have put up with me and supported me in all of my endeavors, no matter how ridiculous; to Meghan Taylor for being a source of joy, inspiration, support, and so much more for the past four years; to my officemates who have made this office incredibly enjoyable: Laura Waters, Tim Gallagher, James Jolles, Peng Ni; and to the incredible group of friends that this entire department has been. Thank you all so much.

TABLE OF CONTENTS

LIST OF FIGURES

LIST OF TABLES

LIST OF APPENDICES

CHAPTER I

INTRODUCTION

1.1. VOLATILES IN RIFT ENVIRONMENTS

The significance of inclusions within individual crystals in providing information about the petrogenesis of igneous rocks has been understood since the pioneering work of Sorby (1858), over one hundred years before analyses of these inclusions began to make an impact in the community. By the 1920's it was apparent that magmas contained some volatile (H_2O, CO_2, Cl, F, S) component and Bowen (1928) understood the need to quantify the effects of volatiles in magma as well as measure the volatiles in a magma, stating, "To many petrologists a volatile component is exactly like a Maxwell demon; it does just what one may wish it to do." Some of the first measurements of melt inclusions were done in the 1970's (Roedder and Weiblen 1970; Anderson 1974a; Anderson 1974b; Roedder 1979), however, due to the difficulty of analyzing volatiles in melt inclusions, it was only within the past two decades that melt inclusion analyses became commonplace. As it is clear that volatiles play a large role in magma genesis, efforts have been made to quantify the volatile contents of the mantle by investigating the storage capacity of nominally anhydrous mineral phases (Beran and Libowitzky 2006; Skogby 2006), the stability of hydrous phases in the mantle (Frost 2006; Foley et al 2009; Green 2015), the nature of mantle metasomatism (Roden and Murthy 1985; Wilshire 1987; Rosenthal et al 2009), as well as the composition of fluid inclusions in mantle xenoliths (Andersen and Neumann,

2001; Frezzotti et al., 2012). Of particular focus in this dissertation is the ability for mantle metasomes to store volatiles.

It is well understood that the generation of silica-undersaturated alkaline lavas requires a metasomatized mantle source that is rich in H_2O and CO_2 (Brey and Green 1975; Menzies and Murthy 1980; Spera 1981; Roden and Murthy 1985; Edgar 1987; Foley 1992; Pilet et al 2008; Foley et al 2009; Green 2015). These metasomes can often have a phase assemblage involving amphibole or phlogopite, hydrous minerals acting as a reservoir for water, and may also be veined with carbonate (Foley 1988; Foley 1992; Rosenthal et al 2009; Kessel et al 2015). The generation of these metasomes is not well understood, with hypotheses including carbonatitic low-degree partial melts of the mantle at ~300 km (Dasgupta and Hirschmann 2006), fluids and/or sediments melts from subducting slabs (Tsuno and Dasgupta 2012; Rooney et al 2014), and partial melts during plume ascent at ~150 km depth (Rosenthal et al 2009; Foley et al 2009). As these metasomes can act as mantle reservoirs for volatiles, understanding their origin and stability is key to understanding the flux of volatiles into and out of the mantle. Silica-undersaturated alkaline are also often found at the propagating tips of rifts, indicating that there may be some link between metasomatism and rift initiation.

Chapter II of this dissertation investigates the major- and trace-element compositions and volatile contents of olivine hosted melt inclusions from the Western Branch of the East African Rift. The mantle beneath this portion of the rift is thought to be a phlogopite- and carbonate-bearing metasomatized mantle. The investigation of these melt inclusions provides evidence of the volatile contents of the silicate melt at the time of entrapment, which allows us to estimate the volatile contents of the initial melt, providing insight into the mantle source. The results from this study show that the melt inclusion chemistry looks very similar to rocks erupted

in arc settings rather than ocean island basalts (OIBs) or rifts, and contain far higher volatile contents than would be expected for OIBs and rifts. The concentrations of fluid-mobile elements compared to fluid-immobile elements show an enrichment in the fluid-mobile elements, similar to subduction-related magmas, that trends towards global subducted sediments (GLOSS). These data provide evidence that the metasomatism in the East African mantle may have occurred during the ~600 Ma Pan-African Orogeny, and that volatiles can be stored in the lithospheric mantle over long periods of geologic time. This chapter has been published in *Contributions to Mineralogy and Petrology 169*(5), 1-18.

1.2. PETROGENESIS IN ARC ENVIRONMENTS

Though studied for over a century, the origin of intermediate and silicic magmas remains enigmatic. Bowen (1928) demonstrated, through a series of experiments, that higher silica liquids could be formed by the crystallization and subsequent removal by settling of mineral phases. This led to the widely accepted theory of crystal fractionation, but also led to Bowen's stance during "The Granite Controversy" that granites formed by the consolidation of evolved magmas, rather than by the "granitization" of pre-existing rock (Bowen 1948; Read 1948). This controversy led to the experimental work of Tuttle and Bowen (1958) that effectively ended the granite controversy, but also demonstrated the ability to generate evolved silicate liquids by the partial melting of granitoid crust in the presence of H_2O.

Since the work of Tuttle and Bowen (1958), many experimental studies have supported the origin of evolved magmas through the partial melting of hydrous crust (Beard and Lofgren 1991; Rapp et al 1991; Coleman et al 1992; Atherton and Petford 1993; Tepper et al 1993; Rapp and Watson 1995; Lange and Carmichael 1996; Petford and Atherton 1996; Petford and Gallagher 2001; Annen et al 2006), however, the origin of intermediate to silicic magmas is still

much like the granite controversy. There is support for magma mixing being the dominant petrogenetic process (Anderson 1976; Reubi and Blundy 2009; Kent et al 2010; Kent 2013), partial melting of the mantle (Straub et al 2008), crystal fractionation (Brophy 1991; Bachmann and Bergantz 2008; MacDonald et al 2008; Dufek and Bachmann 2010). There are even disagreements on the origin of the same magma body, from crystal fractionation (Davies and Halliday 1998) to the re-melting of rhyolitic crust (Bindeman and Valley 2001). Though most would argue that all of these processes are happening somewhere, the main disagreements begin when one tries to determine the dominant process responsible for the generation of intermediate to silicic magmas.

Magma mixing has been proposed as the dominant process by which intermediate magmas are generated (Anderson 1976; Eichelberger 1978; Reubi and Blundy 2009; Kent et al 2010), and the advance of microanalytical techniques has furthered our ability to extract details on the conditions of magma chambers. Recent microanalytical evidence for magma mixing includes the observation of compositionally distinct melt inclusions in intermediate lavas (Reubi and Blundy 2009; Robertson et al 2013), chemical composition and crystal size distribution of phenocrysts in intermediate lavas (Churikova et al 2007; Salisbury et al 2008; Kent et al 2010; Neill et al 2015), and crystal residence times post-mixing by diffusion chronometry (Kent et al 2010; Till et al 2015). Though there is growing evidence of the ubiquity of magma mixing, there exist thermal and compositional barriers to mixing that question the likelihood of magma mixing being the dominant process forming intermediate magmas.

Chapter III of this dissertation examines a set of lavas erupted at Mutnovsky Volcano, Kamchatka, to investigate the petrogenesis of intermediate lavas by examining plagioclase phenocryst abundance, chemistry, and texture. The results of previous melt inclusion work

(Robertson et al 2013) and geochemical modeling (Simon et al 2014) at Mutnovsky are consistent with the formation of intermediate lavas by magma mixing. This chapter set out to see if the chemistry and texture of plagioclase was consistent with the prior melt inclusion and modeling work. Plagioclase is ideal in this regard as it can be found in lavas covering a wide range of silica content and, since plagioclase is a solid solution of anorthite ($CaAl_2Si_2O_8$) and albite ($NaAlSi_3O_8$), its composition reflects the composition of the magma it crystallized from. The results of this study demonstrate that the basaltic andesites erupted at Mutnovsky all have two chemical and textural populations of plagioclase, a euhedral and anorthite-rich population, and a sieved and anorthite-poor population. The anorthite-rich population share similar compositions with the plagioclase observed in Mutnovsky basalts, whereas the sieved, anorthite-poor population are compositionally similar to the plagioclase found in Mutnovsky dacites. We suggest that this is physical evidence of basalt and dacite mixing to form basaltic andesite, leading to the partial resorption of the dacitic plagioclase phenocrysts.

Chapter IV is an effort to quantitatively model the mixing, or lack thereof, of magmas with different temperatures, viscosities, and compositions to address the significance of thermal and compositional barriers to magma mixing. This has been previously investigated by Sparks and Marshall (1986), however many key parameters of the model could not be easily constrained, such as the degree of crystallinity, viscosity, and heat capacity. With the recent advancements in computational thermodynamics and the development of the MELTS model (Ghiorso and Sack 1995), we now have a method by which we can calculate these parameters for any composition, temperature, and pressure, providing much more insight into the properties of these magmas. In addition to this advancement, recent experimental work has quantified the ability of magmas of different viscosities to mix (Laumonier et al 2014b; Laumonier et al

2014a). By combining MELTS modeled data with these experimental results, we demonstrate a robust way to constrain the ability of compositionally and thermally distinct magmas to mix. This can be applied to any system where mixing is proposed, provided that an estimate or measurement of the proposed end-members exists.

1.3. REFERENCES

Anderson AT (1974a) Evidence for a picritic, volatile-rich magma beneath Mt. Shasta, California. J Petrol 15:243–267. doi: 10.1093/petrology/15.2.243

Anderson AT (1974b) Chlorine, sulfur, and water in Magmas and Oceans. Bull Geol Soc Am 85:1485–1492. doi: 10.1130/0016-7606(1974)85<1485:CSAWIM>2.0.CO;2

Anderson AT (1976) Magma mixing: petrological process and volcanological tool. J Volcanol Geotherm Res 1:3–33. doi: 10.1016/0377-0273(76)90016-0

Annen C, Blundy JD, Sparks RSJ (2006) The Genesis of Intermediate and Silicic Magmas in Deep Crustal Hot Zones. J Petrol 47:505–539. doi: 10.1093/petrology/egi084

Atherton MP, Petford N (1993) Generation of sodium-rich magmas from newly underplated basaltic crust. Nature 362:144–146.

Bachmann O, Bergantz GW (2008) Rhyolites and their source mushes across tectonic settings. J Petrol 49:2277–2285. doi: 10.1093/petrology/egn068

Beard JS, Lofgren GE (1991) Dehydration Melting and Water-Saturated Melting of Basaltic and Andesitic Greenstones and Amphibolites at 1, 3, and 6. 9 kb. J Petrol 32:365–401. doi: 10.1093/petrology/32.2.365

Beran A, Libowitzky E (2006) Water in Natural Mantle Minerals II: Olivine, Garnet and Accessory Minerals. Rev Mineral Geochemistry 62:169–191. doi: 10.2138/rmg.2006.62.8

Bindeman IN, Valley JW (2001) Low-delta O-18 rhyolites from Yellowstone: Magmatic evolution based on analyses of zircons and individual phenocrysts. J Petrol 42:1491–1517. doi: 10.1093/petrology/42.8.1491

Bowen NL (1928) The Evolution of the Igneous Rocks. Princeton University Press, Princeton

Bowen NL (1948) Origin of Granite. Geol Soc Am Mem 28:79–90. doi: 10.1130/MEM28

Brey G, Green D (1975) The role of CO2 in the genesis of olivine melilitite. Contrib to Mineral Petrol 103:93–103.

Brophy JG (1991) Composition gaps, critical crystallinity, and fractional crystallization in orogenic (calc-alkaline) magmatic systems. Contrib to Mineral Petrol 109:173–182. doi: 10.1007/BF00306477

Churikova T, Wörner G, Eichelberger J, Ivanov B V (2007) Minor- and Trace Element Zoning in Plagioclase from Kizimen Volcano, Kamchatka: Insights on the Magma Chamber Processes. Geophys Monogr Ser 172:303–323.

Coleman DS, Glazner a F, Frost TP (1992) Evidence from the lamarck granodiorite for rapid late cretaceous crust formation in california. Science 258:1924–1926. doi: 10.1126/science.258.5090.1924

Dasgupta R, Hirschmann MM (2006) Melting in the Earth's deep upper mantle caused by carbon dioxide. Nature 440:659–62. doi: 10.1038/nature04612

Davies GR, Halliday AN (1998) Development of the Long Valley rhyolitic magma system: Strontium and neodymium isotope evidence from glasses and individual phenocrysts. Geochim Cosmochim Acta 62:3561–3575. doi: 10.1016/S0016-7037(96)00329-8

Dufek J, Bachmann O (2010) Quantum magmatism: Magmatic compositional gaps generated by melt-crystal dynamics. Geology 38:687–690. doi: 10.1130/G30831.1

Edgar AD (1987) The genesis of alkaline magmas with emphasis on their source regions: inferences from experimental studies. Geol Soc London, Spec Publ 30:29–52. doi: 10.1144/GSL.SP.1987.030.01.04

Eichelberger JC (1978) Andesitic volcanism and crustal evolution. Nature 275:21–27. doi: 10.1038/275021a0

Foley SF (1992) Vein-plus-wall-rock melting mechanisms in the lithosphere and the origin of potassic alkaline magmas. Lithos 28:435–453.

Foley SF (1988) The Genesis of Continental Basic Alkaline Magmas— An Interpretation in Terms of Redox Melting. J Petrol Special_Vo:139–161. doi: 10.1093/petrology/Special_Volume.1.139

Foley SF, Yaxley GM, Rosenthal A, et al (2009) The composition of near-solidus melts of peridotite in the presence of CO2 and H2O between 40 and 60 kbar. Lithos 112:274–283. doi: 10.1016/j.lithos.2009.03.020

Frost DJ (2006) The Stability of Hydrous Mantle Phases. Rev Mineral Geochemistry 62:243–271. doi: 10.2138/rmg.2006.62.11

Ghiorso M, Sack R (1995) Chemical mass transfer in magmatic processes IV. A revised and internally consistent thermodynamic model for the interpolation and extrapolation of liquid-

solid equilibria in magmatic systems at elevated temperatures and pressures. Contrib to Mineral Petrol 119:197–212.

Green DH (2015) Experimental petrology of peridotites, including effects of water and carbon on melting in the Earth's upper mantle. Phys Chem Miner 42:95–122. doi: 10.1007/s00269-014-0729-2

Kent a. JR (2013) Preferential eruption of andesitic magmas: Implications for volcanic magma fluxes at convergent margins. Geol Soc London, Spec Publ 385:257–280. doi: 10.1144/SP385.10

Kent AJR, Darr C, Koleszar AM, et al (2010) Preferential eruption of andesitic magmas through recharge filtering. Nat Geosci 3:631–636. doi: 10.1038/ngeo924

Kessel R, Pettke T, Fumagalli P (2015) Melting of metasomatized peridotite at 4–6 GPa and up to 1200 °C: an experimental approach. Contrib to Mineral Petrol. doi: 10.1007/s00410-015-1132-9

Lange R, Carmichael I (1996) The Aurora volcanic field, California-Nevada: oxygen fugacity constraints on the development of andesitic magma. Contrib to Mineral Petrol 125:167–185.

Laumonier M, Scaillet B, Arbaret L, Champallier R (2014a) Experimental simulation of magma mixing at high pressure. Lithos 196-197:281–300. doi: 10.1016/j.lithos.2014.02.016

Laumonier M, Scaillet B, Pichavant M, et al (2014b) On the conditions of magma mixing and its bearing on andesite production in the crust. Nat Commun 5:1–12. doi: 10.1038/ncomms6607

MacDonald R, Belkin HE, Fitton JG, et al (2008) The roles of fractional crystallization, magma mixing, crystal mush remobilization and volatile-melt interactions in the genesis of a young basalt-peralkaline rhyolite suite, the greater Olkaria volcanic complex, Kenya Rift valley. J Petrol 49:1515–1547. doi: 10.1093/petrology/egn036

Menzies M, Murthy V (1980) Mantle metasomatism as a precursor to the genesis of alkaline magmas-isotopic evidence. Am J Sci 280-A:622–638.

Neill OK, Larsen JF, Izbekov PE, Nye CJ (2015) Pre-eruptive magma mixing and crystal transfer revealed by phenocryst and microlite compositions in basaltic andesite from the 2008 eruption of Kasatochi Island volcano. Am J Sci 100:722–737.

Petford N, Atherton MP (1996) Na-rich partial melts from newly underplated basaltic crust: the Cordillera Blanca Batholith, Peru. J Petrol 37:1491–1521. doi: 10.1093/petrology/37.6.1491

Petford N, Gallagher K (2001) Partial melting of mafic (amphibolitic) lower crust by periodic influx of basaltic magma. Earth Planet Sci Lett 193:483–499.

Pilet S, Baker M, Stolper E (2008) Metasomatized lithosphere and the origin of alkaline lavas. Science (80-) 320:916–919.

Rapp RP, Watson EB (1995) Dehydration Melting of Metabasalt at 8-32 kbar: Implications for Continental Growth and Crust-Mantle Recycling. J Petrol 36:891–931. doi: 10.1093/petrology/36.4.891

Rapp RP, Watson EB, Miller CF (1991) Partial melting of amphibolite/eclogite and the origin of Archean trondhjemites and tonalites. Precambrian Res 51:1–25. doi: 10.1016/0301-9268(91)90092-O

Read HH (1948) Origin of Granite. Geol Soc Am Mem 28:1–20. doi: 10.1130/MEM28

Reubi O, Blundy J (2009) A dearth of intermediate melts at subduction zone volcanoes and the petrogenesis of arc andesites. Nature 461:1269–73. doi: 10.1038/nature08510

Robertson K, Simon a., Pettke T, et al (2013) Melt inclusion evidence for magma evolution at Mutnovsky volcano, Kamchatka. Geofluids 13:421–439. doi: 10.1111/gfl.12060

Roden MF, Murthy VR (1985) Mantle Metasomatism. Annu Rev Earth Planet Sci 13:269–296.

Roedder E (1979) Origin and significance of magmatic inclusions. Bull Mineral 102:487–510.

Roedder E, Weiblen PW (1970) Silicate liquid immiscibility in lunar magmas, evidenced by melt inclusions in lunar rocks. Science 167:641–644. doi: 10.1126/science.167.3918.641

Rooney TO, Nelson WR, Dosso L, et al (2014) The role of continental lithosphere metasomes in the production of HIMU-like magmatism on the northeast African and Arabian plates. Geology 42:419–422. doi: 10.1130/G35216.1

Rosenthal A, Foley SF, Pearson DG, et al (2009) Petrogenesis of strongly alkaline primitive volcanic rocks at the propagating tip of the western branch of the East African Rift. Earth Planet Sci Lett 284:236–248. doi: 10.1016/j.epsl.2009.04.036

Salisbury MJ, Bohrson W a., Clynne M a., et al (2008) Multiple plagioclase crystal populations identified by crystal size distribution and in situ chemical data: Implications for timescales of magma chamber processes associated with the 1915 eruption of Lassen Peak, CA. J Petrol 49:1755–1780. doi: 10.1093/petrology/egn045

Simon A, Yogodzinski GM, Robertson K, et al (2014) Evolution and genesis of volcanic rocks from Mutnovsky Volcano, Kamchatka. J Volcanol Geotherm Res 286:116–137. doi: 10.1016/j.jvolgeores.2014.09.003

Skogby H (2006) Water in Natural Mantle Minerals I: Pyroxenes. Rev Mineral Geochemistry 62:155–167. doi: 10.2138/rmg.2006.62.7

Sorby HC (1858) On the Microscopical Structure of Crystals, indicating the Origin of Minerals and Rocks. Q J Geol Soc London 14:453–500.

Sparks RSJ, Marshall L (1986) Thermal and mechanical constraints on mixing between mafic and silicic magmas. J Volcanol Geotherm … 29:99–124.

Spera F (1981) Carbon dioxide in igneous petrogenesis: II. Fluid dynamics of mantle metasomatism. Contrib to Mineral Petrol 77:56–65.

Straub SM, LaGatta AB, Martin-Del Pozzo AL, Langmuir CH (2008) Evidence from high-Ni olivines for a hybridized peridotite/pyroxenite source for orogenic andesites from the central Mexican Volcanic Belt. Geochemistry, Geophys Geosystems. doi: 10.1029/2007GC001583

Tepper JH, Nelson BK, Bergantz GW, Irving AJ (1993) Petrology of the Chilliwack batholith, North Cascades, Washington: generation of calc-alkaline granitoids by melting of mafic lower crust with variable water fugacity. Contrib to Mineral Petrol 113:333–351. doi: 10.1007/BF00286926

Till CB, Vazquez JA, Boyce JW (2015) Months between rejuvenation and volcanic eruption at Yellowstone caldera, Wyoming. Geology 1–5. doi: 10.1130/G36862.1

Tsuno K, Dasgupta R (2012) The effect of carbonates on near-solidus melting of pelite at 3GPa: Relative efficiency of H 2O and CO 2 subduction. Earth Planet Sci Lett 319-320:185–196. doi: 10.1016/j.epsl.2011.12.007

Tuttle OF, Bowen NL (1958) Origin of Granite in the Light of Experimental Studies in the System NaAlSi3O8–KAlSi3O8–SiO2–H2O. Geol Soc Am Mem 74:1–146. doi: 10.1130/MEM74

Wilshire HG (1987) Mantle Metasomatism and Alkaline Magmatism. doi: 10.1130/SPE215

CHAPTER II

MELT INCLUSION EVIDENCE FOR CO_2-RICH MELTS BENEATH THE WESTERN BRANCH OF THE EAST AFRICAN RIFT: IMPLICATIONS FOR LONG-TERM STORAGE OF VOLATILES IN THE DEEP LITHOSPHERIC MANTLE

2.1. ABSTRACT

We present new major element, trace element, and volatile (H_2O, CO_2, S, F, and Cl) concentrations of olivine-hosted melt inclusions from five high-K, low-silica basanites from the Western Branch of the East African Rift System, and use these data to investigate the generation of H_2O- and CO_2-rich melts at up to ~150km depth. Measured H_2O and CO_2 concentrations reach ~2.5 wt% and ~1 wt%, respectively, representing some of the highest CO_2 concentrations measured in a melt inclusion to date. These measurements represent direct evidence of the high CO_2 and H_2O concentrations required to generate high-K alkaline lavas, and the CO_2 that has been previously inferred to be necessary for the low mantle potential temperatures in the area. Ratios of CO_2/Nb, CO_2/Ba, and CO_2/Cl are used to estimate an initial melt CO_2 concentration of 5-12 wt%. The measured CO_2 concentrations are consistent with CO_2 solubilities determined by molecular dynamics calculations and high pressure experiments for melt generation at 4-6 GPa, the depth of melting suggested by previous studies in the area. These melt inclusions measurements represent direct evidence for the presence of H_2O- and CO_2-rich melts in the deep upper mantle that have been proposed based on experimental and seismic evidence. Primitive mantle normalized trace element patterns more closely resemble those found in subduction

settings rather than ocean island basalt, and ratios of slab fluid tracers such as Li/Dy and B/Be indicate that the measured volatile abundances may be related to Neoproterozoic subduction during the assembly of Gondwana, implying the storage of volatiles in the mantle by subduction-related metasomatism.

2.2. INTRODUCTION

It has long been appreciated that the generation of intra-plate, silica-undersaturated alkaline magmas requires the involvement of a metasomatized mantle source rich in volatiles, specifically CO_2 and H_2O (Brey and Green 1975; Menzies and Murthy 1980; Spera 1981; Roden and Murthy 1985; Edgar 1987; Foley 1992; Green and Falloon 1998; Foley et al. 2009; Green 2015). These mantle metasomes have the potential to be reservoirs of CO_2 and H_2O on short to long time-scales, and are generally only identifiable when thermobaric perturbations lead to melting and eruption of alkaline lavas. While it is understood that these rocks require a metasomatically modified mantle source, the mechanism and timing of metasomatism is often difficult to constrain, leaving questions of volatile storage timescales and enrichment mechanisms unanswered. Small fractions of carbonatitic to carbonate-bearing silicate liquid generated from low degree partial melts of the mantle at depths of ~100-300 km have been invoked as potential metasomatic agents (Mengel and Green 1989; Dasgupta and Hirschmann 2006; Foley et al. 2009), as well as fluids and sediment melts from a subducting slab (Tsuno and Dasgupta 2012). However, it is clear that fluids introduced by subducting slabs are a potent metasomatic agent that can enrich the mantle with volatiles, provided the volatile phases are not all fluxed to the atmosphere during arc volcanism (Poli and Schmidt 2002; Thomsen and Schmidt 2008).

Data from natural systems demonstrate that subducted volatiles can be efficiently returned to the surface from the mantle via arc volcanism (Fischer 2008; Plank et al. 2009) and also that some proportion of the subducted volatiles may be stored in the mantle for hundreds of millions to possibly several billion years (Pettke et al. 2010; Rooney et al. 2014). Investigating the generation of alkaline intraplate lavas can provide insight into the storage of volatile elements in the mantle lithosphere and the stability of lithospheric metasomes over geologic time. There is a growing body of evidence for the long-term storage of elements in mantle metasomes that are later remobilized during melting by small thermobaric perturbations (Larsen et al. 2003; Pettke et al. 2010; Rooney et al; 2014). For example, Rooney et al. (2014) investigated the metasomatic origins of an isolated field of alkaline lavas in the middle of the Ethiopian large igneous province. These 24 Ma alkaline lavas formed by the melting of metasomatized mantle, stabilized at ~700 Ma, during Pan-African subduction. This is the only known alkaline exposure in the area, and has significant implications for the mantle beneath the entire East African Rift.

The western branch of the East African Rift is ideally suited to further investigate the potential for long-term storage of volatiles in mantle metasomes owing to the abundant and accessible alkaline eruptions and the complex subduction history during Pan-African Orogeny. Previous studies in the Virunga volcanic field have investigated whole-rock major-element, trace-element, and isotopic characteristics of the volcanics (Vollmer and Norry 1983; Rogers 1998; Platz et al. 2004; Chakrabarti et al. 2009; Muravyeva et al. 2014), however there exist few measurements of volatiles in the area (Head et al. 2011). Here we present melt inclusion data from a set of high-K basanites from the Bufumbira volcanic field in the Virunga area of the western branch of the East African Rift System that provide insight into the high volatile

contents in the initial melts, enrichments in fluid-mobile elements, and subduction-like trace-element signatures.

2.3. BACKGROUND GEOLOGY

A comprehensive review of the geologic history of the East African Rift System is presented by Baker et al. (1972) and Chorowicz (2005), and is only briefly described here. The East African Rift System extends from the Afar triple junction to Mozambique and is broken into three main segments: (1) the main Ethiopian rift (MER), extending from the Afar triple junction south to northern Kenya (Corti 2009), (2) the eastern branch, which extends from southern Ethiopia into northern Tanzania, on the east side of the Tanzania Craton (Baker and Wohlenberg 1971), and (3) the western branch, extending from northern Uganda through the Uganda/Congo/Rwanda tri-state region to Mozambique (Ebinger 1989; Pasteels et al. 1989; Kampunzu et al. 1998; Figure 2.1). Volcanic activity began in southern Ethiopia at ~45 Ma, while the more voluminous flood basalts and rift-related activity in northern Ethiopia began at ~30-25 Ma (Berhe et al. 1987; George et al. 1998). The rifting propagated southward, bifurcating around the Tanzanian Craton, generating the eastern and western branches shown in Figure 2.1.

Rifting in the western branch commenced at ~12 Ma (Ebinger et al. 1989; Pasteels et al. 1989; Kampunzu et al. 1998; Roberts et al. 2012), although Roberts et al. (2012) suggested that rift initiation may have begun at ~25 Ma, contemporaneous with the initiation of the voluminous flood basalts in Ethiopia. The western branch is sub-divided into four distinct volcanic segments that together span ~1200km. These four segments, from north to south, are Toro-Ankole, Virunga, Kivu, and Rungwe (Figure 2.1). Volcanism began in Virunga at ~12 Ma, followed by Kivu and Rungwe at ~8-9 Ma and Toro-Ankole at ~1 Ma, where rifting is propagating northward (Ebinger 1989). The volcanic activity of the western branch is characterized by a compositional

range from carbonatitic and silica-undersaturated ultrapotassic lavas to tholeiitic lavas, with a systematic increase in SiO_2 and decrease in K_2O from Toro-Ankole to Kivu (Furman and Graham 1999; Tappe et al. 2003; Furman 2007; Eby et al. 2009).

The Bufumbira volcanic field in southwestern Uganda (Figure 2.1, field area) is a section of the Virunga province and contains ~40 cinder cones first described by Holmes and Harwood (1937). Lavas in the area are predominantly high-K basanites, though latites and trachy-andesites also occur (Ferguson and Cundari 1975; Barifaijo et al. 2010). It has been suggested that these lavas were sourced from a phlogopite-bearing, carbonated mantle (Ferguson and Cundari 1975; Barifaijo et al. 2008; Rosenthal et al. 2009). It was from this area that lavas were sampled for this study to characterize the volatile abundance in olivine-hosted melt inclusions.

2.4. ANALYTICAL METHODS

2.4.1. Whole rock major- and trace-element analysis

Twenty-four whole-rock samples were cut into slabs, trimmed to remove surface alteration, polished to remove saw marks, and ultrasonically cleaned in DI water to remove any residual debris from cutting and polishing. These slabs were subsequently crushed in a steel-jaw crusher and powdered in a rotary flat alumina ceramic-plate grinder. Sample powders were then prepared as fused lithium tetraborate glass disks for major and trace element analysis at Michigan State University following the procedure outlined by Deering et al. (2008). Briefly summarized here, major elements and the trace elements Zr, Sr, Rb, and Ni, were analyzed by using a Bruker S4 Pioneer 4 kW wavelength dispersive X-ray fluorescence spectrometer. The concentrations of other trace elements were obtained by using a Cetac LSX-200 laser and a Micromass Platform inductively coupled plasma mass spectrometer (LA-ICP-MS). Co-existing Fe-Ti oxides in polished thin sections were analyzed using a CAMECA SX 100 electron probe

micro analyzer (EPMA) in the Electron Microbeam Analysis Laboratory (EMAL) at the University of Michigan. The oxide minerals were analyzed by using an accelerating voltage of 15 keV, a beam current of 15 nA, and a point-focused beam. Peak and background count times were 20 and 10 seconds, respectively, for all elements analyzed.

2.4.2. Melt inclusion selection and preparation

Olivine-hosted melt inclusions from five lava samples, chosen to cover the full range of observed whole-rock MgO content of the volcanic field, were isolated, inspected, and prepared for analysis. Samples were crushed and sieved, and olivine grains from the 850-425 μm size fraction were hand-picked under a binocular microscope. Individual olivine crystals that contained melt inclusions at least 30 μm from the edge of the olivine crystal, were free of visually discernable cracks, and had no other visually apparent defects were selected. All melt inclusions observed were crystallized, and were therefore rehomogenized by using a piston cylinder apparatus in Youxue Zhang's laboratory at the University of Michigan to produce a glass for chemical characterization (see Hui et al. (2008) for calibration). To prevent inclusion decrepitation during rehomogenization, batches of 10-30 olivine grains from each whole-rock sample were rehomogenized together following the techniques outlined in Kent (2008). A graphite capsule was used to hold the olivine grains, a graphite furnace was used for heating, MgO spacers held the center of the capsule in the center of the furnace, and barium carbonate was the pressure medium. Samples were first held at 200 °C and ~500 MPa for two hours to allow for relaxation of the cell assembly. The pressure and temperature were then increased in less than one minute to 600 MPa and 1300 °C, respectively, and held at those conditions for eight minutes, then quenched to below 200 °C in less than 20 seconds. Eight-minute rehomogenization times were sufficient to produce a glass, and have been demonstrated to

minimize H_2O loss from the inclusion (Danyushevsky et al. 2002; Rowe et al. 2007). Short rehomogenization times also minimize the possibility of melt-inclusion contamination by the graphite capsule as the solubility and diffusivity of C in olivine are very low, at 0.1-1 ppm and $<10^{-12}$ cm^2/s, respectively (Keppler et al. 2003; Shcheka et al. 2006; Tingle et al. 1988). Recovered olivine grains were polished with 600-grit SiC sandpaper until melt inclusions were exposed at the surface, and then the crystals were mounted in epoxy rounds for EPMA. Epoxy rounds were the polished with finer abrasives down to 0.1 μm alumina powder.

2.4.3. Melt-inclusion and host-crystal major-element analysis

Polished olivine grain mounts were carbon coated, and the major element composition of individual melt-inclusion glass was determined by using EPMA. An accelerating voltage of 15 keV, beam current of 4 nA, and a 5 μm defocused beam were used. The major-element composition of each host-olivine crystal was quantified by using an accelerating voltage of 15 keV, a beam current of 10 nA, and a focused beam. Counting times in the melt inclusions and olivine host for all elements were 20 s and background counting times were half of the peak counting time. Detection limits were typically in the range of 0.02-0.06 wt%.

2.4.4. Measurements of CO_2, H_2O, F, S, and Cl in melt inclusions

The abundances of CO_2, H_2O, F, S, and Cl were measured with a Cameca IMS 1280 secondary ion mass spectrometer (SIMS) at the Northeast National Ion Microprobe Facility (NENIMF) at Woods Hole Oceanographic Institute. Before sample analysis, olivine grains were re-polished to remove any trace of the carbon coating. Olivine grains were then removed from the epoxy mount by using a pointed soldering iron, and the crystals were pressed into an indium mount for better vacuum during the analysis. The mounts were then re-polished, washed with isopropanol, and stored under vacuum prior to cold coating. The gold coated sample mount was

held in the machine airlock for ~12 h before analysis. The melt inclusions were analyzed by using a Cs^+ primary beam with a 1.5 nA current and a 10 μm beam rastered over a 30x30 μm area with a 15x15 μm field aperture to eliminate any beam-edge effects. To eliminate any surface contamination, each spot analyzed was pre-sputtered for four minutes prior to analysis. Preparation, analytical conditions, and calibration for SIMS analysis followed techniques outlined by Shimizu et al. (2009). The raw data were monitored continually for fluctuation of signal intensity during acquisition (Figure 2.2). Sample signals that displayed random fluctuation had extra time appended to the analysis to see if the signal stabilized. Samples displaying decreasing signal intensity had either extra time appended to stabilize or were analyzed a second time, including pre-sputtering to clean the melt inclusion surface. Data from samples that failed to produce a stable signal are not reported.

2.4.5. Trace-element analysis of melt inclusions and host-olivine

Following SIMS analyses, the olivine grains were polished with 0.3 μm alumina powder and washed with ethanol to remove the gold coating and any remaining Cs implanted by the SIMS primary beam. Melt inclusions and their host olivine crystals were then analyzed by using a Photon Machines Analyte 193 ultra-short-pulse Excimer laser coupled to a Bruker 820-MS ICP-MS at Rensselaer Polytechnic Institute. A laser spot size of 65 μm, pulsed at 4 Hz was used to ablate large melt inclusions (>65 μm) and (separately) each olivine host crystal. A laser spot size of 30 μm was used for smaller inclusions (<65 μm). For all melt inclusions, the size of the laser spot was smaller than the diameter of the inclusion; hence, avoiding mixed inclusion – host analyses. Samples were sputtered for one second to ensure a clean surface before analysis. The He carrier gas background signal for each analysis was measured for 20 seconds, at which time the laser was turned on and each inclusion or host crystal was ablated for ~40 seconds. Data were

reduced by using the SILLS software program (Guillong et al. 2008). GSD-1G (Jochum et al. 2005) was used as a standard and ML3B-G (Jochum et al. 2006) was used as a check standard. Both standards were re-analyzed after every 10 melt inclusion analyses. To correct for differences in ablation efficiency, ^{43}Ca was used as an internal standard.

2.4.6. Post-entrapment crystallization

It is well known that the chemistry of a melt inclusion may be effected by post-entrapment crystallization as well as reheating during laboratory homogenization (Danyushevsky et al. 2002). To correct for the compositional effects of post-entrapment crystallization and overheating of an inclusion – both assumed to be able to add or subtract oxide components such as MgO from the inclusion and into olivine or vice versa – we followed the corrections to elemental abundance method described in Sobolev and Shimizu (1993). Olivine was numerically added or subtracted incrementally, in 1 wt% increments, to or from an individual inclusion until each olivine-liquid (melt inclusion) pair had an Fe-Mg K_D of 0.28. This Fe-Mg K_D value is appropriate for the bulk composition of lava samples in the current study, based on Gee and Sack (1988) who demonstrated that the olivine-liquid K_D value decreases with decreasing SiO_2 and increasing alkali content of the silicate melt from the general Fe-Mg K_D of 0.3 for basalt (Roeder and Emslie 1970). The two-oxide Fe-Ti geothermometer and oxybarometer of Ghiorso and Evans (2008) was used to estimate the oxidation state of the host rock of each inclusion. The Fe^{3+}/Fe_T was then calculated for the melt in each inclusion by using the expression relating Fe^{3+} and fO_2 of Kress and Carmichael (1991). The amount of olivine correction ranged from -26% to +17%, where negative values represent olivine subtracted from the inclusion necessitated by apparent overheating and assimilation of host olivine during rehomogenization, and positive numbers represent incomplete homogenization of sidewall crystallization.

2.5. RESULTS

2.5.1. Petrography

Petrographic observations indicate that all samples are dominated by olivine and clinopyroxene, except 08WR-14p, a phlogopite-clinopyroxenite, which is dominated by phlogopite and clinopyroxene. Phlogopite, nepheline, and leucite are minor phases in all samples. All samples are hypocrystalline, display varying degrees of vesicularity, and have <1 modal % oxide phases. The exception here is sample 08WR-20 which contains ~10 modal % oxide phases.

2.5.2. Major-elements of whole-rocks

All whole-rock samples follow an alkaline trend on a total alkali-silica diagram (Le Bas et al. 1986; Figure 2.3). Of the 24 samples analyzed, there are 16 basanites, three basalts, two trachy-basalts, and three trachy-andesites (Table 2.1). The Mg# [$(X_{MgO}/(X_{MgO} + X_{FeO}) * 100)$] of the basanites and basalts ranges from 49 to 78, where X_{FeO} was calculated by using the relationship between Fe^{3+} and fO_2 of Kress and Carmichael (1991) and fO_2 was obtained by using the two-oxide Fe-Ti geothermometer and oxybarometer of Ghiorso and Evans (2008). All samples are shoshonitic ($K_2O > Na_2O$), and are consistent with bulk compositions of volcanic rocks reported in previous studies of the Virunga province (Holmes and Harwood 1937; Rogers et al. 1992; Rogers et al. 1998; Chakrabarti et al. 2009; Head et al. 2011; Muravyeva et al. 2014).

Whole-rock MgO concentrations range from 1.75 wt% to 19.5 wt% (Table 2.1), and trends of major-element concentrations plotted vs. MgO are consistent with the fractionation of olivine and clinopyroxene (Figure 2.4, shaded fields). Samples with MgO >5 wt% display increasing Al_2O_3, K_2O, Na_2O, and P_2O_5 with decreasing MgO (Figure 2.4, shaded fields).

Samples with <5 wt% MgO display decreasing TiO_2, $FeO_{(T)}$, and CaO with decreasing MgO (Figure 2.4, shaded fields).

2.5.3. Major-elements of melt inclusions

The MgO concentrations of olivine-hosted melt inclusions range from 1.6 to 14.2 wt% and the SiO_2 concentrations of melt inclusions range from 35.9 to 51.3 wt% (Table 2.2; Figure 2.4). Trends of major-element concentration vs. MgO indicate decreasing $FeO_{(T)}$, TiO_2, and MnO and increasing SiO_2, Al_2O_3, K_2O, and P_2O_5 with decreasing MgO. Sample 08WR-20 exhibits large variations in TiO_2, $FeO_{(T)}$, and MnO, decreasing strongly with decreasing MgO, which are discussed in section 5.1.

2.5.4. Trace-elements of whole-rock and melt inclusions

Selected whole-rock and melt inclusion trace-element data vs. MgO are presented in Figure 2.5. Whole-rock trace-element data are found in Table 2.3, melt-inclusion trace element data are in Table 2.4. Sample 08WR-20 exhibits high concentrations of V with increasing MgO, discussed in detail in section 5.1. Primitive-mantle normalized whole-rock and melt inclusion compositions have a steep heavy rare earth element slope (Figure 2.6). Potassium exhibits some depletion in all samples except 08WR-20. The concentration of Li is enriched in melt-inclusions from sample 08WR-20, whereas some melt-inclusions are enriched and some depleted in Li (i.e. samples 08WR-7, 08WR-13, and 08WR-16).

2.5.5. Volatile concentrations of melt inclusions

The CO_2 concentrations of the melt inclusions range from ~25 to 9,950 ppm (Table 2.5). These measured CO_2 concentrations are consistent with molecular dynamics simulations (Guillot and Sator 2011), high-pressure partial melting experiments (Dasgupta et al. 2007; 2013), and observations and extrapolation from mid-ocean-ridge basalts (MORBs) (Saal et al. 2002), as

discussed in section 5.2. They are also consistent with measured volatile contents of olivine-hosted melt-inclusions from the nearby Nyamuragira volcano (Head et al. 2011) as well as the volatile concentrations measured in other intraplate basanites (Oppenheimer et al. 2011). Measured volatile contents do not display any correlations with major elements.

The H_2O concentrations for the melt-inclusions measured range from 0.3 to 2.5 wt% (Table 2.5). These concentrations are higher than the ranges reported for MORB and E-MORB, which are 0.1 - 0.3 wt% and 0.3 - 1.0 wt%, respectively (Dixon et al. 1995; Michael 1995; Danyushevsky et al. 2000). The concentration of H_2O decreases with decreasing wt% MgO and does not correlate with the variability of other melt-inclusion major-elements.

The S concentrations of melt-inclusions range from ~10 to 4,000 ppm (Table 2.5; Figures 2.6a,b). The inclusion with the highest measured S concentration (i.e., 4,032 ppm) also contains the highest measured CO_2 concentration (Figure 2.6b). The abundance of Cl ranges from ~90 to 2,100 ppm. The concentration of Cl increases with increasing S and F (Figure 2.6a,c); however, there is no apparent correlation of Cl concentration with H_2O or CO_2 concentration. The concentration of F varies from ~800 to 4,000 ppm, and the two inclusions with the highest measured fluorine concentrations, 3,964 and 3,429 ppm, contain the highest measured H_2O concentrations, 2.3 and 2.5 wt%, respectively, with a general trend of increasing F with increasing H_2O (Figure 2.6d). There is no apparent correlation among S, Cl, or F with major-element concentrations.

2.6. DISCUSSION

2.6.1. Comparison of whole-rock and melt inclusion compositions

The MgO concentrations of olivine-hosted melt-inclusions span a smaller range (1.6 to 14.2 wt%) than the MgO concentration of the whole rock (4.7 to 19.5 wt%). Most melt

inclusions have lower MgO contents than their respective whole rock, except for sample 08WR-20 which falls in the middle of the range for melt inclusion MgO abundances (Figure 2.4). For samples 08WR-7, 08WR-8, 08WR-13, and 08WR-16, this is most likely due to olivine accumulation (cf. Rosenthal et al. 2009), but could also be due to under-correcting for the post-entrapment crystallization. Compositional variability in melt inclusions from 08WR-20 is discussed below. The SiO_2 concentrations of melt inclusions range from 35.9 to 51.3 wt%, mostly within the range of all lavas sampled (38.1 to 61.1 wt% SiO_2).

The melt inclusion abundances of major-elements plotted against MgO generally follow trends similar to those of the whole rocks (Figure 2.4); however, major element concentrations in the melt inclusions display slightly greater variability than the whole rocks. An exception is in the abundances of TiO_2, $FeO_{(T)}$, and MnO for inclusions from sample 08WR-20, which do not follow the trends of other samples. Inclusions from sample 08WR-20 display unrealistic compositions, with elevated concentrations of FeO, MnO, TiO_2, and V, and also SiO_2 contents lower than the whole rock (Figures 2.4 and 2.5). We interpret this to result from co-entrapment of melt and an oxide phase, which is subsequently re-melted during the rehomogenization process. These phases are difficult to observe prior to homogenization owing to the opacity of the crystalline inclusions. The elevated concentrations of FeO, MnO, TiO_2, and V are consistent with the trapping and subsequent melting of ilmenite or titanomagnetite, both of which are petrographically observed in abundance in sample 08WR-20. Further evidence for the assimilation of iron-titanium oxides into the inclusions of 08WR-20 is in the comparison of FeO, MnO, TiO, and V with SiO_2, in which these elements increase with decreasing silica content, a trend not observed in melt inclusions from the other four samples. Though differences in these

elements are apparent, there is an overall agreement between melt inclusion and whole-rock compositions for the remaining major elements.

On a primitive-mantle normalized trace-element plot (Figure 2.6), melt inclusion compositions are very similar to those of their respective whole-rock samples. Inclusions from 08WR-8 are slightly enriched relative to whole rock, whereas samples 08WR-7, 08WR-13, 08WR-16, and 08WR-20 have nearly the same concentrations as whole rock. All of the melt inclusions display greater depletions in K and Pb than whole-rock, but are otherwise in good agreement. Because of this similarity between whole-rock and melt-inclusion chemistry, and in order to simplify the rest of the discussion, any further mention of major and trace element compositions refers to both whole-rock and melt inclusion data except where specifically noted.

2.6.2. Degassing trends and the determination of initial CO_2 concentrations

Previous studies have used CO_2, H_2O, Cl, Ce, Nb, and Ba concentrations in MORB glasses, melt-inclusions, and "popping rock" to define undegassed magmatic CO_2/Cl, CO_2/Nb, and H_2O/Ce values (Michael 1995; Danyushevsky et al. 2000; Dixon and Clague 2001; Saal et al. 2002; Simons et al. 2002; Cartigny et al. 2008; Helo et al. 2011; Rosenthal et al. 2015). Rosenthal et al. (2015) determined peridotite/melt partition coefficients for C and compared their results, paired with the Nb and Ba from Workman and Hart (2005), with CO_2/Nb and CO_2/Ba values from other studies. Our melt-inclusion data exhibit a large range of CO_2/Nb, CO_2/Ba, and CO_2/Cl values that all fall below the undegassed ratios (Saal et al. 2002; Cartigny et al. 2008; Rosenthal et al. 2015), suggesting that the loss of CO_2 is the cause of CO_2/Nb, CO_2/Ba, and CO_2/Cl variability (Figure 2.8a-c). Similarly, all melt-inclusion H_2O/Ce ratios are below undegassed H_2O/Ce values (Michael 1995; Saal et al. 2002)(Figure 2.8d). These trends, coupled with the relatively constant Nb, Ba, and Ce concentrations (Table 2.4), suggest that the

variability in CO_2/Nb, CO_2/Ba, and H_2O/Ce ratios in melt-inclusions is controlled by the loss of the volatile species, and indicates significant degassing of the melt prior to being entrapped by olivine. In the case of H_2O, diffusive loss of H^+ during cooling and rehomogenization will lead to the loss of H_2O with no loss of Ce, resulting in it being a combined H_2O loss by degassing and diffusion trend. Using these trends, we can attempt to estimate the initial volatile concentration in the melt by projecting the trends to an undegassed mantle source.

Using the calculated CO_2/Cl and CO_2/Nb values of Saal et al. (2002) as an estimate for the initial CO_2 content of the melts generated in our study area, an initial melt CO_2 concentration of 5-10 wt% is predicted based on the CO_2/Cl regression and 3-5 wt% using the CO_2/Nb regression (Figure 2.8a,c). Using the CO_2/Nb values of Cartigny et al. (2008), an initial melt CO_2 concentration of 6-9 wt% is predicted (Figure 2.8a), more closely matching the values calculated by the CO_2/Cl regression of Saal et al. (2002). With the CO_2/Ba value of Rosenthal et al. (2015), an initial melt CO_2 concentration of 12-24 wt% is predicted, much higher than the previous estimates (Figure 2.8b). Rosenthal et al. (2015) suggest that CO_2/Ba ratios are more robust than CO_2/Nb ratios for low degree partial melts as the compatibility of C and Ba are closer than C and Nb. However, our measured Ba concentrations in the melt inclusions are higher than the range recorded by the whole-rocks, whereas Nb is consistent with whole-rock (Figure 2.5), suggesting that we may be over-predicting CO_2 with the CO_2/Ba ratio due to excess Ba in the melt inclusions. These high CO_2 concentration estimates are consistent with the results of partial melting experiments (Dasgupta et al. 2007), and can be used to place constraints on the depth of melt generation.

Assuming these melts are CO_2 saturated, a depth of melting can be estimated by using the solubility data for CO_2 in silicate melt calculated by molecular dynamics (Guillot and Sator

2011). This corresponds to a CO_2-saturated melt at pressures of 4-6 GPa (5-10 wt% CO_2 in MORB). These estimated pressures of partial melting are consistent with studies that describe the depth of melting in the surrounding areas (Chakrabarti et al. 2009; Foley et al. 2009; Rosenthal et al. 2009), and observations from partial melting experiments of a carbonate-bearing lherzolite performed at 3GPa and 1300-1600°C that indicate that partial melts ranging from 35.3 to 45.7 wt% SiO_2 contain CO_2 concentrations ranging from 11.1 to 5.1 wt%, respectively (Dasgupta et al. 2007). However, the whole-rock K_2O/Na_2O values of 1-2 may limit the depth of melting to 3 GPa, the upper limit of amphibole stability (Foley et al. 1999; Rosenthal et al. 2009). This is also consistent with the work of Green (2015) where carbonate-bearing hydrous silicate melt can be generated in intraplate settings at ~3 GPa.

With the exception of one datum at about 2.5 wt% H_2O, a weak trend of increasing CO_2 with increasing H_2O is apparent (Figure 2.9). While the spread of CO_2 then seems ideally suited to investigating degassing paths, the loss of H_2O from a melt inclusion by proton diffusion owing to slow cooling or reheating effectively eliminates any coherent degassing trend in a plot of H_2O vs. CO_2 (Lloyd et al. 2013). It is for this reason that volatile loss by degassing and diffusion is investigated by using the ratio of a volatile species with an incompatible element.

2.6.3. Insights into the mantle source and the origin of the volatiles

Comparisons of trace element compositions with various other source compositions provides insight into mantle source characteristics and can also elucidate the source of volatiles. The primitive mantle normalized trace-element compositions of melt inclusions exhibit elevated large-ion lithophile element (LILE) and light rare earth element (LREE) abundances relative to ocean-island basalts (OIB), but have similar abundances of middle rare earth elements (MREE) and heavy rare earth elements (HREE). Compared also to a global average of arc-related

basanites (Rafferty and Heming 1979; Baker et al 1981; Hirai and Arai 1986; Hole 1988; Davis et al 1993; El Azzouzi et al 1999; D'Orazio et al 2000; Beccaluva et al 2002; Gorring et al 2003; Duggen et al 2005; Espinoza et al 2005; Ichiyama and Ishiwatari 2005; Massaferro et al 2006; Perepelov et al 2006; Orozco-Esquivel et al 2007; Chang et al 2009; Espíndola et al 2010) and to the average composition of Mexican arc lamprophyres (Luhr 1997), the melt inclusions exhibit similar abundances for all elements except for the high field strength elements (HFSE) of the Mexican arc lamprophyres (Figure 2.10). The average Mexican arc lamprophyre composition is used for comparison owing to the similarities in the origin of lamprophyres and the generation of low-silica, high-potassium basanites (Foley 1988; Maria and Luhr 2008). The ratios of LREE/HREE, e.g., La/Yb, for the melt inclusions in the present study are similar to those of average arc lamprophyre and average arc basanite, and are much higher than those for OIB. The La/Yb ratios of the melt inclusions are also a factor of three lower than values from Toro-Ankole, north of Virunga, where repeated freezing of upwelling induced melts is proposed as a the metasomatic agent (Tappe et al. 2003; Rosenthal et al. 2009). This similarity to arc-related rocks may indicate a relationship between the mantle in arc settings and mantle beneath the East African Rift, which prior to the Pan-African Orogeny was itself along a convergent margin. Ratios of LILE/HREE, such as Ba/Yb, for the melt inclusions are also similar to arc-related basanites and much higher than OIB, suggesting that a fluid component may be responsible for the observed trends, as is commonly invoked for arc settings (Lee et al. 2005; Pearce and Stern 2006).

High field strength element ratios are dissimilar to the observed trends in LILE and LREE. The Nb/Ta values of the melt inclusions more closely match OIB and average arc basanite than Mexican arc lamprophyre. The discrepancy in Nb and Ta values between average

arc basanite and average arc lamprophyre could be controlled by rutile stability in subducting slab sediments, where rutile effectively retains Nb and Ta. The elevated Nb and Ta concentrations observed in average arc basanite are consistent with the transfer of HFSE into the mantle via aqueous fluids during subduction (Ryerson and Watson 1987; Foley et al. 2000), or with the presence of ilmenite as a Ti-bearing phase instead of rutile (Foley et al. 1999; Tappe et al. 2008). This finding is consistent with field evidence of HFSE mobility during the blueschist to eclogite transition preserved in exhumed terranes (Gao et al. 2007). Experimental fluid-melt partitioning data from 4-6 GPa and 700-1200 °C corroborate the transfer of HFSE into a fluid-phase during subduction-dehydration (Kessel et al. 2005). It is worth noting that arc basanites globally appear not to show the typical arc-related HFSE depletion (Ryerson and Watson 1987), suggesting that the absence of a HFSE depletion in our melt inclusion data is not inconsistent with being derived from a subduction-modified mantle.

The primitive-mantle normalized melt inclusion data are also very similar to data generated from partial melting experiments wherein hornblendite, clinopyroxene-hornblendite, and hornblendite peridotite sandwiches were melted at 1175-1350°C and 1.5GPa (Pilet et al. 2008). These experiments were designed to investigate the products of partially melting a veined, metasomatized mantle, and the similarity of the East African rift data reported here is consistent with the partial melting of a metasomatized mantle that would likely contain phlogopite as well as amphibole at the estimated depth of melting (i.e., >100km; Rosenthal et al. 2009). Though the mantle in this area contains phlogopite and amphibole, very similar alkaline lavas generated from the partial melt of a metasomatized amphibole-bearing mantle have erupted in the Ethiopian large igneous province (ELIP)(Rooney et al. 2014). Hafnium isotope evidence from these samples suggests that the metasome responsible for the alkalic lavas in the ELIP dates to ~700

Ma, during which fluids and fluid mobile elements were transferred to the mantle during the Pan-African Orogeny (Rooney et al. 2014). Despite the geographic distance between the ELIP the field area of the current study (Figure 2.1), the Pan-African orogenic event continued through the area, propagated further south (Meert and van der Voo 1997), and plausibly metasomatized the mantle beneath the western branch of the East Africa rift system (see below).

In an effort to determine if the volatile phases present in the sampled lavas are consistent with their introduction during subduction at ~700 Ma, various slab fluid tracers were examined owing to the chemical similarity between our samples and arc related rocks (Figure 2.10). Ratios of Li/Yb, a proxy to trace the presence of a slab fluid (Ryan and Langmuir 1987), range from 2 to 32, extending beyond the values for MORB and ocean-island basalt (OIB), which are 2 and 4, respectively (Sun and McDonough 1989). The ratios of B/Be, also a slab fluid tracer (Bebout et al. 1993; Edwards et al. 1993; Ryan and Langmuir 1993), range from 1 to 15, extending beyond the field for MORB and OIB, which range from 0 to 5. Plots of melt inclusion Li/Yb vs. Dy/Yb, and Li/Yb vs. B/Be form an array trending towards global subducted sediment (GLOSS-II; Plank 2014), potentially representing a slab-fluid component or a recycled sediment component (Figure 2.11).

If the volatile phases and the mantle metasomatism are consistent with a subduction origin, then this fluid addition and alteration must have remained in the sub-continental lithospheric mantle for 600-700 million years following the closure of the Mozambique Ocean during the Pan-African Orogeny. This long-term stability of mantle metasomes is consistent with rift-related lavas in Ethiopia (Rooney et al. 2014), and the Rocky Mountains region of the U.S., where Pettke et al. (2010) used Pb isotope abundances in fluid inclusions to conclude that magmas erupted during the Eocene contain a component of Proterozoic lithospheric mantle that

was metasomatized at ~1.8 Ga. However, with the data presented here we cannot rule out old, recycled sediments as the source of the observed geochemical trends, suggesting that old subducted slabs may also be a large volatile reservoir in the mantle.

2.7. CONCLUSIONS

Measured major-element, trace-element, and volatile (H_2O, CO_2, S, F, and Cl) concentrations of olivine-hosted melt inclusions sampled from high-K basanites erupted in the Virunga volcanic field of the western branch of the East African Rift System are consistent with partial melting at depths of at least 100 km in the presence of volatiles. Concentrations of CO_2 in melt inclusions are as high as ~ 1 wt. %, and CO_2/Nb and CO_2/Cl ratios indicate that initial CO_2 concentrations of the magma may have been as much 10 wt% CO_2, which is consistent with CO_2 solubility at the estimated depths of melting. Host-lava and melt-inclusion data are consistent with the partial melting of a metasomatized mantle source. Trace element ratios are consistent with mantle metasomatism by subducting slab-derived fluids, which is consistent with Hf isotope data from other portions of the East African Rift. The combination of high volatile contents and subduction-related signatures suggest that the volatiles measured in the melt inclusions may have been introduced to the mantle during Pan-African subduction at ~700-600Ma and were stored in the lithosphere until remobilization during rifting in the Neogene.

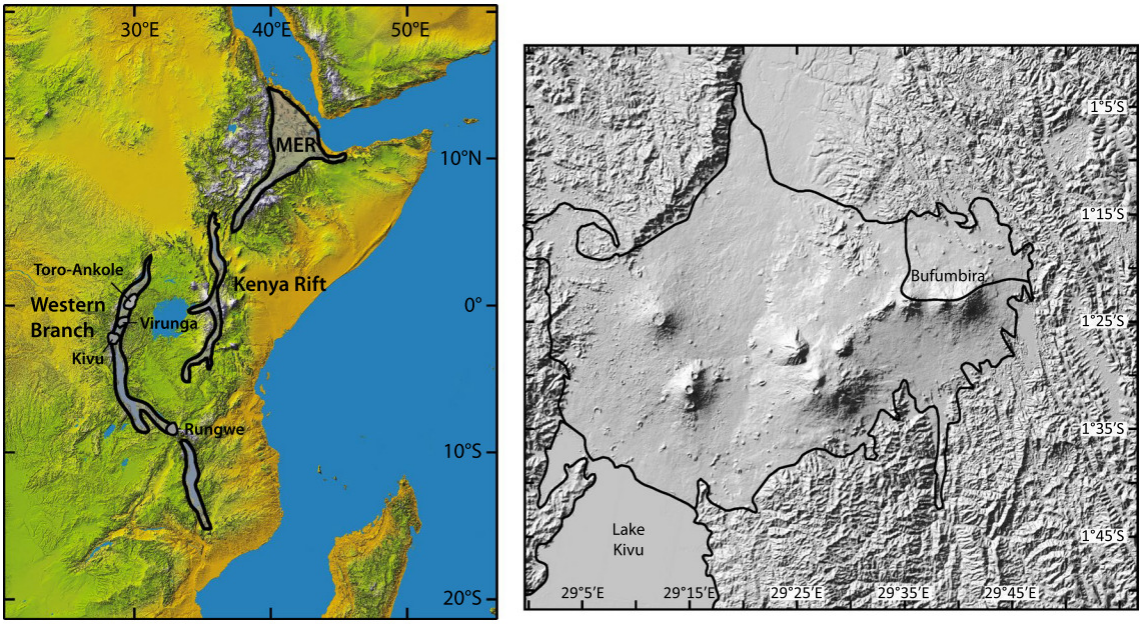

Figure 2.1 Colored digital elevation model of East Africa with the different rift sections shaded, and the Toro-Ankole, Virunga, Kivu, and Rungwe volcanic fields labeled. The small black box in the Western Branch outlines the sample collection site. Basemap from NASA space shuttle radar topography. Inset highlights the Virunga volcanic field and field area, the Bufumbira Volcanic Field. Virunga map from GeoMapApp (www.geomapapp.org)

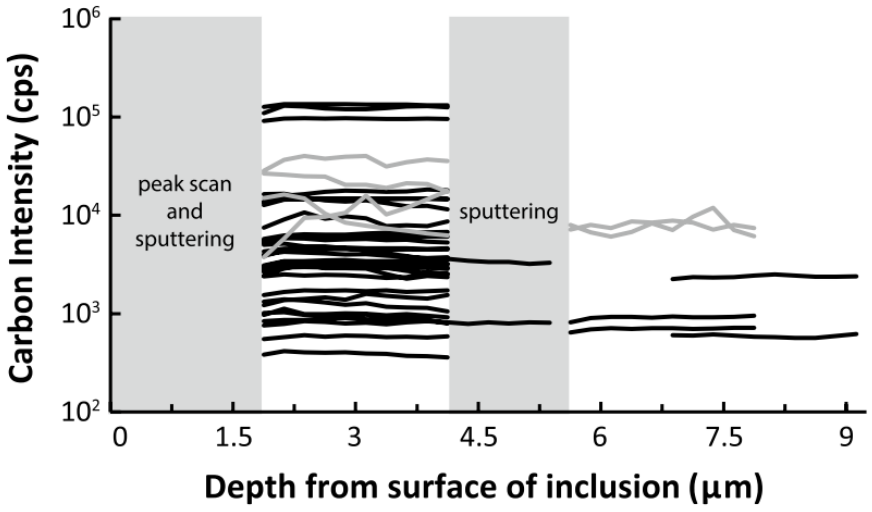

Figure 2.2 Carbon signal intensity vs. melt inclusion depth is plotted for all SIMS analyses. The signal stability for each transient analysis indicates that surface carbon does not contribute to the data. The first 360 seconds of each analysis (first shaded field) are blank as this is a peak scan and sputtering to remove any surface contaminants. The second shaded field is the result of a second run, including sputtering, for two analyses that had extra time appended, as discussed in the text. Gray lines are examples of samples that were excluded due to signal instability

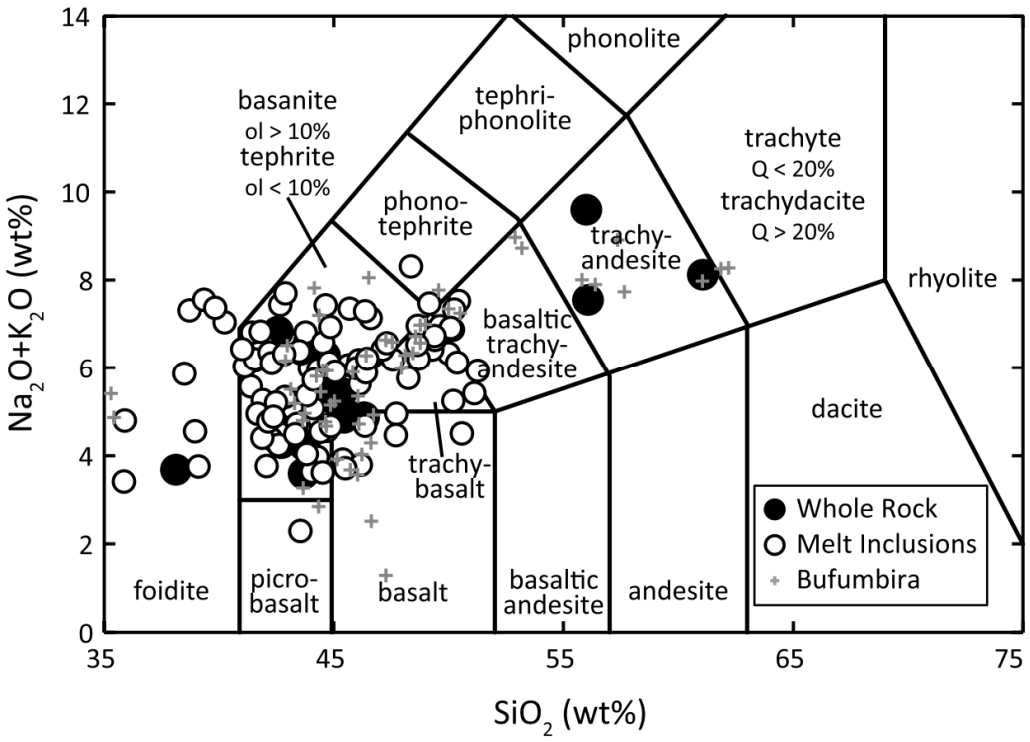

Figure 2.3 Total alkali vs. silica plots of olivine-hosted melt inclusions and their host rocks. Melt inclusions were analyzed from three basanites (08WR-8, 08WR-13, 08WR-16), one basalt (08WR-7), and one trachybasalt (08WR-20). Bufumbira data from Holmes and Harwood (1937)

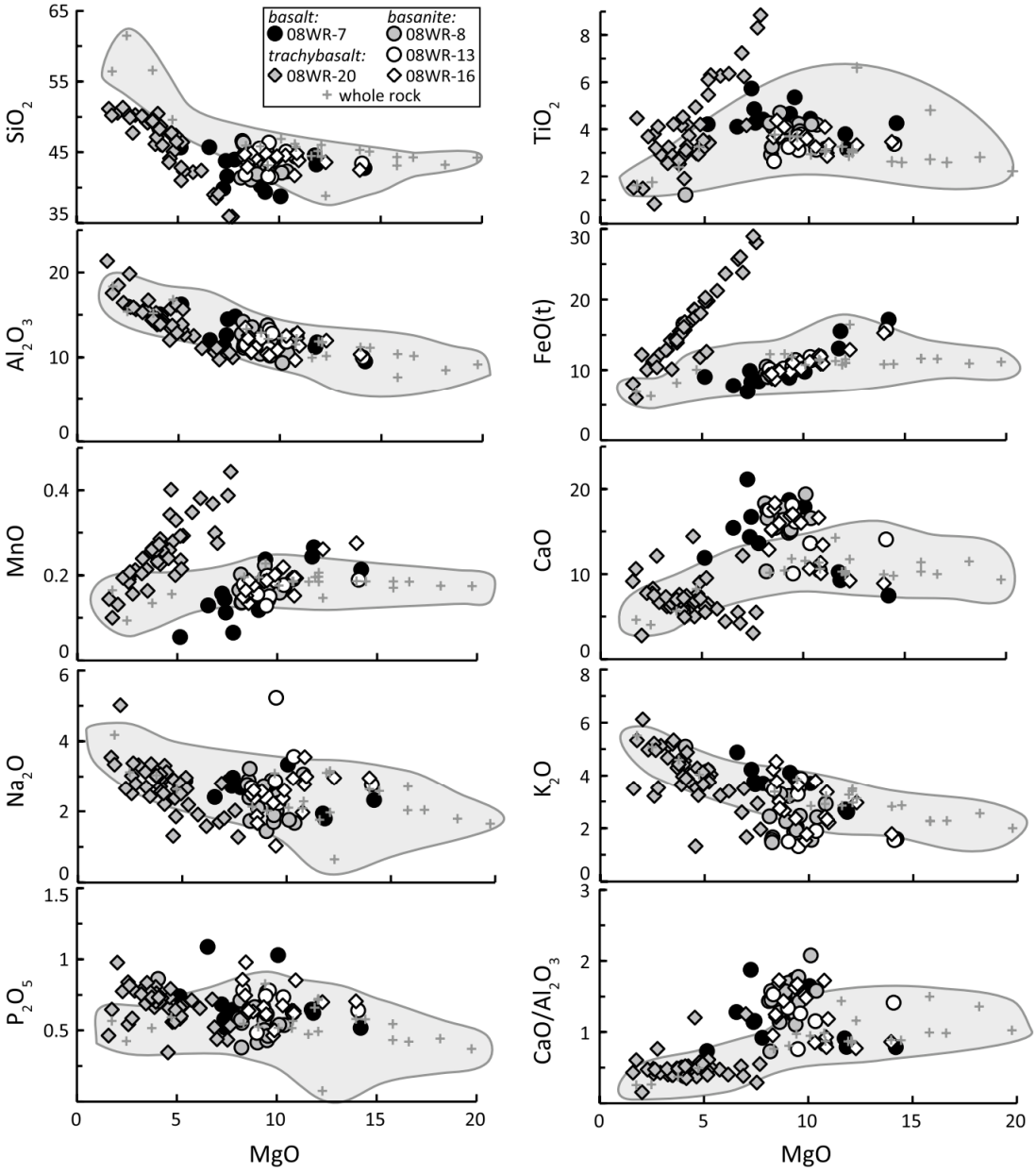

Figure 2.4 Major-element vs MgO plots for melt inclusions and whole rock samples. The shaded field represents the total variability of the whole rock samples

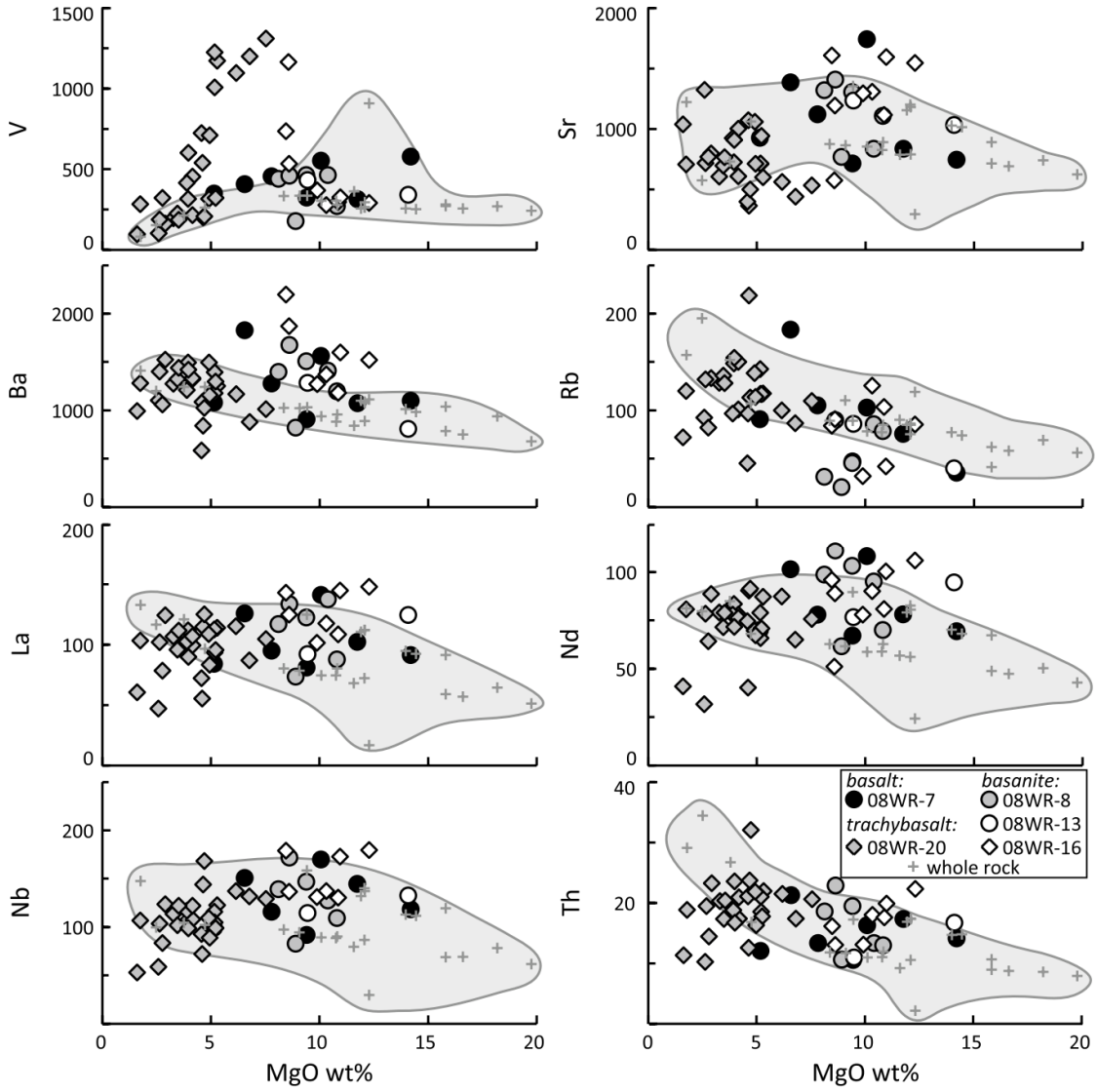

Figure 2.5 Trace-element vs MgO plots for melt inclusions and whole rock samples. The shaded field represents the total variability of the whole rock samples

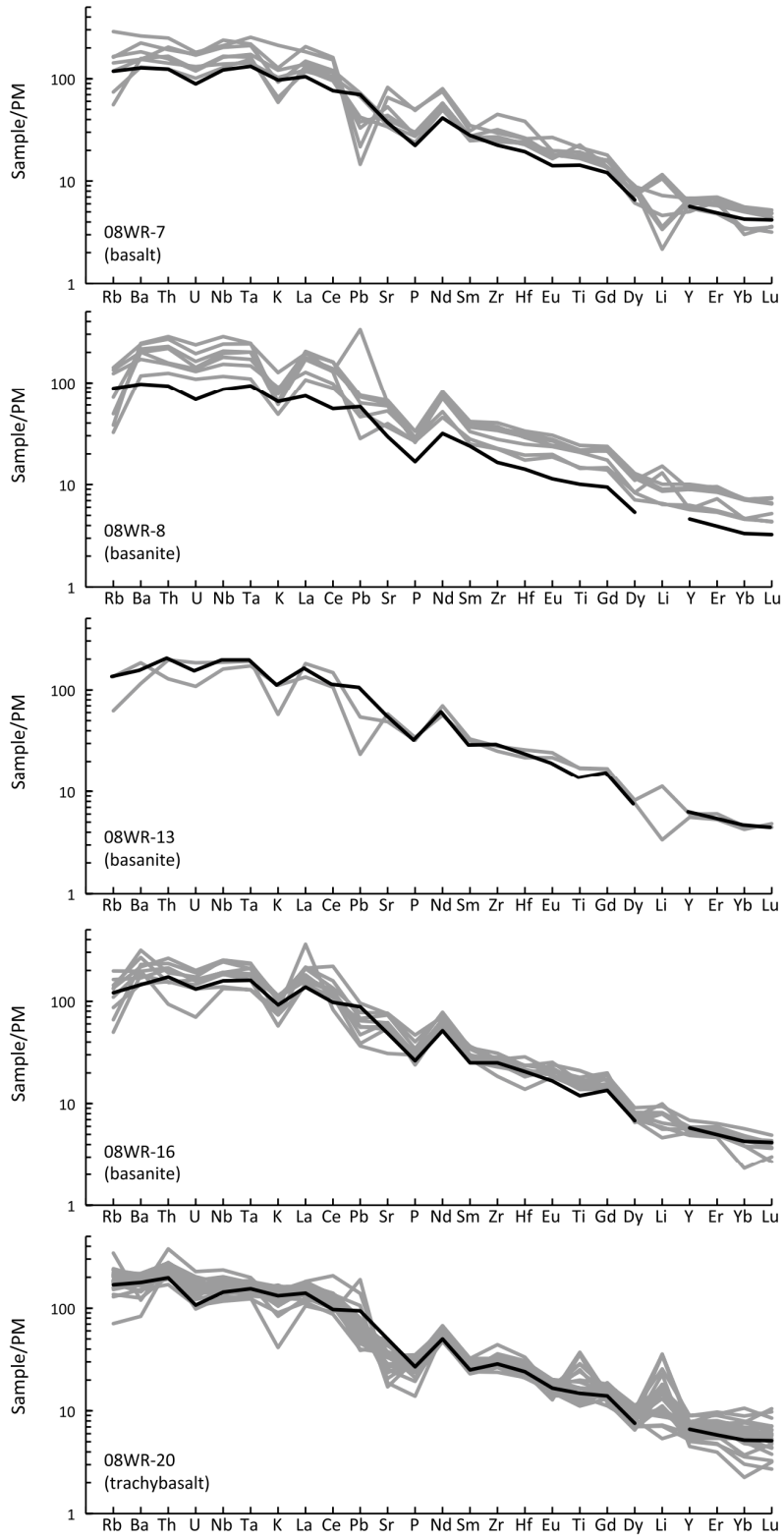

Figure 2.6 Primitive-mantle normalized (Sun and McDonough 1989) multi-element diagrams for melt inclusions and whole rocks. Gray lines represent melt inclusion data, solid black lines represent whole rock

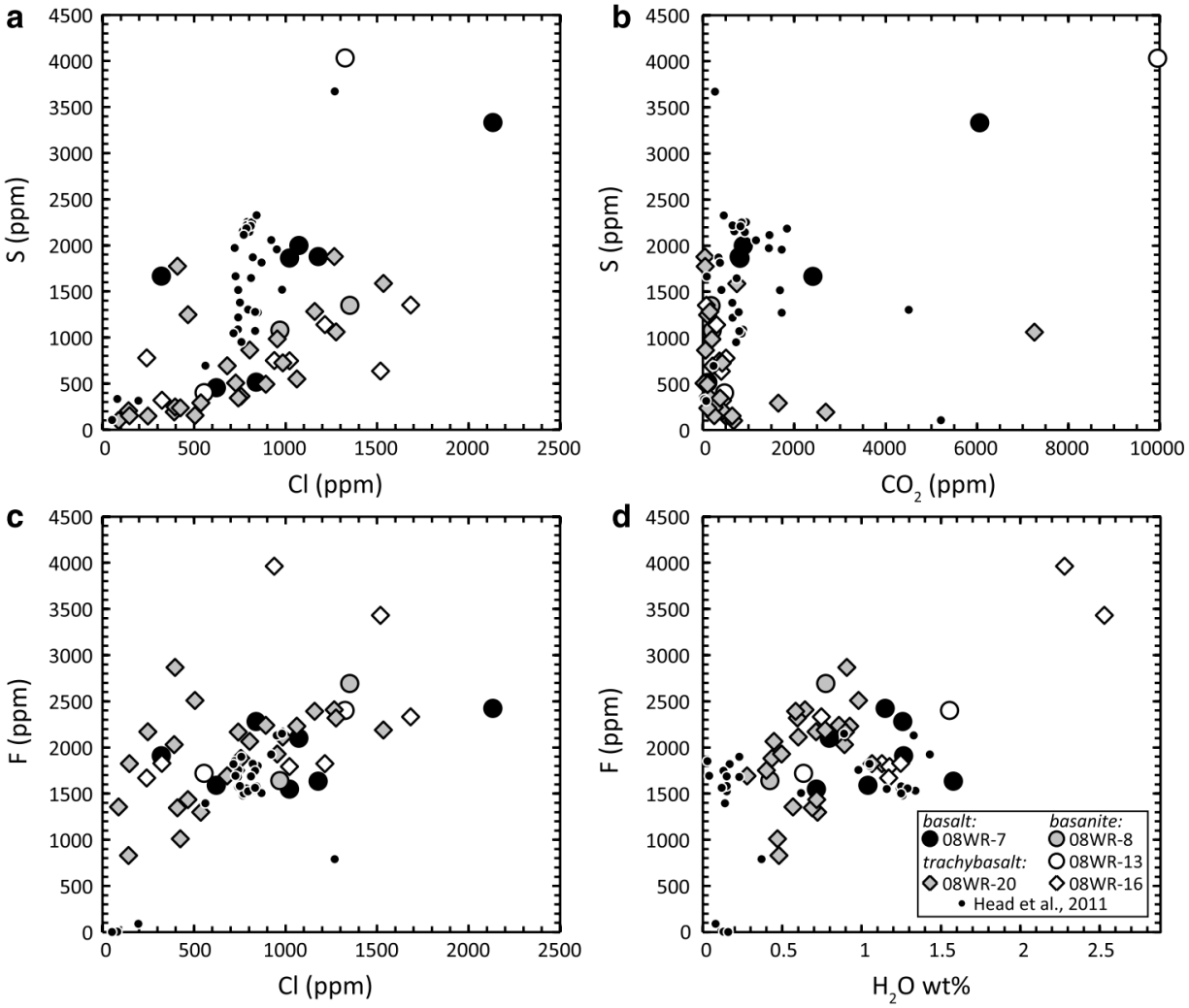

Figure 2.7 Volatile comparison plots. a) S vs Cl. There is a general trend of decreasing S with decreasing Cl. b) S vs. CO_2. Two of the high CO_2 inclusions also record the highest S concentrations. Most of the range of S is expressed at low CO_2 concentrations. **c)** F vs. Cl. There is a general trend of decreasing F with decreasing Cl. d) F vs. H_2O. The two inclusions with the highest H_2O also record the highest F concentrations

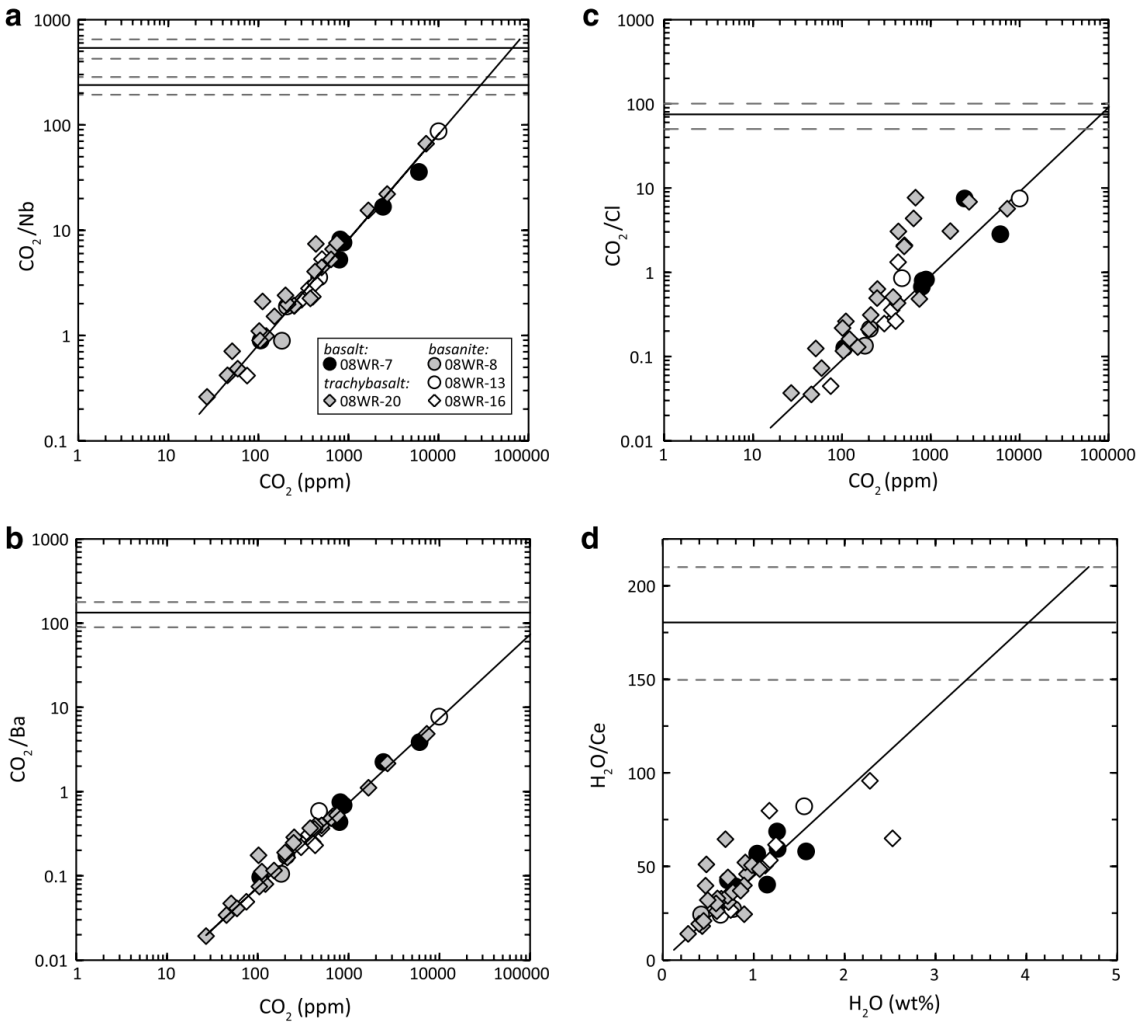

Figure 2.8 CO_2 is compared to Nb, Ba, and Cl, and H_2O is compared to Ce to define degassing trends and to quantify initial volatile concentrations in the melt. a) CO_2/Nb vs CO_2. The lines of constant CO_2/Nb represent mantle ratios and associated errors, calculated by Saal et al. (2002) and Cartigny et al. (2008) as 239 ± 46 and 537 ± 112, respectively. As CO_2 and Nb are expected to behave similarly during partial melting, their ratio should be unaffected by the degree of partial melting. b) CO_2/Ba vs CO_2. Similar to panel a, however Ba has been demonstrated to behave more like C during partial melting (Rosenthal et al. 2015). The line of constant CO_2/Ba is the mantle value proposed by Rosenthal et al (2015) of 133 ± 44. c) CO_2/Cl vs. CO_2. The line of constant CO_2/Cl and associated errors, 75 ± 20, represent undegassed mantle from the data of Saal et al. (2002). d) H_2O/Ce vs H_2O. The line of constant H_2O/Ce, 180 ± 30, represents the manle H_2O/Ce value of Michael (1995). As H_2O and Ce are expected to behave similarly during partial melting, following a degassing trend back to the mantle ratio provides an estimate of the pre-degassed H_2O content of the partial melt

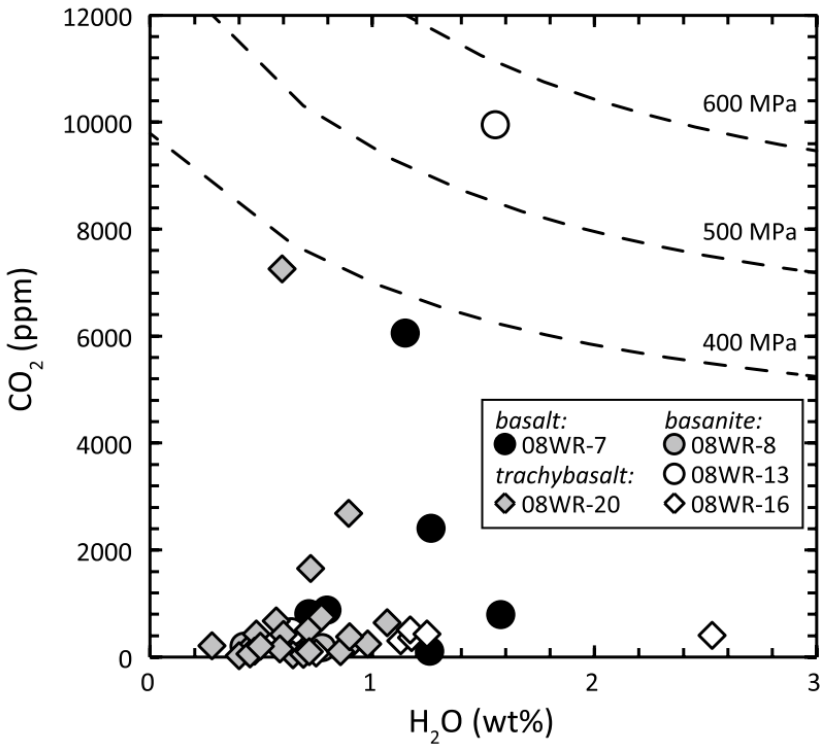

Figure 2.9 CO_2 vs. H_2O plot for all melt inclusions analyzed. Isobars were calculated by using the solubility model of Papale et al. (2006)

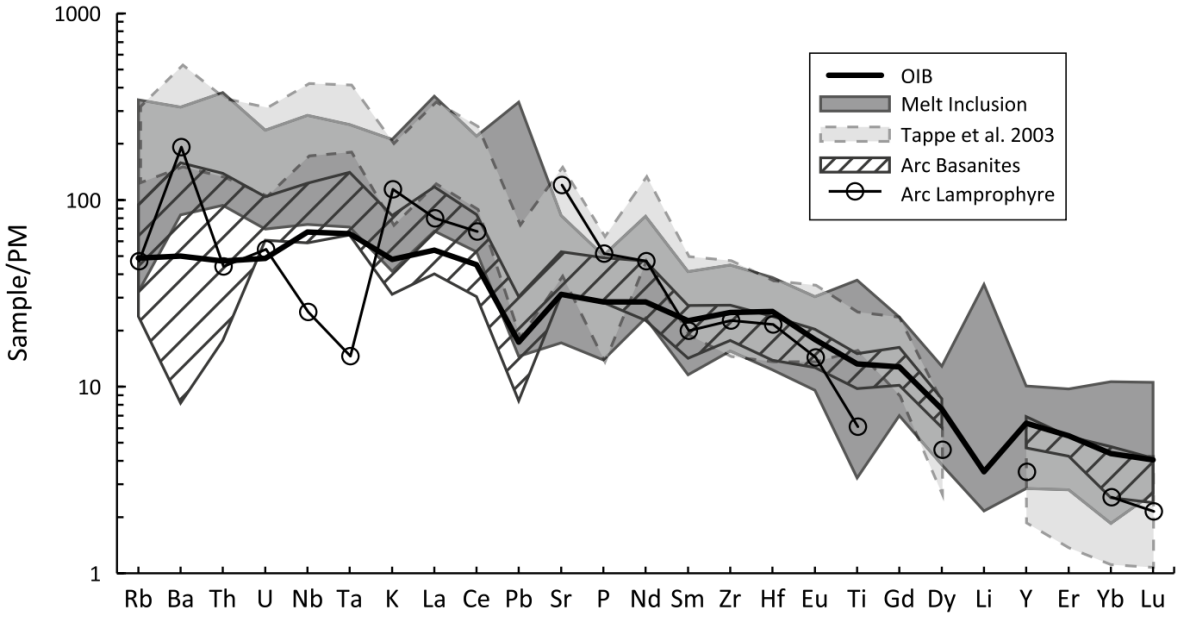

Figure 2.10 Primitive-mantle normalized (Sun and McDonough 1989) multi-element plot comparing analyzed melt inclusion data (shaded field) with ocean island basalt (OIB; Sun and McDonough 1989), similar Toro-Ankole rocks from Tappe et al. (2003), average arc basanite, and average Mexican arc lamprophyre (Luhr 1997). Average arc basanite was calculated from GEOROC database (http://georoc.mpch-mainz.gwdg.de/georoc/) and is defined as ±1σ of the average of 128 analyses from 17 studies (Rafferty and Heming 1979; Baker et al 1981; Hirai and Arai 1986; Hole 1988; Davis et al 1993; El Azzouzi et al 1999; D'Orazio et al 2000; Beccaluva et al 2002; Gorring et al 2003; Duggen et al 2005; Espinoza et al 2005; Ichiyama and Ishiwatari 2005; Massaferro et al 2006; Perepelov et al 2006; Orozco-Esquivel et al 2007; Chang et al 2009; Espíndola et al 2010). The melt inclusion data are more enriched in the large ion lithophile elements (LILE) than OIB and overlap with the LILE concentrations of average arc basanite. Some melt inclusions show the Ti depletion commonly associated with arc magmatism, but lack similar depletions in Nb and Ta. Melt inclusion data also show an enrichment in Li relative to OIB, commonly associated with fluids driven off of a subducting slab

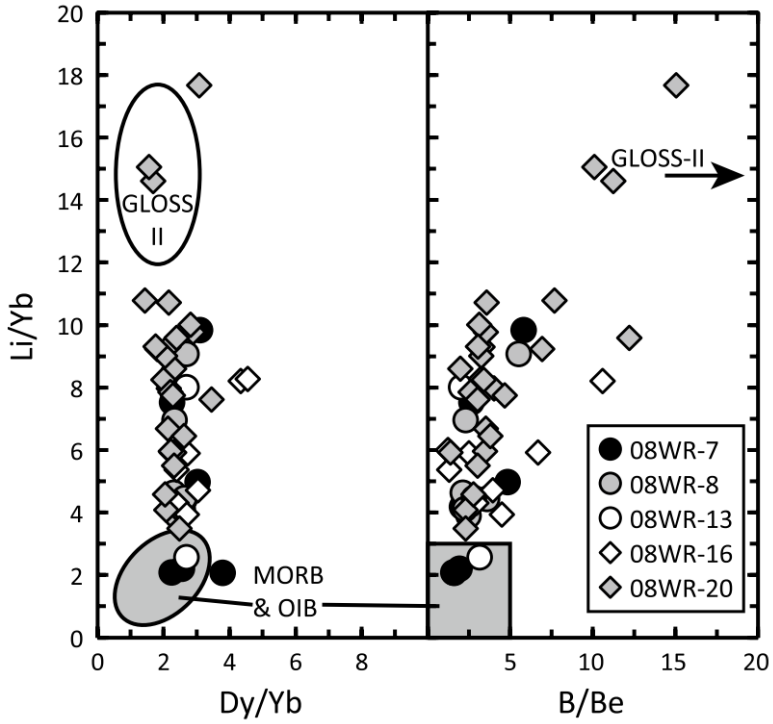

Figure 2.11 Li/Yb vs. Dy/Yb, and Li/Yb vs. B/Be for melt inclusions. Li and Dy have similar compatibilities in the mantle and are expected to behave the same during partial melting and, due to the similar concentrations of Li and Dy expected in mantle peridotite, the Li/Yb vs. Dy/Yb values should follow a 1:1 line. As such, should edge-effects play any role in the trace element concetrations it is expected that Li and Dy would be concentrated equally. Elevated Li/Yb is expected to be a result of fluid migration off a subducting slab as Li is highly fluid mobile and Dy is not. Measured inclusions trend away from MORB and OIB towards high values of Li/Yb, approaching the GLOSS-II composition. B/Be is also used as a slab fluid tracer as boron volatilizes readily. Measured inclusions trend away from the MORB and OIB field towards the GLOSS-II composition (B/Be = 34±4). GLOSS-II data from Plank (2014). MORB and OIB from Sun and McDonough (1989)

Table 2.1 Whole-rock major-element compositions (wt%)

Sample	SiO_2	TiO_2	Al_2O_3	Fe_2O_3	MnO	MgO	CaO	Na_2O	K_2O	P_2O_5	Total
08WR-1	44.41	3.06	11.83	12.24	0.18	10.52	10.30	2.21	3.11	0.55	98.41
08WR-2	42.05	2.73	8.23	11.80	0.17	17.70	11.15	1.74	2.48	0.43	98.48
08WR-3	43.16	2.52	9.89	12.54	0.18	16.21	9.72	1.99	2.21	0.41	98.83
08WR-4	44.57	3.60	12.55	13.28	0.19	8.84	10.12	1.96	3.02	0.51	98.64
08WR-5	43.08	2.64	10.07	12.57	0.18	15.38	9.99	1.97	2.21	0.42	98.51
08WR-6	44.57	3.66	12.93	13.21	0.19	8.11	9.84	2.07	3.27	0.53	98.38
08WR-7	44.89	3.06	11.43	12.52	0.18	11.79	9.68	1.92	2.88	0.48	98.83
08WR-8	43.13	2.16	8.91	12.09	0.17	19.28	9.11	1.61	1.94	0.36	98.76
08WR-9	44.84	2.96	11.17	12.42	0.18	10.46	11.00	2.02	2.82	0.50	98.37
08WR-10	41.75	3.57	11.75	12.78	0.22	9.13	11.40	2.99	3.71	0.80	98.10
08WR-11	43.29	3.17	9.68	12.21	0.18	11.29	13.87	1.71	2.77	0.46	98.63
08WR-12	43.80	2.79	11.50	11.58	0.19	11.56	9.96	3.01	3.16	0.64	98.19
08WR-13	42.84	2.94	11.40	11.86	0.19	11.67	9.97	3.00	3.28	0.69	97.84
08WR-14	43.18	2.92	11.46	11.89	0.20	11.75	9.85	3.07	3.38	0.70	98.40
08WR-14p	37.19	6.33	9.71	17.51	0.14	11.78	11.24	0.62	2.98	0.07	97.57
08WR-15	43.79	2.51	10.78	11.73	0.18	14.04	9.49	2.50	2.77	0.56	98.35
08WR-16	43.85	2.54	10.83	11.61	0.18	13.53	9.61	2.54	2.72	0.56	97.97
08WR-18	45.36	2.84	11.85	11.54	0.17	9.77	11.17	2.03	2.74	0.50	97.97
08WR-19	54.83	1.57	17.83	7.41	0.16	1.71	4.48	4.06	5.35	0.55	97.95
08WR-20	47.86	3.14	16.21	10.78	0.15	4.57	7.93	2.54	3.89	0.57	97.64
08WR-21	54.89	2.32	14.75	8.82	0.13	3.65	5.47	2.94	4.46	0.50	97.93
08WR-22	59.40	1.69	14.86	6.66	0.09	2.40	3.87	3.01	4.90	0.41	97.29

Table 2.2 Melt-inclusion major element data

Melt Inclusion	SiO_2	TiO_2	Al_2O_3	FeO_T	MnO	MgO	CaO	Na_2O	K_2O	P_2O_5	Original Total	P.E.C. Correction
08WR-7-10	44.29	3.86	10.98	10.78	0.24	9.41	15.80	2.03	2.06	0.53	97.65	-3
08WR-7-11	43.76	4.85	12.61	9.88	0.14	7.37	14.34	2.72	3.76	0.58	95.93	5
08WR-7-15	42.74	4.26	9.48	17.14	0.21	14.20	7.45	2.32	1.58	0.52	97.59	14
08WR-7-16	40.23	4.65	12.66	9.57	0.12	9.09	16.51	2.45	4.11	0.64	93.76	7
08WR-7-17	45.63	4.21	16.24	9.03	0.05	5.15	11.87	2.87	4.17	0.74	98.21	-15
08WR-7-18	43.95	4.40	14.79	8.41	0.07	7.80	13.59	2.67	3.69	0.64	97.66	-6
08WR-7-2	41.56	4.26	14.48	8.28	0.11	7.44	16.72	2.96	3.65	0.52	96.80	-7
08WR-7-3	43.24	3.15	11.77	15.52	0.27	11.84	9.27	1.79	2.60	0.62	98.28	14
08WR-7-4	38.72	4.44	10.88	9.77	0.17	10.07	17.89	3.33	3.69	1.03	96.86	4
08WR-7-5a	44.52	3.78	11.19	13.05	0.24	11.75	10.20	1.93	2.69	0.65	97.57	1
08WR-7-5b	45.68	4.11	12.03	7.74	0.13	6.56	15.40	2.40	4.88	1.09	97.33	1
08WR-7-7a	39.34	5.35	10.79	8.90	0.17	9.31	18.68	2.84	3.93	0.67	94.56	11
08WR-7-7b	39.84	5.72	11.27	6.89	0.16	7.25	21.10	2.86	4.22	0.68	94.46	4
08WR-7-8	42.67	4.87	11.38	8.50	0.17	8.63	16.10	2.91	4.09	0.70	96.63	6
08WR-8-1	43.76	3.90	10.41	10.11	0.17	9.04	17.59	1.44	3.20	0.41	97.56	3
08WR-8-10a	42.28	4.19	10.48	11.39	0.17	10.38	16.56	1.67	2.41	0.54	97.07	7
08WR-8-10b	44.33	3.19	12.61	11.90	0.19	10.81	10.39	3.05	2.91	0.62	98.29	0
08WR-8-11	44.69	3.79	11.96	9.96	0.16	9.29	14.84	2.88	1.86	0.51	97.65	-4
08WR-8-13b	48.35	1.21	15.06	16.51	0.23	4.08	5.67	2.98	5.09	0.86	97.72	3
08WR-8-14	46.60	2.92	14.18	10.49	0.20	8.19	10.31	2.88	3.57	0.71	97.29	10
08WR-8-19	44.05	3.53	10.17	10.49	0.16	9.53	18.01	2.01	1.62	0.43	96.82	0
08WR-8-21a	45.38	3.60	12.04	10.25	0.22	9.38	14.99	1.70	1.95	0.57	96.99	7
08WR-8-21b	44.52	4.09	12.02	9.00	0.14	8.26	18.11	1.72	1.65	0.55	96.72	7
08WR-8-2a	41.38	4.25	12.76	9.34	0.16	8.11	18.30	2.76	2.44	0.58	95.34	7
08WR-8-2b	42.59	4.24	13.75	10.47	0.19	9.39	15.18	1.89	1.92	0.50	95.18	11
08WR-8-2c	41.12	4.70	13.10	9.68	0.15	8.62	16.71	2.28	3.13	0.65	96.04	11
08WR-8-3b	42.87	3.86	13.55	9.49	0.16	8.63	15.41	2.09	3.29	0.64	93.73	-1
08WR-8-4	41.86	4.22	10.87	10.74	0.16	9.52	16.35	2.34	3.52	0.61	96.29	12
08WR-8-7	41.90	3.92	12.06	9.96	0.14	9.57	17.21	2.45	2.46	0.46	95.31	7
08WR-8-9a	41.89	4.09	11.39	9.93	0.15	8.90	17.86	2.72	2.25	0.66	98.99	-12
08WR-8-9b	42.06	4.21	9.33	11.06	0.16	10.13	19.36	1.76	1.55	0.54	95.95	13
08WR-8-9c	46.18	3.24	11.11	9.05	0.14	8.22	17.49	2.39	1.56	0.57	97.80	-4
08WR-8-9d	46.36	3.25	11.40	9.00	0.14	8.24	16.55	3.22	1.46	0.38	98.12	0
08WR-13-10	46.36	3.11	13.25	10.15	0.20	9.51	10.02	5.22	1.32	0.77	97.94	11
08WR-13-11a	41.44	3.77	12.80	11.42	0.15	9.62	16.13	2.23	3.87	0.78	95.00	11
08WR-13-2a	45.05	3.13	11.82	11.86	0.18	10.34	13.59	3.55	1.89	0.73	96.80	8
08WR-13-2c	41.80	2.64	11.45	10.15	0.18	8.33	17.48	2.68	3.44	0.78	95.72	11
08WR-13-3	43.39	3.37	9.97	15.71	0.19	14.09	14.05	2.76	1.55	0.64	97.89	9
08WR-13-4	45.50	3.24	12.23	10.20	0.15	9.02	16.35	2.41	1.49	0.48	96.98	-5
08WR-13-5a	41.56	3.70	11.01	10.49	0.13	9.46	18.08	2.86	3.27	0.74	96.06	1
08WR-13-6	42.21	5.22	12.20	10.20	0.23	8.65	14.92	5.73	0.62	0.65	97.51	0
08WR-16-1	43.56	3.33	11.94	12.86	0.26	12.29	9.18	2.95	2.95	0.70	97.79	7
08WR-16-10	44.36	3.63	10.55	9.59	0.13	8.58	17.69	1.87	2.99	0.62	97.74	-1
08WR-16-11a	43.83	3.71	10.70	11.20	0.19	9.83	16.22	2.36	1.52	0.46	97.54	4
08WR-16-11b	41.68	4.09	9.64	12.05	0.19	10.77	16.60	1.96	2.43	0.64	96.58	12
08WR-16-12	44.53	3.24	12.50	11.19	0.22	10.32	10.62	2.94	3.77	0.67	98.37	-2

Elements in wt% post PEC-correction

Table 2.2 Melt-inclusion major element data (cont'd)

Melt Inclusion	SiO_2	TiO_2	Al_2O_3	FeO_T	MnO	MgO	CaO	Na_2O	K_2O	P_2O_5	Original Total	P.E.C. Correction
08WR-16-13	44.71	3.52	10.38	9.77	0.19	9.37	16.83	2.23	2.35	0.66	96.40	2
08WR-16-15	44.11	4.09	11.14	9.84	0.18	8.82	15.98	2.57	2.66	0.63	96.77	-3
08WR-16-2a	43.33	3.41	10.19	11.05	0.19	9.49	17.04	1.02	3.64	0.61	96.91	-4
08WR-16-2b	42.48	3.46	10.34	15.25	0.28	13.98	8.88	2.94	1.77	0.70	97.85	10
08WR-16-3	44.79	2.98	12.25	10.89	0.15	10.86	11.32	2.76	3.35	0.64	97.40	0
08WR-16-5a	43.82	3.33	11.33	10.90	0.19	10.96	13.40	2.99	2.21	0.85	95.76	3
08WR-16-5b	44.42	3.59	10.85	10.18	0.20	9.89	16.00	2.60	1.76	0.50	96.54	4
08WR-16-5c	43.48	4.37	12.52	8.78	0.15	8.46	15.13	2.37	3.76	0.98	96.40	4
08WR-16-5d	44.86	3.69	10.62	8.68	0.19	8.60	18.32	1.66	2.74	0.64	97.10	6
08WR-16-6	44.65	3.65	13.50	9.34	0.15	8.30	12.85	2.50	4.23	0.86	95.66	10
08WR-16-7	44.84	2.86	12.85	11.93	0.19	10.87	10.09	3.54	2.31	0.62	96.81	17
08WR-16-8	42.88	3.83	12.22	9.46	0.16	8.43	15.21	2.59	4.51	0.74	96.22	8
08WR-20-10a	49.16	2.92	13.84	15.21	0.25	3.95	6.92	2.70	4.25	0.81	98.35	-5
08WR-20-12a	42.14	6.26	12.51	21.22	0.35	5.75	5.89	1.91	3.22	0.71	97.79	-7
08WR-20-12b	45.05	4.20	13.39	17.92	0.28	4.79	7.64	2.62	3.53	0.56	97.84	-4
08WR-20-13a	46.08	4.19	14.89	15.65	0.23	4.16	6.84	3.30	3.88	0.71	98.67	-15
08WR-20-13b	49.99	3.23	15.50	12.88	0.24	3.28	6.19	2.69	5.13	0.79	99.18	-21
08WR-20-13c	46.11	4.16	15.23	15.45	0.25	3.90	7.55	2.97	3.64	0.66	98.38	-16
08WR-20-14b	44.11	2.98	15.71	18.59	0.26	4.61	6.61	2.89	3.50	0.66	98.22	-11
08WR-20-14c	47.57	3.12	13.36	18.55	0.34	4.65	4.97	2.37	4.27	0.73	98.22	-7
08WR-20-14d	50.20	0.83	19.81	11.21	0.19	2.59	8.26	3.01	3.20	0.54	99.18	-17
08WR-20-14e	42.37	6.36	11.05	23.62	0.38	6.16	4.41	1.58	3.40	0.66	96.69	-2
08WR-20-15c	50.44	1.89	13.93	15.46	0.23	4.02	5.77	2.97	4.55	0.72	98.90	0
08WR-20-15d	42.29	6.30	12.66	19.80	0.29	5.29	6.47	2.18	4.05	0.67	98.09	-2
08WR-20-15e	50.24	2.92	15.66	12.15	0.21	2.90	6.68	3.32	5.12	0.78	98.96	-14
08WR-20-15f	38.96	7.23	10.59	25.68	0.37	6.78	5.48	1.69	2.59	0.72	99.01	6
08WR-20-15g	49.29	2.87	15.47	14.20	0.21	3.46	6.16	2.42	5.19	0.69	98.73	-17
08WR-20-16a	48.65	2.87	14.01	15.59	0.27	3.99	6.91	2.56	4.40	0.76	98.66	0
08WR-20-16b	35.86	8.84	9.98	28.08	0.44	7.68	5.46	1.27	1.94	0.53	99.06	6
08WR-20-17a	45.98	3.72	14.30	16.33	0.26	4.25	7.41	3.12	3.77	0.73	98.71	-14
08WR-20-18	35.90	8.30	10.51	28.93	0.39	7.54	3.04	2.02	2.92	0.43	100.09	-3
08WR-20-19	48.69	3.28	14.15	16.80	0.29	4.16	4.93	2.20	4.87	0.70	98.43	-13
08WR-20-1a	50.36	3.79	15.96	10.94	0.18	2.57	7.70	2.50	5.20	0.84	97.29	-23
08WR-20-1b	51.27	3.69	16.43	10.03	0.19	2.30	7.73	2.65	4.97	0.77	98.47	-25
08WR-20-2	49.87	3.20	15.89	11.34	0.21	2.65	7.49	3.37	4.95	0.81	99.12	-19
08WR-20-20	51.11	1.51	21.35	8.01	0.14	1.60	9.13	3.53	3.50	0.46	98.80	-26
08WR-20-21a	49.16	4.21	16.70	10.11	0.16	3.52	6.58	3.35	5.32	0.83	98.72	-15
08WR-20-21b	50.18	4.46	17.54	6.00	0.10	1.75	10.59	3.33	5.33	0.64	99.10	-23
08WR-20-22a	38.49	6.24	11.06	26.00	0.30	6.89	4.21	2.79	3.49	0.52	98.90	-7
08WR-20-22b	49.39	2.67	14.38	14.47	0.26	3.70	7.00	3.06	4.29	0.77	98.64	-10
08WR-20-23a	43.55	4.94	12.02	17.27	0.24	4.57	14.42	1.31	1.31	0.34	97.80	-13
08WR-20-23b	47.12	4.51	14.51	15.04	0.26	3.96	6.84	3.07	3.96	0.70	98.55	-9
08WR-20-24a	49.62	2.52	14.73	13.89	0.26	3.77	6.95	2.99	4.54	0.72	98.93	-8
08WR-20-24b	50.09	2.55	15.27	12.82	0.20	3.23	7.28	3.13	4.67	0.75	98.99	-12
08WR-20-25	39.10	4.16	9.72	23.80	0.28	7.01	12.16	1.80	1.66	0.44	97.73	8

Elements in wt% post PEC-correction

P.E.C. Correction in %, where positive numbers represent olivine addition and negative numbers represent olivine subtraction

Table 2.2 Melt-inclusion major element data (cont'd)

Melt Inclusion	SiO_2	TiO_2	Al_2O_3	FeO_T	MnO	MgO	CaO	Na_2O	K_2O	P_2O_5	Original Total	P.E.C. Correction
08WR-20-3a	42.83	5.46	13.24	19.76	0.29	5.17	6.08	2.65	3.92	0.58	98.64	-4
08WR-20-3b	41.00	6.09	13.86	20.23	0.24	5.17	5.50	2.96	4.22	0.66	98.67	-11
08WR-20-4a	47.31	3.16	16.15	11.81	0.20	4.91	8.99	2.79	4.11	0.56	97.49	-5
08WR-20-4b	46.40	3.42	15.63	12.61	0.21	5.22	9.52	2.65	3.74	0.60	98.22	-8
08WR-20-5	47.73	4.11	15.86	10.37	0.16	2.77	12.11	2.78	3.51	0.58	98.26	-24
08WR-20-6	49.37	2.66	14.48	14.24	0.26	3.76	6.99	3.02	4.43	0.73	98.58	-10
08WR-20-7a	47.70	2.94	13.72	17.57	0.40	4.70	6.82	1.85	3.23	0.79	96.71	-13
08WR-20-7b	46.46	3.54	12.85	18.05	0.33	4.94	7.08	2.49	3.65	0.64	97.97	1
08WR-20-8a	48.23	3.10	13.88	16.08	0.27	4.11	7.16	2.50	3.88	0.73	98.99	-10
08WR-20-9	48.64	3.02	14.27	15.11	0.25	3.65	7.00	2.96	4.33	0.73	98.70	-11

Elements in wt% post PEC-correction

P.E.C. Correction in %, where positive numbers represent olivine addition and negative numbers represent olivine subtraction

Table 2.3 Whole-rock trace-element abundances (μg g^{-1})

Sample	Ba	La	Ce	Pr	Nd	Sm	Eu	Gd	Y	Dy	Ho	Er	Lu	Yb	Tb	V	Cr	Nb	Hf	Ta	Pb	Th	U
08WR-1	955	80.0	147.0	16.7	62.7	10.6	2.69	7.85	26.4	5.22	0.99	2.54	0.32	2.23	1.05	278.4	602.1	90.2	6.56	5.77	5.39	11.9	2.18
08WR-2	935	64.3	119.7	13.4	50.2	8.4	2.23	6.19	19.0	3.77	0.68	1.72	0.22	1.47	0.78	268.9	1396.7	78.2	5.19	4.87	3.71	8.6	1.65
08WR-3	750	56.9	107.4	12.4	47.4	8.3	2.17	6.44	23.1	4.41	0.83	2.09	0.26	1.82	0.86	255.6	1327.6	69.1	5.17	4.32	4.40	8.7	1.57
08WR-4	1021	78.1	144.3	16.5	61.6	15.0	2.66	7.96	28.6	5.33	1.01	2.65	0.34	2.33	1.06	334.4	336.3	94.2	6.93	6.12	5.16	11.7	1.95
08WR-5	784	58.7	111.5	12.8	48.7	8.4	2.19	6.57	23.5	4.38	0.82	2.17	0.27	1.83	0.88	270.7	1195.5	68.8	5.01	4.23	4.04	8.9	1.55
08WR-6	1022	80.0	146.2	16.9	62.7	10.8	2.78	7.95	29.0	5.63	1.04	2.68	0.36	2.41	1.11	332.9	293.8	97.0	7.00	6.21	4.92	11.8	1.89
08WR-7	888	72.0	135.4	15.1	56.1	12.4	2.37	7.19	25.7	4.82	0.92	2.35	0.31	2.10	0.95	292.5	825.1	86.5	5.99	5.41	4.95	10.5	1.86
08WR-8	678	51.0	98.0	11.2	42.8	10.6	1.92	5.65	21.0	3.95	0.74	1.88	0.24	1.64	0.78	240.2	1755.5	61.6	4.38	3.84	4.12	7.9	1.43
08WR-9	880	74.4	139.7	15.7	58.7	9.8	2.56	7.63	26.2	4.96	0.92	2.39	0.31	2.07	0.99	303.9	493.4	88.5	6.24	5.57	5.07	11.0	1.99
08WR-10	1031	124.5	220.1	24.5	89.6	14.2	3.61	10.02	30.3	6.00	1.11	2.79	0.34	2.37	1.28	333.5	387.0	158.5	8.29	9.38	6.92	17.2	2.69
08WR-11	840	67.8	128.9	14.9	56.7	9.3	2.42	6.90	21.6	4.39	0.80	1.97	0.23	1.60	0.90	360.8	645.4	79.3	5.78	5.00	3.54	9.2	1.83
08WR-12	1098	110.3	198.1	22.0	79.1	12.4	3.16	8.95	28.4	5.52	1.04	2.61	0.34	2.30	1.16	255.3	803.7	131.9	7.15	7.68	7.37	16.8	3.16
08WR-13	1088	111.9	201.2	22.4	82.6	12.9	3.24	9.22	28.8	5.60	1.04	2.63	0.33	2.31	1.17	262.5	729.8	139.8	7.40	8.06	7.51	17.3	3.23
08WR-14	1075	111.7	202.4	22.3	80.5	12.7	3.21	9.27	28.9	5.59	1.04	2.63	0.34	2.26	1.19	262.7	786.5	137.1	7.18	7.97	7.58	17.3	3.35
08WR-14p	1111	16.6	35.7	5.2	24.2	6.2	1.60	4.61	15.1	3.09	0.56	1.37	0.16	1.11	0.61	908.0	130.4	29.4	3.95	1.98	1.37	2.1	0.35
08WR-15	983	92.3	169.9	18.7	68.0	11.0	2.76	8.02	26.4	5.05	0.94	2.36	0.31	2.12	1.04	250.8	1092.5	111.5	6.37	6.58	6.22	14.8	2.77
08WR-16	1011	94.6	173.2	19.2	70.0	11.1	2.79	8.06	26.3	5.02	0.95	2.39	0.31	2.11	1.04	255.1	1027.9	112.7	6.36	6.56	6.28	14.7	2.76
08WR-18	935	74.3	137.3	15.6	58.6	19.6	2.54	7.60	27.0	5.05	0.95	2.46	0.32	2.15	1.00	303.3	588.3	89.1	6.14	5.52	4.69	10.9	1.88
08WR-19	1408	132.6	237.5	23.7	81.1	12.3	3.07	8.75	30.0	5.59	1.07	2.78	0.41	2.71	1.14	79.3	0.9	147.4	9.36	8.63	17.74	29.1	4.76
08WR-20	1241	96.4	172.3	18.8	68.0	11.1	2.79	8.33	30.2	5.57	1.07	2.79	0.38	2.55	1.12	261.3	102.1	102.2	7.43	6.34	6.68	16.8	2.25
08WR-21	1240	120.8	228.9	23.8	84.8	13.7	2.64	9.54	30.5	5.81	1.08	2.80	0.38	2.60	1.22	211.2	42.0	104.2	8.39	6.29	11.13	26.7	4.47
08WR-22	1197	116.4	213.5	22.4	79.6	13.7	2.14	8.74	26.0	4.89	0.89	2.36	0.33	2.20	1.04	152.3	30.6	99.5	8.12	5.81	19.03	34.4	6.27

Table 2.4 Melt-inclusion trace-element data (μg g^{-1})

Sample	7-4	7-5a	7-5b	7-10	7-15	7-17	7-18	8-2a	8-2b	8-2c	8-9a	8-10a	8-10b	8-15	13-3	13-5a	16-1	16-3
Ni	214	15	1591	2879	17	35	306	11694	247	1092	50	861	88	42	163	3054	34	177
Cu	100	68	21	145	97	8	13	6337	390	397	124	268	219	283	131	239	254	116
V	551	314	407	322	577	349	455	439	462	458	176	462	271	320	339	431	290	296
Sc	40	28	53	60	31	34	38	42	47	56	34	45	20	27	40	50	17	30
Cr	939	890	2378	4332	1735	1260	897	1802	4054	8428	2849	1270	393	2530	3458	1431	1563	2154
Co	72	35	452	332	69	49	108	581	105	212	53	112	56	48	49	242	56	60
Au	0.08	0.07	N.D.	0.28	0.09	0.07	0.13	0.17	0.32	0.21	N.D.	0.10	0.06	0.27	0.53	N.D.	0.06	0.05
Be	2.6	3.0	3.0	1.5	2.1	2.0	2.3	2.4	3.3	3.8	2.0	3.2	2.2	4.6	2.5	2.4	2.8	2.5
B	4.1	6.1	14.4	8.5	5.5	3.1	4.4	5.9	7.4	10.7	10.8	11.5	4.7	10.5	5.1	7.6	3.6	3.1
Rb	102.6	75.6	183.2	47.1	35.3	90.5	104.8	31.2	45.5	89.8	20.5	85.5	78.5	24.3	39.7	85.8	85.1	103.4
Ba	1562	1071	1827	907	1098	1079	1277	1395	1507	1674	820	1407	1195	1711	806	1284	1518	1180
Th	16.2	17.3	21.2	10.5	14.1	12.0	13.3	18.5	19.4	22.8	10.5	13.3	12.9	24.2	16.7	10.9	22.2	17.5
U	3.63	3.57	3.79	2.12	2.60	2.76	2.50	3.00	3.41	4.07	2.29	2.89	2.73	4.97	3.86	2.27	4.21	3.38
Nb	169.8	144.5	150.5	91.6	118.1	99.0	115.5	138.9	146.8	171.6	82.6	127.4	109.1	202.9	132.5	114.2	179.3	130.2
Ta	8.91	8.61	10.41	6.35	6.66	5.83	7.07	8.24	8.25	9.95	4.48	7.00	6.05	10.03	7.81	7.04	9.64	7.25
La	140.9	102.2	125.6	80.8	91.2	83.8	94.8	116.8	122.2	133.4	73.4	137.4	87.6	140.3	124.4	91.9	147.7	108.3
Ce	285.0	213.1	271.6	182.7	183.3	168.5	201.8	230.0	245.0	285.0	157.5	227.0	173.7	284.3	262.2	189.4	280.4	220.6
Pb	4.0	13.4	2.7	7.8	12.4	7.0	6.1	61.7	13.4	13.9	9.5	5.2	8.5	11.6	10.1	4.4	12.5	10.5
Sr	1741	835	1382	714	743	925	1120	1317	1303	1407	768	833	1106	1240	1032	1234	1543	1113
Nd	108	78	101	67	69	70	78	99	103	111	62	95	70	105	95	77	106	81
Sm	15.5	12.2	13.7	11.5	11.0	11.2	11.9	16.1	17.7	18.4	12.4	14.6	11.1	17.5	14.7	14.1	15.6	12.8
Zr	330	356	502	270	292	280	302	377	398	451	252	309	249	413	316	283	348	299
Hf	8.0	8.2	11.9	7.3	7.0	7.4	7.1	9.1	9.7	10.3	6.0	7.6	5.3	8.9	8.0	6.7	7.3	6.6
Eu	4.5	3.0	3.3	3.0	2.8	3.1	3.3	4.5	4.6	5.1	3.3	4.0	3.1	4.1	4.1	3.7	4.2	3.2
Gd	10.7	9.3	8.0	9.6	8.2	8.1	9.4	12.8	13.4	14.1	8.7	10.3	8.3	12.7	10.0	10.1	11.2	8.3
Dy	6.3	6.5	4.5	5.3	5.6	5.8	6.6	8.5	9.1	9.5	6.2	6.1	5.2	8.1	6.1	5.6	6.7	5.4
Li	3.5	11.5	7.4	16.9	18.6	5.4	5.7	13.8	14.5	16.1	20.8	10.3	10.5	24.3	18.0	5.4	15.0	12.9
Y	27.4	30.9	22.9	24.7	28.0	29.1	30.8	40.8	42.2	45.8	26.4	28.6	25.9	40.8	27.3	25.4	31.2	25.7
Er	2.9	3.4	3.0	2.3	2.8	2.9	3.2	4.4	4.6	4.5	3.5	2.7	2.6	4.0	2.9	2.6	3.1	2.6
Yb	1.7	2.8	1.5	1.7	2.5	2.6	2.6	3.5	3.5	3.6	2.3	2.3	2.3	3.5	2.3	2.1	2.8	2.1
Lu	0.26	0.39	0.27	0.24	0.33	0.36	0.36	0.54	0.55	0.49	0.39	0.32	0.32	0.48	0.33	0.36	0.36	0.28

N.D. for samples below the detection limit

Table 2.4 Melt-inclusion trace-element data (μg g^{-1}) (cont'd)

Sample	16-4c	16-5a	16-5b	16-5c	16-5d	16-12	20-2	20-3a	20-3b	20-4a	20-4b	20-5	20-7a	20-7b	20-10a	20-13a	20-13b	20-13c
Ni	354	124	458	634	5383	128	5	404	64	4012	738	26	288	2122	2541	88	16	88
Cu	164	150	165	200	163	101	25	33	27	124	113	368	611	91	57	108	409	67
V	360	325	368	735	533	277	186	1006	1225	314	322	320	206	710	315	452	195	415
Sc	36	21	43	26	60	27	15	24	15	54	25	31	22	63	74	16	18	17
Cr	809	2011	21936	27567	2453	1868	18	763	764	3821	2319	1205	28	631	127	360	12	264
Co	64	119	85	115	443	55	34	326	88	1072	246	51	257	1562	1625	94	50	89
Au	N.D.	0.27	0.85	N.D.	1.01	0.07	0.17	N.D.	0.06	0.52	0.18	0.03	0.14	0.60	0.86	N.D.	0.03	0.08
Be	2.3	3.3	3.0	3.4	4.1	2.2	2.6	2.0	2.4	3.2	2.3	2.4	4.8	2.3	3.4	2.3	2.4	3.3
B	10.2	8.2	9.7	13.5	27.5	6.5	7.7	9.5	6.6	20.1	7.1	9.1	14.6	22.8	26.0	3.1	4.9	7.5
Rb	69.7	41.9	31.7	83.8	90.7	125.4	131.8	142.4	117.0	138.2	116.7	81.8	113.1	113.7	148.4	100.8	128.4	96.4
Ba	1383	1596	1270	2196	1870	1369	1398	1394	1177	1494	1296	1059	1025	1155	1493	1321	1272	1206
Th	7.9	19.8	13.0	16.1	13.0	17.9	19.4	21.0	18.5	21.8	17.7	14.3	32.0	16.2	23.5	17.3	20.2	18.7
U	1.47	3.98	3.05	3.63	3.41	3.30	3.56	3.71	3.26	3.97	3.36	2.22	4.78	2.65	3.47	2.87	3.15	2.94
Nb	94.9	172.8	130.8	178.7	136.3	137.0	103.2	115.6	104.4	109.2	98.8	83.1	168.0	88.8	107.2	107.8	113.3	116.7
Ta	5.33	8.51	6.60	9.44	8.57	7.57	6.11	6.56	5.83	6.79	6.04	5.05	8.12	5.38	7.48	6.11	6.26	6.46
La	246.7	144.7	101.3	142.8	124.6	117.3	101.9	112.4	93.2	108.7	95.5	78.3	125.0	83.2	111.6	99.3	106.6	102.4
Ce	146.7	389.6	191.9	237.8	202.1	223.4	206.6	231.3	182.1	227.3	193.5	154.7	366.3	195.6	233.0	196.3	208.3	201.9
Pb	6.8	17.7	11.9	14.4	10.3	8.7	10.7	11.5	10.3	9.9	8.3	7.4	25.8	11.6	10.3	9.5	9.3	13.7
Sr	651	1593	1294	1606	1192	1306	715	708	714	1056	939	766	496	709	724	1001	605	922
Nd	90	100	78	96	89	90	78	79	66	70	71	64	91	67	83	78	79	78
Sm	12.2	13.4	12.5	15.1	16.2	12.8	11.8	12.0	10.2	10.4	10.8	10.7	14.4	11.2	11.0	13.1	12.8	12.8
Zr	207	287	274	287	303	319	320	350	296	349	309	265	494	305	403	308	341	350
Hf	4.3	5.6	5.7	5.8	8.8	7.3	7.2	7.9	6.5	9.2	7.6	6.5	10.3	7.4	9.5	7.3	7.8	8.0
Eu	3.1	3.8	3.5	4.0	3.5	3.6	2.6	2.9	2.6	2.4	2.7	2.8	2.7	2.7	2.6	3.4	2.8	3.1
Gd	8.3	10.3	8.9	10.0	11.9	9.3	8.7	9.1	7.7	6.7	7.9	8.9	11.2	8.4	10.9	9.9	9.1	9.3
Dy	5.1	6.1	5.2	5.8	4.8	5.7	6.8	6.2	5.2	5.7	5.0	6.2	7.7	5.9	7.5	6.6	6.3	7.1
Li	7.4	13.1	9.4	9.0	12.7	10.3	16.1	21.1	11.6	36.4	17.6	15.3	41.0	57.3	56.4	16.9	23.4	14.0
Y	23.7	27.0	22.2	25.9	23.7	26.8	30.1	30.1	27.3	20.6	23.0	29.0	40.8	32.0	35.2	32.0	30.7	35.9
Er	2.4	2.5	2.2	2.8	2.5	2.9	3.3	3.3	3.0	1.9	2.3	3.3	4.7	3.6	4.5	3.3	3.4	3.9
Yb	1.9	2.2	1.1	1.9	2.1	2.4	2.9	2.7	2.5	1.1	1.8	2.4	4.4	3.8	5.2	2.8	2.7	3.4
Lu	0.27	0.32	0.22	0.20	0.30	0.31	0.36	0.42	0.38	0.23	0.24	0.33	0.73	0.78	0.63	0.40	0.39	0.48

N.D. for samples below the detection limit

Table 2.4 Melt-inclusion trace-element data (μg g^{-1}) (cont'd)

Sample	20-14b	20-14c	20-14d	20-14e	20-15d	20-15e	20-15f	20-15g	20-18	20-19	20-20	20-21a	20-21b	20-23a	20-23b
Ni	13	27	145	7	6	5	6	8	8	180	237	63	20	212	3002
Cu	183	607	21	547	580	18	686	620	810	459	12	66	73	451	135
V	538	201	101	1096	1171	161	1198	223	1311	213	96	184	283	724	601
Sc	10	17	8	19	21	14	21	14	22	20	13	15	29	55	74
Cr	1698	66	524	790	1487	13	1117	315	1490	29	17	79	232	2072	924
Co	67	80	151	57	68	27	43	62	61	169	181	75	39	197	1840
Au	0.15	0.24	0.43	0.24	0.19	0.22	0.15	0.24	0.05	0.10	0.19	0.07	0.06	0.08	0.94
Be	2.0	4.7	1.0	2.9	2.9	2.5	1.9	2.2	3.3	3.2	1.4	1.8	2.4	7.2	2.8
B	8.0	16.1	15.0	7.6	9.5	8.6	13.0	7.7	10.6	11.5	16.5	5.6	5.4	25.2	31.4
Rb	96.4	218.5	92.3	99.8	117.1	133.1	86.5	135.7	109.3	149.9	71.9	127.9	119.9	45.0	154.1
Ba	1086	838	1100	1165	1249	1521	878	1323	1009	1332	989	1437	1279	582	1419
Th	12.5	23.6	10.2	21.4	21.9	23.2	17.3	17.3	20.5	20.8	11.3	20.3	18.8	21.0	16.6
U	2.18	3.92	1.83	3.41	3.26	4.25	2.66	2.54	3.06	3.22	1.81	3.31	2.98	2.06	3.01
Nb	71.9	143.9	58.5	136.9	122.3	123.5	131.5	101.7	128.9	121.7	52.7	121.7	106.4	92.6	98.5
Ta	4.44	7.26	3.71	6.95	6.95	6.52	7.03	5.59	7.58	6.42	2.93	6.92	6.06	5.16	6.10
La	55.3	114.5	46.8	115.0	113.9	124.2	86.7	95.5	104.5	106.7	60.4	111.5	103.1	72.1	89.7
Ce	106.8	240.7	93.6	248.2	224.1	239.1	174.1	183.3	193.5	219.4	118.3	214.8	199.3	162.2	212.1
Pb	9.0	19.6	4.2	14.9	10.6	13.3	12.6	8.4	12.1	11.3	6.3	11.9	11.1	35.0	7.2
Sr	1071	363	1321	559	598	796	437	696	531	606	1037	764	704	396	908
Nd	40	90	32	87	87	89	65	71	76	76	41	79	81	74	72
Sm	5.7	12.8	5.1	14.4	12.9	14.1	10.9	11.1	11.5	12.2	5.7	11.6	12.9	14.0	13.3
Zr	212	377	174	362	354	353	320	303	392	349	175	342	355	365	355
Hf	5.3	8.5	4.1	7.3	7.3	7.9	7.3	7.1	8.8	7.5	3.8	8.2	8.7	9.2	9.3
Eu	1.9	2.7	1.6	2.7	2.9	3.1	2.2	2.5	2.5	2.7	1.8	2.9	3.2	3.0	3.4
Gd	4.8	10.3	4.2	9.7	9.7	9.4	7.2	7.9	8.7	8.7	4.4	8.8	9.9	10.9	9.2
Dy	3.4	6.5	2.8	7.1	6.6	6.2	4.8	5.3	6.1	5.8	3.1	5.2	6.1	8.3	6.4
Li	12.8	26.8	16.1	25.1	28.6	16.6	24.5	17.9	26.9	29.0	12.4	11.4	8.6	26.1	55.2
Y	17.8	33.6	13.0	32.4	33.7	32.4	24.8	26.2	31.2	30.9	15.0	23.6	29.6	41.1	31.8
Er	1.8	3.7	1.3	3.6	3.7	3.5	2.6	2.7	3.1	3.6	1.7	2.3	3.2	4.3	3.3
Yb	1.6	3.3	0.9	3.2	3.1	2.8	2.7	1.8	3.0	2.7	1.3	1.5	2.5	3.9	3.8
Lu	0.25	0.52	0.22	0.44	0.44	0.48	0.32	0.35	0.45	0.49	0.20	0.20	0.28	0.53	0.49

N.D. for samples below the detection limit

Table 2.5 Melt-inclusion volatile concentrations

Melt Inclusion	CO_2	H_2O	F	S	Cl
08WR-7-10	-	1.04	1590	455	621
08WR-7-15	106	1.26	2281	516	839
08WR-7-17	810	0.72	1550	1862	1022
08WR-7-18	882	0.80	2101	2000	1072
08WR-7-4	6056	1.15	2423	3333	2133
08WR-7-5a	2409	1.26	1910	1668	321
08WR-7-5b	791	1.58	1635	1877	1179
08WR-8-10b	206	0.42	1639	1079	969
08WR-8-15	181	0.77	2691	1351	1351
08WR-13-3	472	0.63	1720	401	554
08WR-13-5a	9953	1.55	2402	4032	1325
08WR-16-1	75	0.75	2333	1352	1683
08WR-16-12	300	1.13	1826	1139	1214
08WR-16-3	364	1.18	1792	749	1021
08WR-16-4c	505	1.17	1670	778	241
08WR-16-5a	402	2.53	3429	636	1519
08WR-16-5c	-	2.28	3964	751	938
08WR-16-5d	429	1.25	1827	318	324
08WR-20-10a	1655	0.72	1298	292	537
08WR-20-13a	45	0.64	2406	1879	1267
08WR-20-13b	503	0.71	2171	148	247
08WR-20-13c	-	0.93	2230	552	1062
08WR-20-14b	51	0.69	1348	1775	409
08WR-20-14d	432	0.48	831	205	141
08WR-20-15d	2686	0.89	2032	192	392
08WR-20-15e	122	0.43	1883	365	756
08WR-20-15f	251	0.91	2868	248	396
08WR-20-15g	672	0.57	1357	102	87
08WR-20-18	249	0.98	2508	156	505
08WR-20-19	641	1.07	1824	153	147
08WR-20-2	27	0.40	1751	508	727
08WR-20-20	111	0.47	1012	237	424
08WR-20-21a	59	0.45	2067	865	804
08WR-20-21b	211	0.28	1693	693	680
08WR-20-23a	102	0.72	1436	1249	467
08WR-20-23b	744	0.77	2188	1588	1535
08WR-20-3a	104	0.86	2239	493	892
08WR-20-3b	424	0.60	2112	724	985
08WR-20-4a	7254	0.59	2318	1062	1276
08WR-20-4b	150	0.58	2393	1283	1158
08WR-20-5	200	0.50	1931	984	954
08WR-20-7a	377	0.90	2166	344	741

CO_2, F, S, and Cl in $\mu g\ g^{-1}$, H_2O in wt%

A "-" is present where CO_2 signals failed to stabilize

2.8. REFERENCES

Baker BH, Mohr PA, Williams LAJ (1972) Geology of the Eastern Rift System of Africa. Geol Soc Am Spec Pap 136:1–68. doi: 10.1130/SPE136

Baker BH, Wohlenberg J (1971) Structure and Evolution of the Kenya Rift Valley. Nature 229:538–542.

Baker PE, Rea WJ, Skarmeta J, et al (1981) Igneous History of the Andean Cordillera and Patagonian Plateau around Latitude 46 degrees S. Philos Trans R Soc A Math Phys Eng Sci 303:105–149. doi: 10.1098/rsta.1981.0194

Barifaijo E, Muwanga A, Schumann A (2010) Geochemistry of the Potassic Basalts from the Bufumbira Volcanic Field in Southwestern Uganda. Tanzania J Sci 36:95–112.

Barifaijo E, Owor M, Erima G (2008) Enrichment characteristics in the upper mantle xenoliths from the Bufumbira basaltic rocks, southwestern Uganda. African J fo Sci Technol 9:85–101.

Bebout G, Ryan J, Leeman W (1993) B-Be systematics in subduction-related metamorphic rocks: Characterization of the subducted component. Geochim Cosmochim Acta 57:2227–2237.

Beccaluva L, Coltorti M, Di Girolamo P, et al (2002) Petrogenesis and evolution of Mt. Vulture alkaline volcanism (Southern Italy). Mineral Petrol 74:277–297. doi: 10.1007/s007100200007

Berhe S, Desta B, Nicoletti M, Teferra M (1987) Geology, geochronology and geodynamic implications of the Cenozoic magmatic province in W and SE Ethiopia. J Geol Soc London 144:213–226.

Brey G, Green D (1975) The role of CO2 in the genesis of olivine melilitite. Contrib to Mineral Petrol 103:93–103.

Cartigny P, Pineau F, Aubaud C, Javoy M (2008) Towards a consistent mantle carbon flux estimate: Insights from volatile systematics (H2O/Ce, δD, CO2/Nb) in the North Atlantic mantle (14° N and 34° N). Earth Planet Sci Lett 265:672–685. doi: 10.1016/j.epsl.2007.11.011

Chakrabarti R, Basu AR, Santo AP, et al (2009) Isotopic and geochemical evidence for a heterogeneous mantle plume origin of the Virunga volcanics, Western rift, East African Rift system. Chem Geol 259:273–289. doi: 10.1016/j.chemgeo.2008.11.010

Chang JM, Feeley TC, Deraps MR (2009) Petrogenesis of basaltic volcanic rocks from the Pribilof Islands, Alaska, by melting of metasomatically enriched depleted lithosphere,

crystallization differentiation, and magma mixing. J Petrol 50:2249–2286. doi: 10.1093/petrology/egp075

Chorowicz J (2005) The East African rift system. J African Earth Sci 43:379–410. doi: 10.1016/j.jafrearsci.2005.07.019

Corti G (2009) Continental rift evolution: From rift initiation to incipient break-up in the Main Ethiopian Rift, East Africa. Earth-Science Rev 96:1–53. doi: 10.1016/j.earscirev.2009.06.005

D'Orazio M, Agostini S, Mazzarini F, et al (2000) The Pali Aike Volcanic Field, Patagonia: Slab-window magmatism near the tip of South America. Tectonophysics 321:407–427. doi: 10.1016/S0040-1951(00)00082-2

Danyushevsky L, Eggins SM, Fallon TJ, D.M. C (2000) H_2O Abundance in Depleted to Moderately Enriched Mid-ocean Ridge Magmas; Part I: Incompatible Behaviour, Implications for Mantle Storage, and Origin of Regional Variations. J Petrol 41:1329–1364. doi: 10.1093/petrology/41.8.1329

Danyushevsky L, McNeill A, Sobolev A (2002) Experimental and petrological studies of melt inclusions in phenocrysts from mantle-derived magmas: an overview of techniques, advantages and complications. Chem Geol 183:5–24.

Danyushevsky L, Leslie RAJ, Crawford AJ, Durance P (2004) Melt Inclusions in Primitive Olivine Phenocrysts: the Role of Localized Reaction Processes in the Origin of Anomalous Compositions. J Petrol 45:2531–2553. doi: 10.1093/petrology/egh080

Dasgupta R, Hirschmann MM (2006) Melting in the Earth's deep upper mantle caused by carbon dioxide. Nature 440:659–62. doi: 10.1038/nature04612

Dasgupta R, Hirschmann MM, Smith ND (2007) Partial Melting Experiments of Peridotite + CO2 at 3 GPa and Genesis of Alkalic Ocean Island Basalts. J Petrol 48:2093–2124. doi: 10.1093/petrology/egm053

Davis AS, Gunn SH, Gray L-B, et al (1993) Petrology and isotopic composition of Quaternary basanites dredged from the Bering Sea continental margin near Navarin Basin. Can J Earth Sci 30:975–984. doi: 10.1139/e93-081

Dasgupta R, Mallik A, Tsuno K, et al (2013) Carbon-dioxide-rich silicate melt in the Earth's upper mantle. Nature 493:211–5. doi: 10.1038/nature11731

Deering CD, Cole JW, Vogel T A. (2008) A Rhyolite Compositional Continuum Governed by Lower Crustal Source Conditions in the Taupo Volcanic Zone, New Zealand. J Petrol 49:2245–2276. doi: 10.1093/petrology/egn067

Dixon J, Clague D (2001) Volatiles in basaltic glasses from Loihi Seamount, Hawaii: Evidence for a relatively dry plume component. J Petrol 42:627–654.

Dixon J, Stolper E, Holloway J (1995) An experimental study of water and carbon dioxide solubilities in mid-ocean ridge basaltic liquids. Part I: calibration and solubility models. J Petrol 36:1607–1631.

Duggen S, Hoernle K, van den Bogaard P, Garbe-Schönberg D (2005) Post-collisional transition from subduction-to intraplate-type magmatism in the westernmost Mediterranean: Evidence for continental-edge delamination of subcontinental lithosphere. J Petrol 46:1155–1201. doi: 10.1093/petrology/egi013

Ebinger C (1989) Tectonic development of the western branch of the East African rift system. Geol Soc Am Bull 885–903. doi: 10.1130/0016-7606(1989)101<0885

Ebinger C, Deino A, Drake R, Tesha A (1989) Chronology of Volcanism and Rift Basin Propagation: Rungwe Volcanic Province, East Africa. J Geophys Res 94:15758–15803.

Eby GN, Lloyd FE, Woolley AR (2009) Geochemistry and petrogenesis of the Fort Portal, Uganda, extrusive carbonatite. Lithos 113:785–800. doi: 10.1016/j.lithos.2009.07.010

Edgar AD (1987) The genesis of alkaline magmas with emphasis on their source regions: inferences from experimental studies. Geol Soc London, Spec Publ 30:29–52. doi: 10.1144/GSL.SP.1987.030.01.04

Edwards C, Morris J, Thirlwall M (1993) Separating mantle from slab signatures in arc lavas using B/Be and radiogenic isotope systematics. Nature 362:530–533.

El Azzouzi M, Bernard-Griffiths J, Bellon H, et al (1999) Evolution of the sources of Moroccan volcanism during the Neogene. Comptes Rendus l'Académie des Sci - Ser IIA - Earth Planet Sci 329:95–102. doi: 10.1016/S1251-8050(99)80210-9

Espíndola JM, Zamora-Camacho a., Godinez ML, et al (2010) The 1793 eruption of San Martín Tuxtla volcano, Veracruz, Mexico. J Volcanol Geotherm Res 197:188–208. doi: 10.1016/j.jvolgeores.2009.08.005

Espinoza F, Morata D, Pelleter E, et al (2005) Petrogenesis of the Eocene and Mio-Pliocene alkaline basaltic magmatism in Meseta Chile Chico, southern Patagonia, Chile: Evidence for the participation of two slab windows. Lithos 82:315–343. doi: 10.1016/j.lithos.2004.09.024

Ferguson A, Cundari A (1975) Petrological aspects and evolution of the leucite bearing lavas from Bufumbira, South West Uganda. Contrib to Mineral Petrol 50:25–46.

Fischer T (2008) Fluxes of volatiles (H2O, CO2, N2, Cl, F) from arc volcanoes. Geochem J 42:21–38.

Foley SF (1988) The Genesis of Continental Basic Alkaline Magmas— An Interpretation in Terms of Redox Melting. J Petrol Special_Vo:139–161. doi: 10.1093/petrology/Special_Volume.1.139

Foley S (1992) Vein-plus-wall-rock melting mechanisms in the lithosphere and the origin of potassic alkaline magmas. Lithos 28:435–453.

Foley SF, Musselwhite DS, van der Laan SR (1999) Melt Compositions from Ultramafic Vein Assemblages in the Lithospheric Mantle: A Comparison of Cratonic and Non-Cratonic Settings. In: J.J.G. et al. (ed) J.B. Dawson Vol. Red Roof Design Cape Town, pp 238–246

Foley SF, Barth MG, Jenner GA. (2000) Rutile/melt partition coefficients for trace elements and an assessment of the influence of rutile on the trace element characteristics of subduction zone magmas. Geochim Cosmochim Acta 64:933–938. doi: 10.1016/S0016-7037(99)00355-5

Foley SF, Yaxley GM, Rosenthal A., et al (2009) The composition of near-solidus melts of peridotite in the presence of CO2 and H2O between 40 and 60 kbar. Lithos 112:274–283. doi: 10.1016/j.lithos.2009.03.020

Furman T, Graham D (1999) Erosion of lithospheric mantle beneath the East African Rift system: geochemical evidence from the Kivu volcanic province. Lithos 48:237–262.

Furman T (2007) Geochemistry of East African Rift basalts: An overview. J African Earth Sci 48:147–160. doi: 10.1016/j.jafrearsci.2006.06.009

Gao J, John T, Klemd R, Xiong X (2007) Mobilization of Ti–Nb–Ta during subduction: evidence from rutile-bearing dehydration segregations and veins hosted in eclogite, Tianshan, NW China. Geochim Cosmochim Acta 71:4974–4996.

Gee LL, Sack RO (1988) Experimental Petrology of Melilite Nephelinites. J Petrol 29:1233–1255.

George R, Rogers N, Kelley S (1998) Earliest magmatism in Ethiopia: evidence for two mantle plumes in one flood basalt province. Geology 26:923–926. doi: 10.1130/0091-7613(1998)026<0923

Ghiorso MS, Evans BW (2008) Thermodynamics of Rhombohedral Oxide Solid Solutions and a Revision of the FE-TI Two-Oxide Geothermometer and Oxygen-Barometer. Am J Sci 308:957–1039. doi: 10.2475/09.2008.01

Gorring M, Singer B, Gowers J, Kay SM (2003) Plio-Pleistocene basalts from the Meseta del Lago Buenos Aires, Argentina: Evidence for asthenosphere-lithosphere interactions during slab window magmatism. Chem Geol 193:215–235. doi: 10.1016/S0009-2541(02)00249-8

Green DH, Falloon TJ (1998) Pyrolite: a Ringwood concept and its current expression. The Earth's Mantle: Composition, Structure, and Evolution 311-378.

Green DH (2015) Experimental petrology of peridotites, including effects of water and carbon on melting in the Earth's upper mantle. Phys Chem Miner 42:95–122. doi: 10.1007/s00269-014-0729-2

Guillong M, Meier DL, Allan MM, et al (2008) SILLS: a MATLAB-based program for the reduction of laser ablation ICP-MS data of homogeneous materials and inclusions. Mineral Assoc Canada Short Course 40:328–333.

Guillot B, Sator N (2011) Carbon dioxide in silicate melts: A molecular dynamics simulation study. Geochim Cosmochim Acta 75:1829–1857. doi: 10.1016/j.gca.2011.01.004

Head EM, Shaw AM, Wallace PJ, et al (2011) Insight into volatile behavior at Nyamuragira volcano (D.R. Congo, Africa) through olivine-hosted melt inclusions. Geochemistry, Geophys Geosystems. doi: 10.1029/2011GC003699

Helo C, Longpré M-A, Shimizu N, et al (2011) Explosive eruptions at mid-ocean ridges driven by CO_2-rich magmas. Nat Geosci 4:260–263. doi: 10.1038/ngeo1104

Hirai H, Arai S (1986) Formation of analcime and phillipsite in hydrous basanites from Southwestern Japan. Nueus Jahrb fur Mineral 153:163–176.

Hole MJ (1988) Post-subduction alkaline volcanism along the Antarctic Peninsula. J Geol Soc London 145:985–998. doi: 10.1144/gsjgs.145.6.0985

Hui H, Zhang Y, Xu Z, Behrens H (2008) Pressure dependence of the speciation of dissolved water in rhyolitic melts. Geochim Cosmochim Acta 72:3229–3240. doi: 10.1016/j.gca.2008.03.025

Ichiyama Y, Ishiwatari A (2005) HFSE-rich picritic rocks from the Mino accretionary complex, southwestern Japan. Contrib to Mineral Petrol 149:373–387. doi: 10.1007/s00410-005-0659-6

Jochum KP, Stoll B, Herwig K, et al (2006) MPI-DING reference glasses for in situ microanalysis: New reference values for element concentrations and isotope ratios. Geochemistry, Geophys Geosystems. doi: 10.1029/2005GC001060

Jochum KP, Willbold M, Raczek I, et al (2005) Chemical Characterisation of the USGS Reference Glasses and BIR-1G Using EPMA , ID-TIMS , ID-ICP-MS and LA-ICP-MS. Geostand Geoanalytical Res 29:285–302. doi: 10.1111/j.1751-908X.2005.tb00901.x

Kampunzu A, Bonhomme M, Kanika M (1998) Geochronology of volcanic rocks and evolution of the Cenozoic Western Branch of the East African Rift System. J African Earth … 26:441–461.

Kent a. JR (2008) Melt Inclusions in Basaltic and Related Volcanic Rocks. Rev Mineral Geochemistry 69:273–331. doi: 10.2138/rmg.2008.69.8

Keppler H, Wiedenbeck M, Shcheka SS (2003) Carbon solubility in olivine and the mode of carbon storage in the Earth's mantle. Nature 424:414–6. doi: 10.1038/nature01828

Kessel R, Schmidt MW, Ulmer P, Pettke T (2005) Trace element signature of subduction-zone fluids, melts and supercritical liquids at 120-180 km depth. Nature 437:724–7. doi: 10.1038/nature03971

Kress VC, Carmichael ISE (1991) The compressibility of silicate liquids containing Fe2O3 and the effect of composition, temperature, oxygen fugacity and pressure on their redox states. Contrib to Mineral Petrol 108:82–92.

Larsen LM, Pedersen AK, Sundvoll B, Frei R (2003) Alkali Picrites Formed by Melting of Old Metasomatized Lithospheric Mantle: Manidlat Member, Vaigat Formation, Palaeocene of West Greenland. J Petrol 44:3–38.

Lee C-TA, Leeman WP, Canil D, Li Z-XA (2005) Similar V/Sc Systematics in MORB and Arc Basalts: Implications for the Oxygen Fugacities of their Mantle Source Regions. J Petrol 46:2313–2336. doi: 10.1093/petrology/egi056

Lloyd AS, Plank T, Ruprecht P, et al (2013) Volatile loss from melt inclusions in pyroclasts of differing sizes. Contrib to Mineral Petrol 165:129–153. doi: 10.1007/s00410-012-0800-2

Luhr J (1997) Extensional tectonics and the diverse primitive volcanic rocks in the western Mexican Volcanic Belt. Can Mineral 35:473–500.

Maria AH, Luhr JF (2008) Lamprophyres, basanites, and basalts of the Western Mexican Volcanic Belt: Volatile contents and a Vein-wallrock melting relationship. J Petrol 49:2123–2156. doi: 10.1093/petrology/egn060

Massaferro GI, Haller MJ, D'Orazio M, Alric VI (2006) Sub-recent volcanism in Northern Patagonia: A tectonomagmatic approach. J Volcanol Geotherm Res 155:227–243. doi: 10.1016/j.jvolgeores.2006.02.002

Menzies M, Murthy V (1980) Mantle metasomatism as a precursor to the genesis of alkaline magmas-isotopic evidence. Am J Sci 280-A:622–638.

Michael P (1995) Regionally distinctive sources of depleted MORB: Evidence from trace elements and H2O. Earth Planet Sci Lett 131:301–320.

Muravyeva N, Belyatsky B, Senin V (2014) Clinopyroxene-host disequilibrium (Sr-Nd-Pb isotope systematics) in ultra-potassic magmas from East-African Rift : Implications for magma mixing and source heterogeneity. LITHOS 16:10603. doi: 10.1016/j.lithos.2014.09.011

Oppenheimer C, Moretti R, Kyle PR, et al (2011) Mantle to surface degassing of alkalic magmas at Erebus volcano, Antarctica. Earth Planet Sci Lett 306:261–271. doi: 10.1016/j.epsl.2011.04.005

Orozco-Esquivel T, M. Petrone C, Ferrari L, et al (2007) Geochemical and isotopic variability in lavas from the eastern Trans-Mexican Volcanic Belt: Slab detachment in a subduction zone with varying dip. Lithos 93:149–174. doi: 10.1016/j.lithos.2006.06.006

Papale P, Moretti R, Barbato D (2006) The compositional dependence of the saturation surface of H2O+CO2 fluids in silicate melts. Chem Geol 229:78–95. doi: 10.1016/j.chemgeo.2006.01.013

Pasteels P, Villeneuve M, De Paepe P, Klerkx J (1989) Timing of the volcanism of the southern Kivu province: implications for the evolution of the western branch of the East African Rift system. Earth Planet Sci Lett 94:353–363.

Pearce J, Stern R (2006) Origin of Back-Arc Basin Magmas: Trace Element and Isotope Perspectives. Geophys Monogr Ser 166:63–86.

Perepelov AB, Puzankov MY, Ivanov A V., Filosofova TM (2006) Basanites of Mt. Khukhch: First mineralogical-geochemical data on the Neogene K-Na alkaline magmatism in western Kamchatka. Dokl Earth Sci 409:765–768. doi: 10.1134/S1028334X06050205

Pettke T, Oberli F, Heinrich C a. (2010) The magma and metal source of giant porphyry-type ore deposits, based on lead isotope microanalysis of individual fluid inclusions. Earth Planet Sci Lett 296:267–277. doi: 10.1016/j.epsl.2010.05.007

Pilet S, Baker M, Stolper E (2008) Metasomatized lithosphere and the origin of alkaline lavas. Science (80-) 320:916–919.

Plank T (2014) The Chemical Composition of Subducting Sediments. Treatise on geochemistry 4:607–629.

Plank T, Cooper LB, Manning CE (2009) Emerging geothermometers for estimating slab surface temperatures. Nat Geosci 2:611–615. doi: 10.1038/ngeo614

Platz T, Foley SF, André L (2004) Low-pressure fractionation of the Nyiragongo volcanic rocks, Virunga Province, D.R. Congo. J Volcanol Geotherm Res 136:269–295. doi: 10.1016/j.jvolgeores.2004.05.020

Poli S, Schmidt MW (2002) Petrology of Subducted Slabs. Annu Rev Earth Planet Sci 30:207–235. doi: 10.1146/annurev.earth.30.091201.140550

Rafferty WJ, Heming RF (1979) Quaternary alkalic and sub-alkalic volcanism in South Auckland, New Zealand. Contrib to Mineral Petrol 71:139–150. doi: 10.1007/BF00375430

Roberts EM, Stevens NJ, O'Connor PM, et al (2012) Initiation of the western branch of the East African Rift coeval with the eastern branch. Nat Geosci 5:289–294. doi: 10.1038/ngeo1432

Roden MF, Murthy VR (1985) Mantle Metasomatism. Annu Rev Earth Planet Sci 13:269–296.

Roeder P, Emslie R (1970) Olivine-Liquid Equilibrium. Contrib to Mineral Petrol 29:275–289.

Rogers NW, De Mulder M, Hawkesworth CJ (1992) An enriched mantle source for potassic basanites: evidence from Karisimbi volcano, Virunga volcanic province, Rwanda. Contrib to Mineral Petrol 111:543–556. doi: 10.1007/BF00320908

Rogers N, James D, Kelley S, De Mulder M (1998) The Generation of Potassic Lavas from the Eastern Virunga Province, Rwanda. J Petrol 39:1223–1247.

Rooney TO, Nelson WR, Dosso L, et al (2014) The role of continental lithosphere metasomes in the production of HIMU-like magmatism on the northeast African and Arabian plates. Geology 42:419–422. doi: 10.1130/G35216.1

Rosenthal A, Foley SF, Pearson DG, et al (2009) Petrogenesis of strongly alkaline primitive volcanic rocks at the propagating tip of the western branch of the East African Rift. Earth Planet Sci Lett 284:236–248. doi: 10.1016/j.epsl.2009.04.036

Rosenthal A, Hauri EH, Hirschmann MM (2015) Experimental determination of C, F, and H partitioning between mantle minerals and carbonated basalt, CO2/Ba and CO2/Nb systematics of partial melting, and the CO2 contents of basaltic source regions. Earth Planet Sci Lett 412:77–87. doi: 10.1016/j.epsl.2014.11.044

Rowe M, Kent A, Nielsen R (2007) Determination of sulfur speciation and oxidation state of olivine hosted melt inclusions. Chem Geol 236:303–322. doi: 10.1016/j.chemgeo.2006.10.007

Ryan J, Langmuir C (1993) The systematics of boron abundances in young volcanic rocks. Geochim Cosmochim Acta 57:1489–1498.

Ryan J, Langmuir CH (1987) The systematics of lithium abundances in young volcanic rocks. Geochim Cosmochim Acta 51:1727–1741.

Ryerson FJ, Watson EB (1987) Rutile saturation in magmas: implications for TiNbTa depletion in island-arc basalts. Earth Planet Sci Lett 86:225–239. doi: 10.1016/0012-821X(87)90223-8

Saal AE, Hauri EH, Langmuir CH, Perfit MR (2002) Vapour undersaturation in primitive mid-ocean-ridge basalt and the volatile content of Earth's upper mantle. Nature 419:451–455. doi: 10.1038/nature01073

Shcheka SS, Wiedenbeck M, Frost DJ, Keppler H (2006) Carbon solubility in mantle minerals. Earth Planet Sci Lett 245:730–742. doi: 10.1016/j.epsl.2006.03.036

Shimizu K, Shimizu N, Komiya T, et al (2009) CO2-rich komatiitic melt inclusions in Cr-spinels within beach sand from Gorgona Island, Colombia. Earth Planet Sci Lett 288:33–43. doi: 10.1016/j.epsl.2009.09.005

Simons K, Dixon J, Schilling J-G, et al (2002) Volatiles in basaltic glasses from the Easter-Salas y Gomez Seamount Chain and Easter Microplate: Implications for geochemical cycling of volatile elements. Geochemistry Geophys Geosystems 3:1–29. doi: 10.1029/2001GC000173

Sobolev A, Shimizu N (1993) Ultra-depleted primary melt included in an olivine from the Mid-Atlantic Ridge. Nature 363:151–154.

Spera F (1981) Carbon dioxide in igneous petrogenesis: II. Fluid dynamics of mantle metasomatism. Contrib to Mineral Petrol 77:56–65.

Sun SS, McDonough WF (1989) Chemical and isotopic systematics of oceanic basalts: implications for mantle composition and processes. Geol Soc London, Spec Publ 42:313–345. doi: 10.1144/GSL.SP.1989.042.01.19

Tappe S, Foley S, Pearson D (2003) The kamafugites of Uganda: a mineralogical and geochemical comparison with their Italian and Brazilian analogues. Period di Mineral 72:51–77.

Tappe S, Foley SF, Kjarsgaard B A., et al (2008) Between carbonatite and lamproite—Diamondiferous Torngat ultramafic lamprophyres formed by carbonate-fluxed melting of cratonic MARID-type metasomes. Geochim Cosmochim Acta 72:3258–3286. doi: 10.1016/j.gca.2008.03.008

Thomsen TB, Schmidt MW (2008) Melting of carbonated pelites at 2.5–5.0 GPa, silicate–carbonatite liquid immiscibility, and potassium–carbon metasomatism of the mantle. Earth Planet Sci Lett 267:17–31. doi: 10.1016/j.epsl.2007.11.027

Tingle TN, Green HW, Finnerty AA (1988) Experiments and Observations Bearing on the Solubility and Diffusivity of Carbon in Olivine. J Geophys Res 93:15289–15304.

Tsuno K, Dasgupta R (2012) The effect of carbonates on near-solidus melting of pelite at 3GPa: Relative efficiency of H_2O and CO_2 subduction. Earth Planet Sci Lett 319-320:185–196. doi: 10.1016/j.epsl.2011.12.007

Vogel T A., Flood TP, Patino LC, et al (2006) Geochemistry of silicic magmas in the Macolod Corridor, SW Luzon, Philippines: Evidence of distinct, mantle-derived, crustal sources for silicic magmas. Contrib to Mineral Petrol 151:267–281. doi: 10.1007/s00410-005-0050-7

Vollmer R, Norry M (1983) Possible origin of K-rich volcanic rocks from Virunga, East Africa, by metasomatism of continental crustal material: Pb, Nd and Sr isotopic evidence. Earth Planet Sci Lett 64:374–386.

Workman RK, Hart SR (2005) Major and trace element composition of the depleted MORB mantle (DMM). Earth Planet Sci Lett 231:53–72. doi: 10.1016/j.epsl.2004.12.005

CHAPTER III

INVESTIGATING MAGMA MIXING THROUGH CHEMICAL AND TEXTURAL OBSERVATIONS OF PLAGIOCLASE FROM MUTNOVSKY VOLCANO, KAMCHATKA

3.1. ABSTRACT

Mixing of compositionally distinct mafic and felsic magmas is seemingly accepted as a ubiquitous process to generate intermediate composition magmas at stratovolcanoes. However, in a majority of studies that invoke this process there are no constraints on the source of the pre-mixed mafic and felsic endmembers or quantitative evaluations of the physicochemical plausibility of mixing. In this study, we investigate the plausibility that mixing of basaltic and dacitic end-member magmas with significantly different initial temperatures and viscosities can mix to produce basaltic andesite erupted from Mutnovsky Volcano, Kamchatka. The plagioclase phenocryst populations in the basaltic and dacitic magmas are compositionally continuous, with their peaks centered in a single range of plagioclase compositions. Plagioclase phenocrysts in the basaltic andesite are strongly bimodal with distinct peaks and a prominent ~10-20 mol% An gap. Significantly, all plagioclase phenocrysts are euhedral in the basalt and dacite lavas, whereas the basaltic andesite contains both a euhedral population and a sieved population of plagioclase. The bimodal plagioclase assemblage in the basaltic andesites cannot be explained by purely fractional crystallization or degassing, but rather is most consistent with hybridization of basalt and dacite to generate basaltic andesite. This is also consistent with published Hf, Sr, Nd and Pb isotope

data and assimilation-fractional crystallization model results that demonstrate that the basaltic, basaltic andesitic and dacitic magmas are genetically related.

3.2. INTRODUCTION

Magma mixing is recognized as a ubiquitous process at stratovolcanoes, which globally erupt magmas that vary in composition from basalt to rhyolite, however the role of magma mixing as a petrological process for driving compositional diversity in arc environments remains controversial. Some studies suggest that magma mixing itself is the dominant process that forms intermediate magma compositions (Reubi and Blundy 2009; Kent et al 2010). However, other studies indicate that intermediate magmas may be generated by partial melting of amphibole-bearing basaltic material in the mid- to lower-crust (Beard and Lofgren 1991; Rapp and Watson 1995; Lange and Carmichael 1996). Some studies suggest that some intermediate magmas may originate by partial melting of the sub-arc mantle (Carmichael 2002; Straub et al 2008). And still other studies suggest that intermediate and high-Si magmas simply reflect the eruption of evolved interstitial liquids that are the product of down-temperature fractional crystallization of mafic magmas (Brophy 1991; Bachmann and Bergantz 2008; MacDonald et al 2008; Dufek and Bachmann 2010). Proponents of the magma mixing hypothesis argue that the presence of mafic and felsic enclaves and mafic and felsic composition melt inclusions in intermediate magmas, and notably a dearth of andesitic composition melt inclusions, are consistent with magma mixing (e.g., Reubi and Blundy 2009). Critics of the magma mixing hypothesis, however, argue that the disparate thermal and compositional differences of mafic and felsic magmas eliminate the possibility of physical mixing as a process responsible for the compositional diversity of arc magmas.

In this study we investigate and present plagioclase phenocryst chemical and textural data of lavas from Mutnovsky volcano, Kamchatka. Mutnovsky has repeatedly erupted basalts, basaltic andesites, andesites, and dacites. Published melt inclusion data, Sr, Nd, Hf, Pb isotope data, and assimilation-fractional crystallization (AFC) model results are consistent with the intermediate composition lavas at Mutnovsky having been the product of mixing of basaltic and dacitic magmas (Robertson et al. 2013; Simon et al. 2014). This previous work provides for a clear comparison of petrologic data with model evidence and melt inclusion evidence for magma mixing.

3.3. BACKGROUND GEOLOGY

Mutnovsky volcano is located ~75 km southwest of Petropavlovsk-Kamchatsky (Figure 3.1). Briefly summarized here from Selyangin (1993), Mutnovsky consists of four superimposed eruptive centers, Mutnovsky I-IV, and lavas span the compositional range from basalt to dacite, from 48.7 to 69.4% SiO_2. Mutnovsky I erupted basaltic to dacitic lavas from ~80-60 ka. Mutnovsky II formed ~3km southeast of the Mutnovsky I crater and erupted basaltic to dacitic lavas from ~40-30 ka. Mutnovsky III formed between the centers of Mutnovsky I and II and erupted basaltic to dacitic lavas. The active Mutnovsky IV has erupted only basalt and basaltic andesite. Across all eruptive centers, basalt and basaltic andesite are dominant, with ~12% of the total erupted volume (~91 km^3) comprised of andesite and dacite (Selyangin, 1993). The compositional diversity at Mutnovsky is similar to most Kamchatka volcanoes, which are composed mainly of basalt and basaltic andesite (i.e., 50-85% of the total mapped rock volume; Volynets 1994; Ponomareva et al 2007).

Simon et al. (2014) investigated the cause(s) for compositional diversity of erupted lavas at Mutnovsky and here we summarize their findings, which are critical to establishing the

magma mixing process that is investigated in the current study. They analyzed fifty unique samples from Mutnovsky I-IV. Across centers of all ages, Mutnovsky lavas define a tholeiitic igneous series with FeO*/MgO generally increasing with increasing SiO_2. Hafnium (ε_{Hf} = 15.3-15.9), Nd (ε_{Nd} ~8.0-9.5), Pb ($^{206}Pb/^{204}Pb$ ~ 18.36; $^{207}Pb/^{204}Pb$ ~ 15.51) and Sr ($^{87}Sr/^{86}Sr$~0.7033) isotope data are similar for samples of all compositions from all four eruptive centers, and indicate that all samples were produced by melting of a similar source material. Simon et al. (2014) reported that fractional crystallization *sensu stricto* cannot explain the origin of basaltic andesites, andesites and dacites from a basaltic source. Dacites from Mutnovsky have trace element patterns that contrast with more mafic rocks from those centers. Notably, Mutnovsky dacites are more depleted in the middle and heavy REEs relative to more mafic lavas from Mutnovsky. If the dacites formed by purely down-temperature fractional crystallization of a more mafic magma, the depleted REE signature of the dacites requires a fractionating phase that preferentially sequesters the REE. Amphibole fractionation can do this; however, model fractional crystallization results indicate that fractionation of 1 to 80 modal % amphibole, using a wide range of amphibole / melt partition coefficients from the Geochemical Earth Reference Model (GERM, earthref.org) database and Hidalgo and Rooney (2010) cannot reproduce the Mutnovsky dacite compositions by fractional crystallization of amphibole from any melt composition less evolved than dacite. Formation of dacite by partial melting of oceanic crust was ruled out based on the absence of a high-Mg#, highly calc-alkaline composition for the Mutnovsky dacites. Simon et al. (2014) concluded that the most plausible explanation for the origin of the dacites involves partial melting of underplated amphibole-bearing basaltic rock in the middle-crust (cf. Beard and Lofgren 1989; Beard and Lofgren 1991; Rapp et al 1991;

Coleman et al 1992; Tepper et al 1993; Rapp and Watson 1995; Lange and Carmichael 1996; Borg and Clynne 1998).

Published experimental studies demonstrate that small to moderate degree partial melts of underplated amphibole-bearing basaltic rock can yield dacitic magma (e.g., Beard and Lofgren 1989; Rushmer 1991; Beard and Lofgren 1991; Rapp et al 1991; Rapp and Watson 1995). The REE patterns for vapor-absent dacitic to rhyodacitic melts produced by experimentally partially melting amphibole-bearing basaltic rock at 8 kbar, and 900 and 1000˚C, are almost identical to the REE signature of the Mutnovsky dacites. To test this partial melting hypothesis, Simon et al. (2014) performed batch melting calculations of amphibole-bearing basaltic rock that contains 60% cpx, 10% ol, and 30% hornblende. The model results indicate that batch melting of 20 to 25% of amphibole-bearing basaltic rock reproduces the REE signature of Mutnovsky dacites. This finding is consistent with a plethora of published studies that have investigated the evolution of chemically evolved silicate magmas in arc environments (e.g., Coleman et al 1992; Atherton and Petford 1993; Tepper et al 1993; Lange and Carmichael 1996; Petford and Atherton 1996; Borg and Clynne 1998; Petford and Gallagher 2001).

Simon et al. (2014) used the the least-squares program XLFRAC (Stormer and Nicholls 1978) to model the major element evolution of Mutnovsky basaltic andesites and andesites. Their model results indicate that 20% fractional crystallization of 6% olivine, 3% clinopyroxene and 91% plagioclase from basalt, combined with assimilation of dacite in a basalt:dacite ratio of 9:1 yields a basaltic andesite composition that is similar to basaltic andesite at Mutnovsky. The sum of the squares of residuals is 1.63 and the fractionating assemblage is consistent with petrographic observations. XLFRAC results also indicate that that a model andesite similar to

andesite at Mutnovsky may be produced by 11% FC of 100% plagioclase from basaltic andesite; the sum of squares of residuals is 1.212.

Model results for the evolution of the REE abundances, performed by using the IgPet software program (Carr 2007), indicate that the REE abundances of basaltic andesite at Mutnovsky can be generated by 15% fractional crystallization of 6% olivine, 3% clinopyroxene and 91% plagioclase from basalt, coupled with assimilation of dacite with R (mass assimilated/mass fractionated) = 0.1. Andesite with a composition similar to that erupted at Mutnovsky can be generated by 8% fractional crystallization of 100% plagioclase, combined with assimilation of dacite with R = 0.4. The consistency between the model results for the major and REE abundances were interpreted by Simon et al. (2014) to indicate that assimilation – fractional crystallization is the most plausible origin for basaltic andesites and andesites at Mutnovksy.

3.4. METHODS

The following analyses were done on a subset of the samples analyzed by Simon et al. (2014). Whole-rock major and trace element compositions of these samples can be found in Table 3.1.

3.4.1. Mineral analysis

The compositions of plagioclase, pyroxene, ilmenite, and magnetite were quantified in thin-section by using a Cameca SX-100 at the Electron Microbeam Analysis Laboratory (EMAL) at the University of Michigan. An accelerating voltage and beam current of 15 kV and 4 nA, respectively, were used to analyze plagioclase, and an accelerating voltage and beam current of 15 kV and 15 nA, respectively, were used to analyze pyroxene, ilmenite, and magnetite. Plagioclase phenocrysts (defined as grains that measured >200 μm) were analyzed

with transects from rim to rim, along the long axis, with 10 to 30 µm spacing between points depending on crystal size size and visually discernible zoning of each grain. Plagioclase microlites (defined as grains that measured <50 µm) were analyzed with a single point or a rim and a core point, size permitting. Pyroxene crystals were analyzed for core and rim compositions. Due to the generally small size of the ilmenite and magnetite crystals, a single analysis was performed at the center of the crystal.

3.4.2. Geothermometry

Temperatures were calculated by using two geothermometers, where possible. Two-pyroxene temperatures were calculated by using the geothermometer of Putirka (2008) on all clinopyroxene-orthopyroxene pairs analyzed in thin section (Table 3.2). Two Fe-Ti oxide temperatures and oxygen fugacities were calculated using the geothermometer of Ghiorso and Evans (2008) on all possible magnetite-ilmenite pairs measured in thin section (Table 3.3).

3.5. RESULTS

Histograms of mol% anorthite (An) of plagioclase phenocrysts and microlites are presented in Figures 3.2-3.4 for representative samples of basalt, basaltic andesite, and dacite from Mutnovsky I, II and III, respectively. Plagioclase phenocrysts from basalt range from ~95 to 60 mol% anorthite and are dominantly An-rich with a peak at ~An_{90-95} and a smaller peak at ~An_{75-80}. Plagioclase phenocrysts in the dacite range from An_{51} to An_{33}, with a peak at ~An_{50-55}. Plagioclase phenocrysts in the basaltic andesite display a bimodal distribution of anorthite compositions with distinct peaks at An_{80-95} and An_{40-50}, and a ~20 mol% An gap between An_{50} and An_{70}. In the basaltic andesite, euhedral plagioclase grains are An-rich, whereas plagioclase grains that display a sieved texture are An-poor (Figs. 3.2-3.4). For basalt and dacite samples, plagioclase microlite compositions are more sodic than co-existing plagioclase phenocrysts,

overlapping slightly with the most sodic phenocrysts. However, plagioclase microlites in the basaltic andesite from Mutnovsky III have compositions that are between the sodic and calcic populations of phenocrysts.

Photomicrographs of representative plagioclase phenocrysts are presented with the mol% An histograms in Figures 3.2-3.4. Plagioclase phenocrysts observed in basalts and dacites erupted from Mutnovsky I-III are all euhedral and do not display any sieved or spongy textures. There are two distinct populations of plagioclase phenocrysts in the Mutnovsky I-III basaltic andesites, a euhedral population displaying no sieved or spongy textures, and a euhedral to subhedral population with very clear sieved and spongy textures. These populations directly correspond to the high An and low An peaks, respectively, observed in the histograms of the basaltic andesites.

Two-pyroxene temperatures (±1σ) range from 1131 ± 15° to 1093 ± 19°C for basaltic lavas, 1086 ± 44° to 1006 ± 35°C for basaltic andesite, and 1032 ± 18° to 997 ± 21°C for dacite (Table 3.2).

3.6. PLAGIOCLASE CHEMICAL AND TEXTURAL EVIDENCE FOR MAGMA MIXING

Plagioclase phenocrysts in Mutnovsky basaltic andesites display a bimodal distribution of anorthite content, with a gap of ~20 mol% An between An-rich and An-poor plagioclase populations, whereas plagioclase compositions in the basalts and dacites all have a single population within a narrow range of anorthite content (Figs. 3.2-3.4). The basaltic andesites contain two textural populations of plagioclase, a euhedral population and a sieved population, whereas the basalts and dacites only contain euhedral plagioclase phenocrysts. The two textural populations in the basaltic andesites correspond with the two distinct chemical populations,

where the euhedral crystals are always the An-rich population and the sieved crystals are always the An-poor population.

There are several petrological processes that can result in compositional and textural diversity of plagioclase phenocrysts in lavas. These include magma decompression, degassing, fractional crystallization, convective mixing of a single magma, and mixing of two compositionally disparate magmas. Nelson and Montana (1992) investigated the effects of decompression on plagioclase texture and chemistry in basaltic andesite and andesite magma compositions by performing experiments with decompression rates ranging from 0.07 to 0.21 MPa/min. They demonstrated experimentally that sieve-textured plagioclase, often invoked as an indicator of magma mixing, can form solely due to decompression. However, they showed that the resulting sieve-textured and euhedral phenocrysts span ~30-60 mol% An, and are chemically indistinguishable from one another (Figure 7 in Nelson and Montana 1992). This is not observed for Mutnovsky samples. Waters and Lange (2013) investigated decompression-induced crystallization in a suite of phenocryst-poor obsidians and reported that rapid decompression during eruption led to the crystallization of sodic plagioclase microlites, all of which had compositions overlapping with those of the plagioclase phenocryst assemblage. Additionally, Waters et al. (2015) experimentally investigated decompression-induced crystallization, finding that their decompression experiments yielded plagioclase compositions more sodic than the range observed in natural samples. These results demonstrate that decompression-induced crystallization yields a wider range of plagioclase compositions, and notably not compositionally distinct plagioclase populations as observed in basaltic andesite lavas from Mutnovsky.

Evolution of the strongly bimodal plagioclase populations in Mutnovsky basaltic andesites seems inconsistent with fractional crystallization, which should result in a continually

decreasing An component with crystallization (Drake 1976; Anderson et al 1982). This is not observed in Mutnovsky basaltic andesites and cannot explain the ~10-20 mol% An gap. Convective mixing has also been proposed to explain disequilibrium textures and compositions in intermediate composition lavas (Murphy et al 2000; Couch et al 2001). In such a scenario, a thermal boundary layer develops in an initially compositionally homogeneous magma chamber that is losing heat at its roof and simultaneously being heated at its base during an underplating event. This may cause convective self-mixing, and the temperature heterogeneity may also result in calcic overgrowths on plagioclase phenocrysts that are not in equilibrium with their rock matrix. We argue that this is also unlikely for Mutnovsky basaltic andesites because of the prominent ~10-20 mol% An gap.

We suggest that the observation that the anorthite peaks in the basaltic andesites correlate with peaks in the basalt and dacite from each eruptive center (Figures 3.2-3.4) is consistent with the hypothesis that the compositionally disparate plagioclase populations crystallized in separate basaltic and dacitic magmas that subsequently mixed physically, and erupted prior to chemically re-equilibrating. Thus, the pre-mixed plagioclase chemistry is preserved. This finding is consistent with the interpretation of assimilation – fractional crystallization model results described above that indicate that Mutnovsky basaltic andesites formed by the mixing of basaltic and dacitic magmas (Simon et al 2014). Mixing must have been vigorous as it was effective at stirring the basaltic and dacitic magmas such that the melt was homogenized on a hand-sample scale, yet dissolution of dacitic plagioclase was incomplete. We do not suggest that the composition of the basalts hosting the plagioclase analyzed represent the basaltic composition that formed the basaltic andesites when mixed with dacite. The basalts have erupted as basalts, suggesting they did not undergo any mixing to form basaltic andesite. The

dacites from which plagioclase were measured have also not mixed, as they erupted as dacites. These plagioclase compositions are used to demonstrate that only the basaltic andesites contain two phenocrysts populations, both chemically and texturally. These observations are consistent with the previous geochemical modeling of Simon et al. (2014) suggesting the mixing of basalt and dacite to form basaltic andesite. This is also consistent with observations from Mt. Hood, Oregon, where crystal size distributions could be linked with chemical data to demonstrate the existence of two compositionally distinct magmas mixing prior to eruption (Kent et al. 2010). Though we know significant viscosity and thermal barriers to magma mixing exist, these observations demonstrate that they can be overcome to result in hybridized magmas.

3.7. CONCLUSIONS

Geochemical modeling of whole-rock and isotope data for lavas from Mutnovsky Volcano, Kamchatka, Russia, is consistent with basaltic andesitic magmas having formed by physical mixing and hybridization of basaltic and dacitic magmas. New results for the variability of compositions of plagioclase phenocrysts and microlites in basaltic, basaltic andesite and dacitic lavas indicate that the bimodal distribution of plagioclase from Mutnovsky basaltic andesites is consistent with physical mixing of basaltic and dacitic magmas that contained An-rich and An-poor plagioclase phenocryst populations, respectively, prior to mixing. The textures of plagioclase in the basaltic andesites are consistent with the resorption of plagioclase originally formed in the dacite end-member owing to a high mixing ratio of basalt:dacite. The results of this study provide physical evidence of the magma mixing proposed at Mutnovsky by previous geochemical modeling efforts.

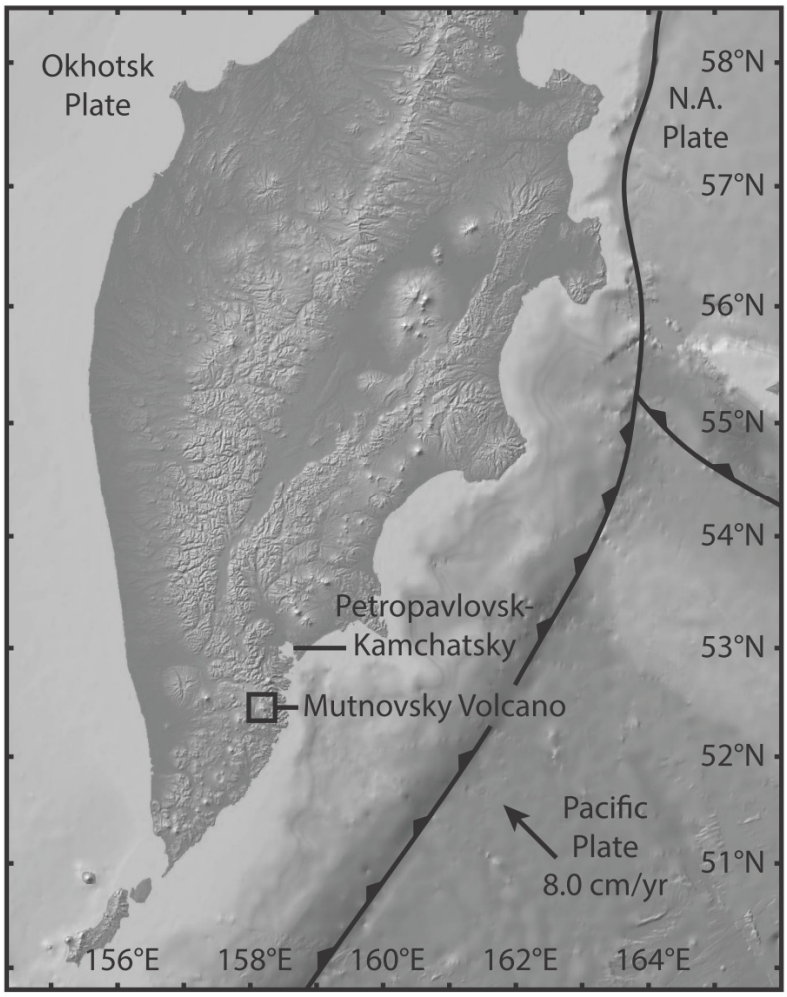

Figure 3.1 A map of the Kamchatka Peninsula showing the location of Mutnovsky Volcano. Map from GeoMapApp (www.geomapapp.org)

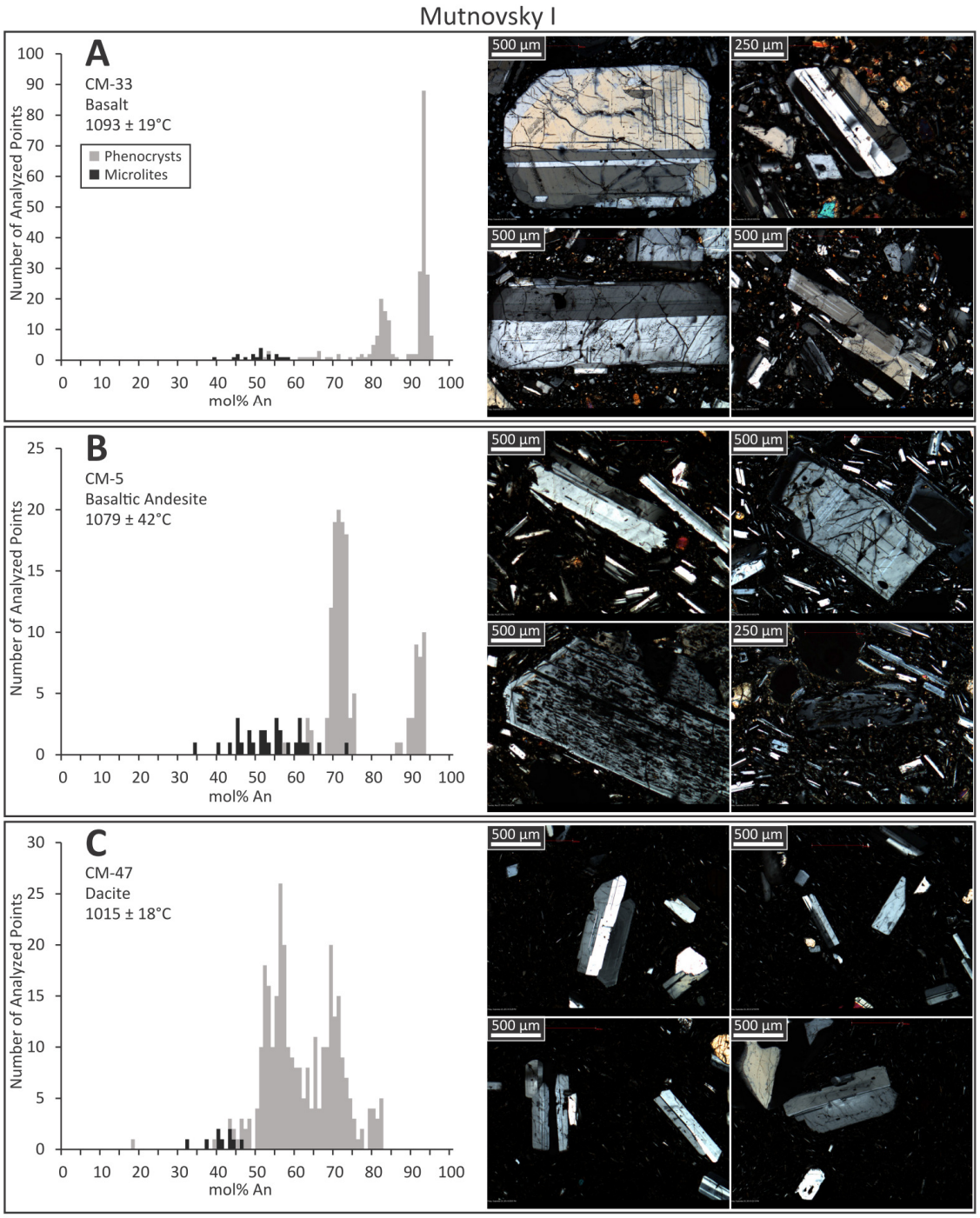

Figure 3.2 Histograms of mol% anorthite from a basalt (a), a basaltic andesite (b), and a dacite (c) from Mutnovsky I. Calculated temperatures (±1σ) are from the two-pyroxene geothermometer of Putirka (2008). For the basalt and dacite the photomicrograph is representative of the plagioclase phenocrysts analyzed. For the basaltic andesite the top two photomicrographs are representative of the anorthite-rich phenocrysts and the bottom two photomicrographs are representative of the anorthite-poor phenocrysts.

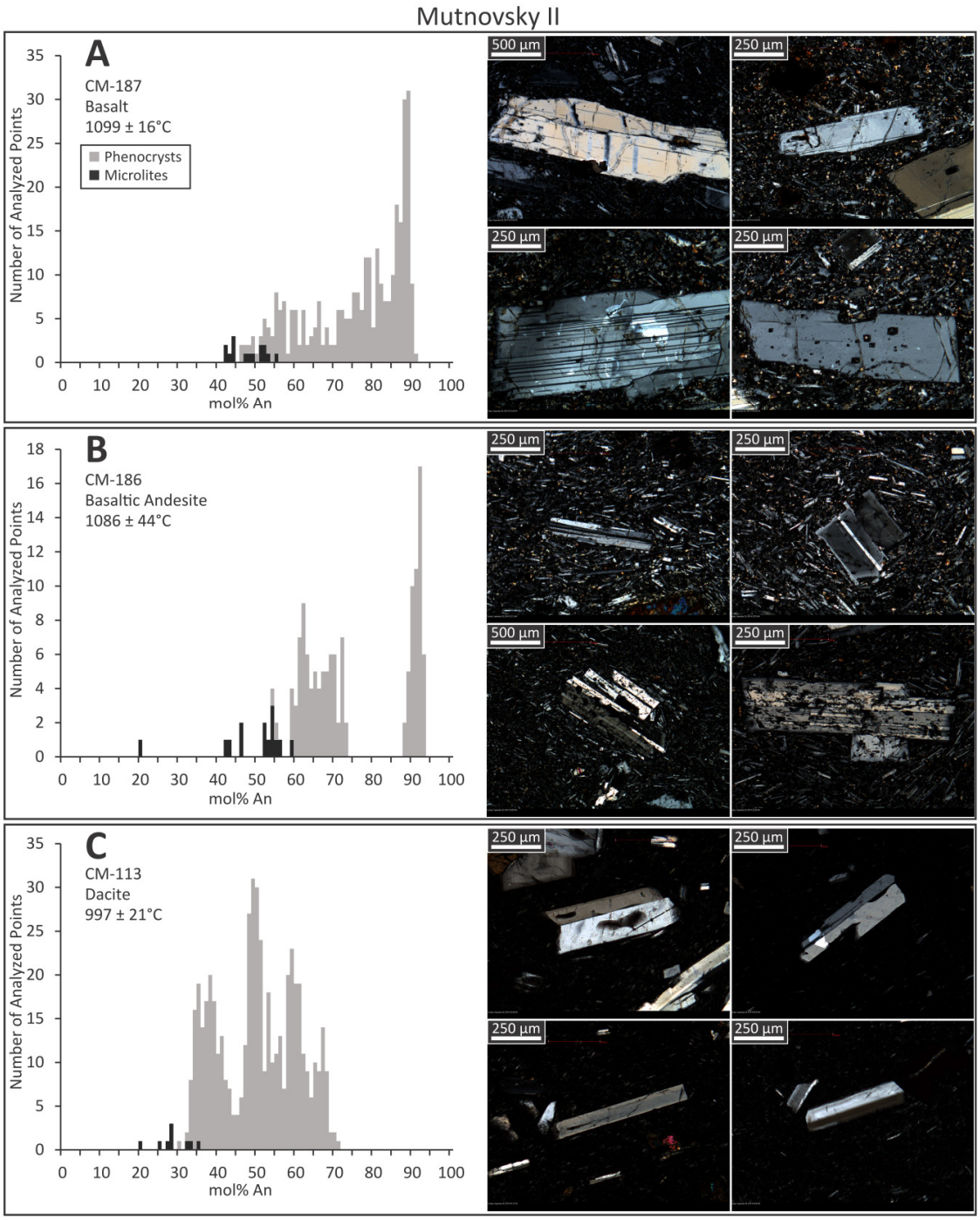

Figure 3.3 Histograms of mol% anorthite from a basalt (a), a basaltic andesite (b), and a dacite (c) from Mutnovsky II. Calculated temperatures (±1σ) are from the two-pyroxene geothermometer of Putirka (2008). For the basalt and dacite the photomicrograph is representative of the plagioclase phenocrysts analyzed. For the basaltic andesite the top two photomicrographs are representative of the anorthite-rich phenocrysts and the bottom two photomicrographs are representative of the anorthite-poor phenocrysts.

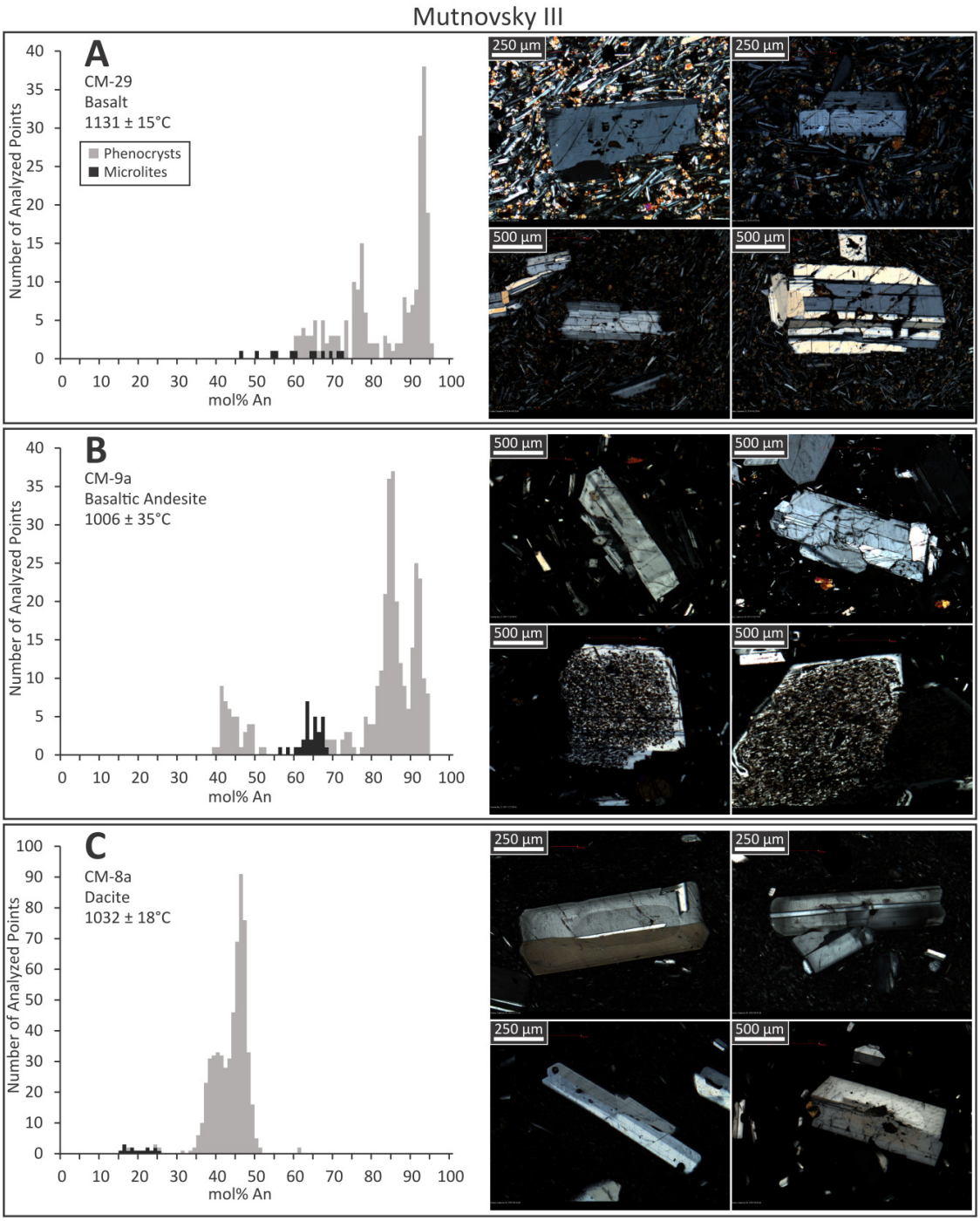

Figure 3.4 Histograms of mol% anorthite from a basalt (a), a basaltic andesite (b), and a dacite (c) from Mutnovsky III. Calculated temperatures (±1σ) are from the two-pyroxene geothermometer of Putirka (2008). For the basalt and dacite the photomicrograph is representative of the plagioclase phenocrysts analyzed. For the basaltic andesite the top two photomicrographs are representative of the anorthite-rich phenocrysts and the bottom two photomicrographs are representative of the anorthite-poor phenocrysts.

Table 3.1. Whole-rock Major and Trace Element Results for Mutnovsky Lavas

sample	M1-04-08	M1-05-08	CM-19	CM-33	CM-105	M1-09-08	CM-48	CM-92a	CM-97a	CM-33a	M1-06-08	CM-4a	CM-5
center	M I	M I	M I	M I	M I	M I	M I	M I	M I	M I	M I	M I	M I
Map #	1	2	3	4	5	6	7	8	9	10	11	12	13
SiO_2	53.14	51.67	52.42	52.59	51.06	51.23	50.92	50.94	51.44	58.08	54.08	55.13	53.95
Al_2O_3	18.65	19.81	19.53	23.00	17.73	17.54	17.46	20.98	18.07	18.90	17.61	18.45	18.72
FeO*	10.81	9.89	9.93	7.54	10.42	11.83	11.96	9.15	10.01	8.20	10.80	7.62	9.18
MnO	0.20	0.19	0.18	0.21	0.21	0.24	0.23	0.21	0.16	0.19	0.23	0.16	0.16
MgO	3.43	3.18	3.46	3.24	5.71	4.76	4.89	3.73	7.29	2.39	3.50	4.76	4.00
CaO	8.37	10.03	8.91	8.73	9.80	9.22	9.54	10.24	8.78	6.03	8.22	8.37	8.61
Na_2O	3.29	3.42	3.35	2.88	2.92	3.21	3.12	2.76	2.45	3.70	3.50	3.61	3.17
K_2O	0.55	0.41	0.55	0.60	0.52	0.42	0.36	0.74	0.55	1.12	0.45	0.78	0.74
TiO_2	1.34	1.22	1.42	1.06	1.42	1.33	1.31	1.13	1.11	1.16	1.34	0.91	1.22
P_2O_5	0.22	0.18	0.24	0.15	0.21	0.22	0.21	0.12	0.13	0.22	0.27	0.20	0.25
Mg#	0.36	0.36	0.38	0.43	0.49	0.42	0.42	0.42	0.56	0.34	0.37	0.53	0.44
Rb	7.06	4.95	5.35	6.86	2.79	5.66	5.26	5.83	8.09	13.2	3.34	7.35	10.1
Sr	386	399	423	420	511	413	404	412	477	402	451	410	462
Y	27.8	31.9	32.8	27.2	29.1	29.2	28.1	27.5	25.4	35.4	46.1	34.8	38.9
Zr	67.2	63.0	62.2	52.1	57.0	60.3	57.0	49.6	63.8	74.4	84.4	81.7	70.3
Nb	1.33	1.07	1.05	1.20	1.11	1.20	1.13	0.85	1.36	1.70	1.95	1.62	1.47
Cs	0.49	0.41	0.23	0.34	0.26	0.44	0.41	0.35	0.49	0.68	0.23	0.37	0.78
Ba	179	154	164	164	174	164	149	151	229	274	282	277	242
La	4.44	4.30	4.42	5.39	4.63	4.77	4.38	4.01	5.63	7.36	6.46	6.89	6.55
Ce	12.3	12.8	13.1	13.4	13.9	13.2	12.5	11.4	15.1	18.8	17.8	19.4	18.7
Pr	2.17	2.33	2.39	2.43	2.51	2.34	2.23	2.07	2.47	3.12	3.05	3.34	3.24
Nd	11.8	13.1	13.5	12.7	13.6	12.6	12.2	11.4	12.5	16.1	16.4	17.1	17.0
Sm	3.67	4.12	4.27	3.70	4.13	3.85	3.76	3.56	3.55	4.71	5.12	4.95	5.07
Eu	1.20	1.35	1.44	1.21	1.36	1.25	1.22	1.18	1.20	1.52	1.89	1.53	1.65
Gd	4.38	5.05	5.01	4.22	4.95	4.67	4.40	4.24	4.19	5.41	6.72	5.73	6.24
Tb	0.72	0.83	0.85	0.70	0.82	0.75	0.73	0.70	0.71	0.90	1.20	0.98	1.05
Dy	4.65	5.25	5.44	4.46	5.22	4.74	4.67	4.52	4.51	5.78	7.86	6.32	6.75
Ho	0.96	1.09	1.13	0.92	1.07	0.98	0.97	0.94	0.93	1.20	1.66	1.30	1.41
Er	2.70	3.04	3.18	2.59	3.01	2.73	2.71	2.63	2.64	3.40	4.80	3.70	3.96
Tm	0.41	0.46	0.48	0.40	0.45	0.41	0.40	0.40	0.40	0.52	0.72	0.57	0.60
Yb	2.78	3.10	3.25	2.64	2.88	2.74	2.75	2.68	2.61	3.52	4.71	3.75	3.89
Lu	0.42	0.46	0.50	0.40	0.45	0.41	0.42	0.40	0.41	0.54	0.73	0.59	0.62
Hf	2.19	2.12	2.11	1.72	1.87	1.95	1.90	1.70	1.96	2.45	2.56	2.58	2.28
Ta	0.08	0.06	0.06	0.07	0.06	0.06	0.06	0.05	0.09	0.11	0.11	0.10	0.09
Pb	4.09	3.05	3.87	3.66	3.55	3.78	3.51	3.43	4.82	6.27	5.98	5.92	5.50
Th	0.42	0.28	0.28	0.43	0.28	0.30	0.30	0.32	0.52	0.74	0.47	0.64	0.53
U	0.18	0.14	0.15	0.18	0.12	0.14	0.14	0.17	0.24	0.33	0.24	0.27	0.25

Table 3.1. Whole-rock Major and Trace Element Results for Mutnovsky Lavas (continued)

sample	CM-24	M1-02-08	CM-47	CM-156	CM-169a	CM-187	CM-186	CM-142	CM-147	CM-154	CM-155	CM-113	M3-03-08
center	M I	M I	M I	M II	M II	M II	M II	M II	M II	M II	M II	M II	M III
Map #	14	15	16	17	18	19	20	21	22	23	24	25	26
SiO_2	60.73	61.04	65.52	49.55	52.52	52.29	54.58	54.51	60.98	63.90	58.37	68.51	51.66
Al_2O_3	18.28	17.13	16.25	18.98	18.16	19.03	17.44	17.68	16.63	16.28	16.03	14.84	18.22
FeO*	6.20	7.14	5.41	9.68	10.29	9.45	9.94	9.48	7.40	5.89	9.53	4.79	11.34
MnO	0.16	0.16	0.15	0.31	0.26	0.15	0.18	0.23	0.16	0.21	0.21	0.11	0.21
MgO	2.23	2.30	1.64	6.51	4.66	4.60	4.01	3.88	2.00	1.41	2.70	1.07	4.68
CaO	5.59	5.78	4.07	11.01	8.97	9.50	8.04	8.30	4.83	4.34	6.05	3.36	9.06
Na_2O	4.42	3.94	3.81	2.13	3.02	2.87	3.39	3.56	4.72	5.13	3.95	4.62	3.02
K_2O	1.04	1.29	2.01	0.49	0.55	0.68	0.80	0.73	1.54	1.50	1.32	2.13	0.45
TiO_2	1.03	0.95	0.92	1.19	1.40	1.23	1.38	1.34	1.28	1.02	1.48	0.48	1.16
P_2O_5	0.32	0.27	0.22	0.15	0.17	0.19	0.24	0.29	0.46	0.32	0.35	0.10	0.21
Mg#	0.39	0.36	0.35	0.55	0.45	0.46	0.42	0.42	0.32	0.30	0.34	0.28	0.42
Rb	14.6	40.4	37.8	4.29	5.93	6.05	9.04	8.30	18.1	21.4	15.1	21.1	4.36
Sr	374	392	317	476	456	500	478	474	407	350	411	200	477
Y	42.1	43.2	40.4	26.4	29.2	31.2	40.8	38.1	57.3	56.6	52.4	20.3	23.3
Zr	122	132	192	53.7	61.5	71.5	94.9	94.2	160	193	153	122	50.2
Nb	2.46	2.76	3.59	1.07	1.18	1.48	1.95	1.94	3.56	3.95	3.16	2.75	1.14
Cs	0.27	1.58	2.51	0.41	0.52	0.25	0.47	0.61	1.22	1.46	0.74	2.38	0.36
Ba	415	390	652	166	200	196	253	250	502	591	451	696	168
La	8.21	9.75	13.2	4.23	4.99	5.59	7.52	7.12	14.0	14.0	11.0	8.51	4.30
Ce	23.9	26.1	33.8	12.4	14.4	16.5	22.0	21.2	37.7	38.3	32.0	20.9	12.0
Pr	3.82	4.27	4.99	2.21	2.51	2.85	3.79	3.60	6.23	6.06	5.29	2.69	2.02
Nd	19.3	21.8	23.1	11.9	13.4	15.0	19.8	18.9	31.2	29.8	27.0	11.7	10.8
Sm	5.62	6.16	5.97	3.65	4.02	4.41	5.75	5.48	8.44	8.09	7.68	2.86	3.24
Eu	1.83	1.99	1.54	1.21	1.34	1.40	1.72	1.64	2.24	2.14	2.15	0.90	1.18
Gd	6.59	7.03	6.66	4.38	4.81	5.20	6.77	6.47	9.71	9.25	8.84	3.14	3.85
Tb	1.13	1.21	1.11	0.74	0.81	0.88	1.14	1.08	1.60	1.53	1.46	0.54	0.67
Dy	7.36	7.68	7.00	4.74	5.23	5.61	7.22	6.91	10.0	9.73	9.26	3.48	4.32
Ho	1.53	1.58	1.44	0.98	1.09	1.16	1.50	1.43	2.08	2.02	1.92	0.74	0.89
Er	4.42	4.63	4.12	2.79	3.08	3.29	4.25	4.05	5.89	5.81	5.45	2.19	2.52
Tm	0.69	0.69	0.64	0.42	0.46	0.49	0.64	0.61	0.89	0.89	0.82	0.35	0.38
Yb	4.59	4.61	4.18	2.70	3.02	3.22	4.17	3.99	5.76	5.84	5.41	2.46	2.46
Lu	0.73	0.71	0.67	0.43	0.48	0.51	0.67	0.63	0.93	0.94	0.86	0.42	0.37
Hf	3.77	3.94	5.32	1.76	2.04	2.30	3.01	3.00	4.82	5.46	4.56	3.69	1.59
Ta	0.14	0.17	0.26	0.06	0.07	0.08	0.11	0.11	0.20	0.22	0.17	0.27	0.06
Pb	7.47	8.85	12.84	3.76	4.83	4.63	5.28	5.88	11.14	12.18	10.46	11.10	4.05
Th	1.00	1.40	3.04	0.25	0.37	0.38	0.51	0.51	1.13	1.15	0.95	3.53	0.30
U	0.43	0.63	1.21	0.14	0.19	0.18	0.24	0.24	0.54	0.54	0.44	1.17	0.14

Table 3.1. Whole-rock Major and Trace Element Results for Mutnovsky Lavas (continued)

sample	M3-04-08	M3-05-08	M3-07-08	M3-08-08	CM-29	CM-193	CM-201b	CM-210	CM-211	KR1-2	CM-9a	M3-09-08
center	M III	M III	M III	M III	M III	M III	M III	M III	M III	M III	M III	M III
Map #	27	28	29	30	31	32	33	34	35	36	37	38
SiO_2	51.68	51.34	50.20	49.49	50.43	53.64	52.25	50.22	49.39	56.95	53.65	59.29
Al_2O_3	18.44	18.43	19.66	22.95	18.07	18.07	20.50	17.83	17.81	16.49	19.31	18.15
FeO*	11.03	11.24	10.24	7.23	10.07	9.20	8.01	9.16	9.69	8.90	7.95	6.60
MnO	0.20	0.21	0.18	0.13	0.15	0.18	0.25	0.11	0.18	0.16	0.14	0.13
MgO	4.51	4.70	4.23	4.46	5.81	4.93	4.51	8.24	8.50	4.27	5.47	2.18
CaO	9.29	9.30	10.69	12.58	11.04	8.87	10.64	10.96	10.74	7.84	9.33	7.29
Na_2O	3.17	3.08	2.95	2.19	2.65	2.94	2.06	2.07	2.28	2.82	2.53	3.68
K_2O	0.38	0.37	0.54	0.28	0.46	0.80	0.62	0.28	0.40	1.38	0.67	1.63
TiO_2	1.15	1.15	1.11	0.60	1.16	1.17	0.98	0.93	0.82	0.96	0.80	0.85
P_2O_5	0.15	0.17	0.20	0.09	0.15	0.19	0.18	0.22	0.19	0.23	0.15	0.21
Mg#	0.42	0.43	0.42	0.52	0.51	0.49	0.50	0.62	0.61	0.46	0.55	0.37
Rb	3.17	3.73	9.76	6.25	1.58	8.34	4.71	7.76	7.04	28.3	12.5	40.2
Sr	479	485	430	451	469	459	497	503	514	402	457	405
Y	22.0	15.2	30.8	20.3	25.0	36.9	23.0	23.6	23.6	30.1	24.9	35.2
Zr	47.3	49.0	75.6	57.3	53.0	88.0	58.6	72.5	70.5	142	79.2	189
Nb	1.06	1.14	1.78	1.09	1.02	1.99	1.32	2.02	1.93	3.08	1.54	3.76
Cs	0.15	0.27	0.56	0.50	0.12	0.44	0.32	0.43	0.36	1.75	0.80	2.51
Ba	165	168	209	174	164	302	198	232	223	406	262	540
La	3.92	2.71	5.90	4.07	4.19	9.81	5.32	6.87	6.84	10.3	5.76	13.24
Ce	12.1	8.0	16.1	11.1	12.1	24.4	14.3	17.5	17.5	25.5	15.6	32.6
Pr	1.96	1.29	2.73	1.81	2.05	3.91	2.38	2.79	2.76	3.80	2.47	4.77
Nd	10.5	6.9	14.2	9.35	10.9	19.3	12.3	13.7	13.6	17.8	12.3	22.1
Sm	3.20	2.16	4.19	2.80	3.36	5.33	3.54	3.75	3.71	4.65	3.46	5.52
Eu	1.18	0.81	1.46	1.02	1.15	1.63	1.29	1.27	1.27	1.26	1.11	1.45
Gd	3.76	2.57	5.02	3.35	4.10	6.14	4.05	4.17	4.13	5.07	4.03	5.93
Tb	0.66	0.45	0.87	0.59	0.68	1.04	0.69	0.70	0.69	0.87	0.69	1.01
Dy	4.24	2.90	5.60	3.80	4.43	6.55	4.30	4.38	4.31	5.48	4.40	6.35
Ho	0.87	0.60	1.17	0.79	0.91	1.35	0.87	0.89	0.88	1.12	0.92	1.30
Er	2.49	1.71	3.34	2.25	2.55	3.89	2.48	2.50	2.49	3.20	2.59	3.75
Tm	0.37	0.26	0.50	0.34	0.38	0.57	0.37	0.37	0.36	0.48	0.40	0.56
Yb	2.43	1.71	3.28	2.25	2.49	3.81	2.45	2.42	2.38	3.19	2.60	3.78
Lu	0.36	0.26	0.50	0.33	0.39	0.58	0.37	0.36	0.36	0.48	0.41	0.57
Hf	1.53	1.56	2.26	1.74	1.67	2.55	1.71	2.02	1.95	3.96	2.35	5.23
Ta	0.06	0.06	0.11	0.07	0.06	0.12	0.07	0.11	0.11	0.21	0.10	0.27
Pb	3.99	4.33	4.67	4.37	3.64	6.50	4.51	4.27	3.97	9.20	5.52	10.23
Th	0.26	0.26	0.66	0.51	0.33	0.66	0.27	0.53	0.51	2.05	0.83	3.00
U	0.10	0.11	0.27	0.22	0.16	0.30	0.15	0.23	0.22	0.90	0.37	1.32

Table 3.1. Whole-rock Major and Trace Element Results for Mutnovsky Lavas (continued)

sample	M3-01-08	CM-8a	M4-01-08	CM-196	CM-206	CM-68	CM-61a	CM-63a	CM-67	CM-198	KR-1	CM-62
center	M III	M III	M IV	M IV	M IV	M IV	M IV	M IV	M IV	M IV	M IV	M IV
Map #	39	40	41	42	43	44	45	46	47	48	49	50
SiO_2	64.09	69.60	53.19	49.60	51.97	50.95	50.19	50.30	48.97	50.14	54.94	54.24
Al_2O_3	16.00	14.65	19.37	19.22	18.31	20.94	19.97	19.15	20.25	18.12	16.93	17.44
FeO*	5.65	3.66	9.97	9.99	9.27	7.94	9.63	9.45	10.05	9.66	9.16	8.67
MnO	0.21	0.10	0.16	0.18	0.20	0.18	0.21	0.14	0.18	0.19	0.16	0.15
MgO	1.55	0.75	3.93	6.27	5.39	5.15	5.08	6.25	5.40	7.22	5.26	5.02
CaO	3.35	3.10	8.85	10.90	10.40	11.17	10.73	10.41	10.73	10.84	8.96	8.99
Na_2O	4.93	4.19	2.82	2.54	2.54	2.25	2.45	2.51	2.71	2.27	2.65	3.10
K_2O	2.71	3.19	0.55	0.29	0.61	0.55	0.42	0.55	0.55	0.49	0.85	1.20
TiO_2	1.27	0.63	0.99	0.85	1.13	0.78	1.06	1.01	1.00	0.93	0.91	1.00
P_2O_5	0.25	0.12	0.17	0.16	0.17	0.10	0.25	0.23	0.16	0.14	0.18	0.18
Mg#	0.33	0.27	0.41	0.53	0.51	0.54	0.48	0.54	0.49	0.57	0.51	0.51
Rb	64.6	53.6	9.67	2.82	5.75	2.98	4.76	6.53	4.91	3.83	17.0	16.8
Sr	271	177	471	474	520	437	501	498	472	461	427	432
Y	54.8	48.2	28.7	21.4	24.9	15.5	21.8	26.2	25.4	21.5	24.6	25.3
Zr	408	321	70.0	56.8	65.2	43.5	53.8	78.4	58.6	62.2	97.2	102
Nb	12.30	5.63	1.55	1.38	1.45	1.05	1.17	1.73	1.08	1.43	2.03	2.08
Cs	2.39	3.72	0.71	0.12	0.38	0.32	0.42	0.47	0.43	0.41	1.08	1.18
Ba	1069	900	222	187	204	125	161	223	169	169	282	307
La	31.5	16.6	6.07	5.08	5.64	3.14	4.08	6.66	4.37	4.87	7.07	7.42
Ce	75.1	44.7	16.0	13.4	14.8	8.8	11.7	18.4	12.8	12.9	17.9	19.5
Pr	9.96	6.23	2.58	2.19	2.43	1.45	1.95	2.89	2.19	2.11	2.75	2.96
Nd	42.2	28.1	13.3	11.0	12.4	7.36	10.1	14.4	11.5	10.7	13.4	14.2
Sm	9.55	7.01	3.92	3.13	3.55	2.16	2.99	3.95	3.43	3.10	3.69	3.79
Eu	2.44	1.37	1.38	1.14	1.27	0.77	1.08	1.31	1.22	1.13	1.14	1.12
Gd	9.32	7.53	4.73	3.65	4.18	2.58	3.60	4.44	4.18	3.64	4.15	4.31
Tb	1.57	1.29	0.81	0.62	0.71	0.44	0.61	0.76	0.72	0.63	0.71	0.71
Dy	9.73	8.30	5.21	3.95	4.51	2.84	3.96	4.74	4.62	3.96	4.49	4.52
Ho	2.00	1.73	1.08	0.81	0.92	0.58	0.82	0.97	0.96	0.81	0.92	0.92
Er	5.79	5.04	3.07	2.30	2.64	1.66	2.31	2.71	2.71	2.31	2.64	2.61
Tm	0.90	0.79	0.46	0.34	0.39	0.25	0.34	0.41	0.41	0.34	0.39	0.39
Yb	6.08	5.32	3.04	2.24	2.57	1.63	2.26	2.68	2.67	2.24	2.57	2.58
Lu	0.94	0.84	0.46	0.34	0.39	0.26	0.36	0.41	0.42	0.34	0.39	0.41
Hf	9.61	8.93	2.08	1.64	1.89	1.31	1.65	2.23	1.85	1.76	2.73	2.91
Ta	0.75	0.41	0.09	0.07	0.08	0.06	0.06	0.10	0.06	0.08	0.14	0.14
Pb	17.93	18.15	5.16	3.17	5.20	2.99	3.87	4.93	4.24	3.77	6.17	6.91
Th	4.91	4.79	0.50	0.29	0.39	0.31	0.31	0.42	0.27	0.31	1.22	1.36
U	1.99	1.89	0.24	0.13	0.19	0.14	0.14	0.20	0.15	0.16	0.53	0.56

Table 3.2. Average compositions of pyroxene analyses

Sample	CM-33	CM-5	CM-47	CM-187	CM-186	CM-113	CM-29	CM-9a	CM-8a
Phase	opx	opx	opx	opx	opx	opx	opx	opx	opx
No. of analyses	9	2	17	10	6	21	1	5	34
SiO_2	51.58	52.67	51.59	52.63	52.84	52.24	53.46	51.14	50.88
TiO_2	0.33	0.35	0.30	0.32	0.44	0.25	0.29	0.22	0.24
Al_2O_3	0.71	0.87	0.83	0.59	1.14	1.28	0.85	0.52	0.77
FeO_T	21.34	21.25	22.87	24.76	22.29	19.65	20.93	25.26	28.25
MnO	0.73	0.79	0.87	0.83	0.80	1.01	0.53	1.13	1.07
MgO	19.94	19.83	21.01	18.61	18.73	23.33	21.47	18.98	16.55
CaO	4.30	5.24	2.37	4.03	4.95	1.51	4.19	1.61	1.69
Na_2O	0.39	0.09	0.04	0.08	0.14	0.03	0.08	0.03	0.08
Total	99.33	101.08	99.87	101.86	101.32	99.30	101.79	98.89	99.54
Cations per formula unit based on 6 oxygens									
Si	1.942	1.955	1.937	1.964	1.970	1.941	1.957	1.965	1.973
Ti	0.009	0.010	0.008	0.009	0.012	0.007	0.008	0.006	0.007
Al^{IV}	0.048	0.035	0.037	0.027	0.018	0.052	0.035	0.028	0.020
Al^{VI}	0.000	0.003	0.000	0.000	0.032	0.004	0.002	0.000	0.016
Fe^{3+}	0.093	0.038	0.076	0.034	0.000	0.050	0.039	0.035	0.010
Fe^{2+}	0.579	0.622	0.644	0.739	0.695	0.561	0.602	0.777	0.906
Mn	0.023	0.025	0.028	0.026	0.025	0.032	0.016	0.037	0.035
Mg	1.120	1.098	1.171	1.035	1.040	1.291	1.172	1.088	0.956
Ca	0.174	0.208	0.096	0.161	0.198	0.060	0.164	0.066	0.070
Na	0.028	0.006	0.003	0.006	0.010	0.002	0.005	0.002	0.006
Mg#	62.5	62.4	61.7	57.3	59.9	67.9	64.6	57.3	51.0
$\pm 1\sigma$ Mg#	2.6	2.9	5.8	1.2	1.6	2.5	—	0.3	2.1

Phase	cpx	cpx	cpx	cpx	cpx	cpx	cpx	cpx	cpx
No. of analyses	3	7	6	7	6	8	15	18	10
SiO_2	49.67	49.56	50.57	51.78	54.68	49.60	51.28	50.75	50.79
TiO_2	0.72	0.97	0.55	0.66	0.62	0.75	0.70	0.59	0.43
Al_2O_3	2.72	4.20	2.00	1.40	2.90	3.10	2.30	2.89	1.32
FeO_T	11.34	12.18	11.19	15.01	13.61	10.36	14.10	9.79	14.33
MnO	0.41	0.38	0.44	0.53	0.53	0.50	0.39	0.33	0.60
MgO	15.32	14.03	14.59	14.42	12.87	14.73	15.00	15.46	12.50
CaO	18.47	18.63	19.50	16.99	15.38	19.06	17.31	18.97	18.87
Na_2O	0.28	0.30	0.29	0.33	0.68	0.31	0.27	0.26	0.28
Total	98.93	100.25	99.13	101.12	101.27	98.41	101.33	99.04	99.12
Cations per formula unit based on 6 oxygens									
Si	1.867	1.849	1.904	1.931	2.038	1.873	1.898	1.898	1.943
Ti	0.020	0.027	0.016	0.018	0.017	0.021	0.020	0.017	0.012
Al^{IV}	0.113	0.123	0.081	0.051	0.000	0.105	0.082	0.085	0.045
Al^{VI}	0.008	0.061	0.008	0.011	0.126	0.033	0.018	0.042	0.015
Fe^{3+}	0.125	0.083	0.094	0.064	0.000	0.095	0.084	0.062	0.051
Fe^{2+}	0.231	0.297	0.259	0.404	0.424	0.233	0.353	0.244	0.408
Mn	0.013	0.012	0.014	0.017	0.017	0.016	0.012	0.011	0.019
Mg	0.858	0.780	0.818	0.801	0.715	0.829	0.827	0.862	0.713
Ca	0.744	0.745	0.786	0.679	0.614	0.772	0.686	0.760	0.774
Na	0.021	0.022	0.021	0.024	0.049	0.023	0.019	0.019	0.021
Mg#	70.6	67.4	69.9	63.1	62.8	71.7	65.4	73.8	60.9
$\pm 1\sigma$ Mg#	2.6	3.8	3.6	1.3	0.4	2.7	2.1	3.4	2.7
T(°C) $\pm 1\sigma$	1093 ± 19	1079 ± 42	1015 ± 18	1099 ± 16	1086 ± 44	997 ± 21	1131 ± 15	1006 ± 35	1032 ± 18

Table 3.3. Average compositions of Fe-Ti oxides

Sample	CM-47	CM-186	CM-29	CM-9a	CM-8a
Phase	ilmenite	ilmenite	ilmenite	ilmenite	ilmenite
No. of analyses	4	13	2	2	7
SiO_2	0.62	0.24	0.20	15.32	0.22
TiO_2	45.48	44.04	48.67	34.47	47.14
Al_2O_3	0.35	0.07	0.12	4.92	0.20
Fe_2O_3	17.56	15.23	11.43	18.23	12.64
V_2O_3	0.37	0.38	0.45	0.42	0.30
Cr_2O_3	0.01	0.02	0.01	0.01	0.01
FeO	30.03	35.93	36.94	22.18	36.68
MnO	0.73	0.73	0.56	0.34	0.80
MgO	1.70	0.89	2.49	1.45	1.93
CaO	4.15	0.21	0.19	1.70	0.04
Total	100.99	97.71	101.08	99.05	99.95
$X_{ilmenite}$	76.1	80.2	79.1	77.8	79.2
$\pm 1\sigma$ $X_{ilmenite}$	2.1	1.4	1.2	2.5	0.4
Phase	magnetite	magnetite	magnetite	magnetite	magnetite
No. of analyses	30	17	8	8	11
SiO_2	0.16	0.14	0.37	0.20	0.35
TiO_2	14.64	8.02	16.46	13.97	16.37
Al_2O_3	2.07	0.79	1.81	1.86	1.63
Fe_2O_3	37.91	50.36	33.86	41.22	35.96
V_2O_3	0.71	0.74	1.24	0.56	0.35
Cr_2O_3	0.04	0.03	0.07	0.05	0.02
FeO	41.75	36.59	44.38	41.78	44.62
MnO	0.57	0.42	0.57	0.54	0.66
MgO	1.48	0.24	1.05	1.73	1.12
CaO	0.12	0.18	0.16	0.07	0.10
Total	99.45	97.50	99.97	101.98	101.17
$X_{ulvospinel}$	41.1	23.5	46.0	38.2	45.3
$\pm 1\sigma$ $X_{ulvospinel}$	4.7	3.3	5.9	0.8	3.0
T(°C) $\pm 1\sigma$	882 ± 41	775 ± 36	898 ± 40	959 ± 25	924 ± 21
ΔNNO $\pm 1\sigma$	-0.3 ± 0.1	0.5 ± 0.2	-0.6 ± 0.1	0.1 ± 0.03	-0.3 ± 0.04

3.8 REFERENCES

Anderson AT, Friedman R, Otto J, et al (1982) The Fractional Crystallization of Plagioclase in the Hat Creek Basalt: Observations and Theory. J Geol 90:545–558.

Atherton MP, Petford N (1993) Generation of sodium-rich magmas from newly underplated basaltic crust. Nature 362:144–146.

Bachmann O, Bergantz GW (2008) Rhyolites and their source mushes across tectonic settings. J Petrol 49:2277–2285. doi: 10.1093/petrology/egn068

Beard JS, Lofgren GE (1989) Effect of water on the composition of partial melts of greenstone and amphibolite. Science 244:195–197. doi: 10.1126/science.244.4901.195

Beard JS, Lofgren GE (1991) Dehydration Melting and Water-Saturated Melting of Basaltic and Andesitic Greenstones and Amphibolites at 1, 3, and 6. 9 kb. J Petrol 32:365–401. doi: 10.1093/petrology/32.2.365

Borg LE, Clynne M a. (1998) The Petrogenesis of Felsic Calc-alkaline Magmas from the Southernmost Cascades, California: Origin by Partial Melting of Basaltic Lower Crust. J Petrol 39:1197–1222. doi: 10.1093/petroj/39.6.1197

Brophy JG (1991) Composition gaps, critical crystallinity, and fractional crystallization in orogenic (calc-alkaline) magmatic systems. Contrib to Mineral Petrol 109:173–182. doi: 10.1007/BF00306477

Carmichael IS (2002) The andesite aqueduct: perspectives on the evolution of intermediate magmatism in west-central (105–99°W) Mexico. Contrib to Mineral Petrol 143:641–663. doi: 10.1007/s00410-002-0370-9

Carr M (2007) Igpet 2007 forWindows XP or Vista. Terra Softa Inc.

Coleman DS, Glazner a F, Frost TP (1992) Evidence from the lamarck granodiorite for rapid late cretaceous crust formation in california. Science 258:1924–1926. doi: 10.1126/science.258.5090.1924

Couch S, Sparks RS, Carroll MR (2001) Mineral disequilibrium in lavas explained by convective self-mixing in open magma chambers. Nature 411:1037–1039. doi: 10.1038/35082540

Drake MJ (1976) Plagioclase-melt equilibria. Geochim Cosmochim Acta 40:457–465. doi: 10.1016/0016-7037(76)90011-9

Dufek J, Bachmann O (2010) Quantum magmatism: Magmatic compositional gaps generated by melt-crystal dynamics. Geology 38:687–690. doi: 10.1130/G30831.1

Ghiorso MS, Evans BW (2008) Thermodynamics of Rhombohedral Oxide Solid Solutions and a Revision of the FE-TI Two-Oxide Geothermometer and Oxygen-Barometer. Am J Sci 308:957–1039. doi: 10.2475/09.2008.01

Hidalgo PJ, Rooney TO (2010) Crystal fractionation processes at Baru volcano from the deep to shallow crust. Geochemistry, Geophys Geosystems. doi: 10.1029/2010GC003262

Kent AJR, Darr C, Koleszar AM, et al (2010) Preferential eruption of andesitic magmas through recharge filtering. Nat Geosci 3:631–636. doi: 10.1038/ngeo924

Lange R, Carmichael I (1996) The Aurora volcanic field, California-Nevada: oxygen fugacity constraints on the development of andesitic magma. Contrib to Mineral Petrol 125:167–185.

MacDonald R, Belkin HE, Fitton JG, et al (2008) The roles of fractional crystallization, magma mixing, crystal mush remobilization and volatile-melt interactions in the genesis of a young basalt-peralkaline rhyolite suite, the greater Olkaria volcanic complex, Kenya Rift valley. J Petrol 49:1515–1547. doi: 10.1093/petrology/egn036

Murphy M, Sparks R, Barclay J, et al (2000) Remobilization of andesite magma by intrusion of mafic magma at the Soufriere Hills Volcano, Montserrat, West Indies. J Petrol 41:21–42.

Nelson ST, Montana A (1992) Sieve-textured plagioclase in volcanic rocks produced by rapid decompression. Am Mineral 77:1242–1249.

Petford N, Atherton MP (1996) Na-rich partial melts from newly underplated basaltic crust: the Cordillera Blanca Batholith, Peru. J Petrol 37:1491–1521. doi: 10.1093/petrology/37.6.1491

Petford N, Gallagher K (2001) Partial melting of mafic (amphibolitic) lower crust by periodic influx of basaltic magma. Earth Planet Sci Lett 193:483–499.

Ponomareva V, Churikova T, Melekestsev I, et al (2007) Late Pleistocene-Holocene Volcanism on the Kamchatka Peninsula, Northwest Pacific Region. Geophys Monogr Geophys Union 172:165.

Putirka KD (2008) Thermometers and Barometers for Volcanic Systems. Rev Mineral Geochemistry 69:61–120. doi: 10.2138/rmg.2008.69.3

Rapp RP, Watson EB (1995) Dehydration Melting of Metabasalt at 8-32 kbar: Implications for Continental Growth and Crust-Mantle Recycling. J Petrol 36:891–931. doi: 10.1093/petrology/36.4.891

Rapp RP, Watson EB, Miller CF (1991) Partial melting of amphibolite/eclogite and the origin of Archean trondhjemites and tonalites. Precambrian Res 51:1–25. doi: 10.1016/0301-9268(91)90092-O

Reubi O, Blundy J (2009) A dearth of intermediate melts at subduction zone volcanoes and the petrogenesis of arc andesites. Nature 461:1269–73. doi: 10.1038/nature08510

Rushmer T (1991) Partial melting of two amphibolites: contrasting experimental results under fluid-absent conditions. Contrib to Mineral Petrol 107:41–59. doi: 10.1007/BF00311184

Selyangin O (1993) Mutnovsky Volcano, Kamchatka: New Evidence on Structure, Evolution, and Future Activity. Volcanol Seismol 15:17–38.

Simon A, Yogodzinski GM, Robertson K, et al (2014) Evolution and genesis of volcanic rocks from Mutnovsky Volcano, Kamchatka. J Volcanol Geotherm Res 286:116–137. doi: 10.1016/j.jvolgeores.2014.09.003

Stormer JC, Nicholls J (1978) XLFRAC: a program for the interactive testing of magmatic differentiation models. Comput Geosci 4:143–159. doi: 10.1016/0098-3004(78)90083-3

Straub SM, LaGatta AB, Martin-Del Pozzo AL, Langmuir CH (2008) Evidence from high-Ni olivines for a hybridized peridotite/pyroxenite source for orogenic andesites from the central Mexican Volcanic Belt. Geochemistry, Geophys Geosystems. doi: 10.1029/2007GC001583

Tepper JH, Nelson BK, Bergantz GW, Irving AJ (1993) Petrology of the Chilliwack batholith, North Cascades, Washington: generation of calc-alkaline granitoids by melting of mafic lower crust with variable water fugacity. Contrib to Mineral Petrol 113:333–351. doi: 10.1007/BF00286926

Volynets ON (1994) Geochemical Types, Petrology, and Genesis of Late Cenozoic Volcanic Rocks from the Kurile-Kamchatka Island-Arc System. Int Geol Rev 36:373–405. doi: 10.1080/00206819409465467

Waters LE, Andrews BJ, Lange R a. (2015) Rapid Crystallization of Plagioclase Phenocrysts in Silicic Melts during Fluid-saturated Ascent: Phase Equilibrium and Decompression Experiments. J Petrol 56:981–1006. doi: 10.1093/petrology/egv025

Waters LE, Lange RA (2013) Crystal-poor, multiply saturated rhyolites (obsidians) from the Cascade and Mexican arcs: evidence of degassing-induced crystallization of phenocrysts. Contrib to Mineral Petrol 166:731–754. doi: 10.1007/s00410-013-0919-9

CHAPTER IV

A MODEL TO INVESTIGATE THE PLAUSIBILITY OF THE HYBRIDIZATION OF THERMALLY AND COMPOSITIONALLY DISTINCT MAGMAS

4.1. ABSTRACT

To assess the hypothesis that basaltic and dacitic magmas mixed to produce the basaltic andesite, we develop a quantitative model that fully describes the evolving viscosity of the basaltic and dacitic end-member magmas (melt + crystals, including water content) and quantify that there is a narrow viscosity-defined magma mixing window over a narrow range of temperatures (<30°C) where basaltic and dacitic magmas reach thermal equilibrium and mix to produce basaltic andesite. To test the applicability of the model to other magmatic systems, we used published mafic and felsic end-member magma estimates from Mt. Hood, Oregon, to demonstrate that the proposed basaltic and rhyolitic magma end-members for that system do enter a viscosity-defined magma mixing window where they can mix to produce andesite, as proposed in several published studies. Also consistent with published work, the efficiency of mixing is maximized with larger proportions of mafic magma, which is well documented as the primary source of energy for the mixing process. Our results demonstrate quantitatively that the physical mixing of mafic and felsic magmas from initially disparate thermal and viscosity conditions is a plausible mechanism to produce intermediate magmas. The methodology by which proposed mixing ratios can be tested to determine the physical plausibility for magma

mixing is globally applicable and can be applied in cases where mafic and felsic endmember compositions are known or can be estimated.

4.2. INTRODUCTION

Mixing of compositionally disparate magmas is a seemingly ubiquitous process in the plumbing systems of stratovolcanoes (Anderson 1976) The seminal work of Sparks and Marshall (1986) provided a conceptual framework that considers the physicochemical plausibility for compositionally disparate magmas (i.e., low-Si mafic and high-Si felsic) with different initial temperatures and viscosities to hybridize. Sparks and Marshall (1986) suggested that mixing requires magmas of similar temperatures and viscosities, and that the hybridization potential for magmas with very different initial (pre-mixing) viscosities is maximized if the proportion of mafic magma is volumetrically dominant, regardless of the composition of the felsic endmember. However, despite this well accepted conceptual framework, magma mixing as a petrological process for driving compositional diversity in arc environments remains controversial.

Recent studies by Laumonier et al. (2014a,b) have experimentally investigated the effect viscosity differences in magmas have on their ability to mix. Their findings show that magmas with a viscosity contrast, $\Delta\log\eta$ ($\log(\eta_{basalt}/\eta_{dacite})$), greater than 0.5 do not efficiently mix. This is in contrast to melt inclusion, phenocryst, and field observations of the mixing of mafic and felsic magmas with $\Delta\log\eta > 1$. However, the experimental studies are limited to the investigation of the mixing of compositionally distinct magmas at the same temperature, leaving an investigation of the mixing of two compositionally and thermally distinct magmas unaddressed.

In this study, we investigate the plausibility of physicochemical mixing of mafic and felsic magmas by focusing on lavas from the active, arc-front Mutnovsky volcano, located in

Kamchatka, Russia. By using thermodynamic models for the evolution of magma (melt + crystals, including water content) viscosities we quantitatively assess the hypothesis that mafic and felsic magmas physically mix to produce intermediate compositions. This work builds on the concepts described in Sparks and Marshall (1986) by applying a rigorous thermodynamic treatment to natural magma compositions, and linking the model to phenocryst assemblages in the lavas. We also use published compositions for Mt. Hood to demonstrate the applicability of the technique to other arc volcanic systems.

4.3. BACKGROUND GEOLOGY

Mutnovsky volcano is located ~75 km southwest of Petropavlovsk-Kamchatsky (Figure 4.1). Briefly summarized here from Selyangin (1993) and Simon et al. (2014), Mutnovsky consists of four superimposed eruptive centers, Mutnovsky I-IV. Mutnovsky I erupted basaltic to dacitic lavas from ~80-60 ka. Mutnovsky II formed ~3km southeast of the Mutnovsky I crater and erupted basaltic to dacitic lavas from ~40-30 ka. Mutnovsky III formed between the centers of Mutnovsky I and II and erupted basaltic to dacitic lavas. The active Mutnovsky IV has erupted only basalt and basaltic andesite. Across all eruptive centers, basalt and basaltic andesite are dominant, with ~12% of the total erupted volume (~91 km^3) comprised of andesite and dacite.

4.4. MELTS MODELING

The starting compositions used in this study are fifty samples from Mutnovsky volcano, previously characterized for their whole-rock compositions (Simon et al. 2014). A subset of these samples can be found in Table 4.1. MELTS modeling (Ghiorso and Sack 1995) was done by using the alphaMELTS software (Smith and Asimow 2005) and Rhyolite-MELTS (Gualda et al 2012). Whole-rock compositions were used as initial liquid compositions and were cooled in 1°C increments from 1200°C to 900°C for Mutnovsky basalts and basaltic andesites, 1200 to 800

for Mutnovsky dacites, 1200°C to 900°C for the proposed Mt. Hood mafic endmember (Kent et al 2010), and 1200°C to 700°C for the proposed Mt. Hood felsic endmember (Kent et al 2010), recording residual liquid composition, mineral phases crystallizing, and mineral compositions for each step. Oxygen fugacity was fixed at the nickel-nickel oxide reference buffer for the Mutnovsky samples, consistent with the fO_2 calculated for the rocks from the Fe-Ti oxide geothermobarometer of Ghiorso and Evans (2008). Oxygen fugacity for the Mt. Hood samples was set at the quartz-fayalite-magnetite buffer, following the Mt. Hood MELTS modeling of the same composition described in Cooper and Kent (2014). The pressure used for the Mutnovsky samples was 400 MPa, consistent with existing geobarometry and magma depth estimates (Robertson 2011; Robertson et al 2013; Simon et al 2014). The pressure used for Mt. Hood modeling was 200 MPa following Cooper and Kent (2014). The H_2O concentrations used for the Mutnovsky samples were determined for each sample by using the plagioclase hygrometer of Lange et al. (2009) and the average plagioclase composition of each sample. Due to the bimodal distribution of plagioclase in the basaltic andesites (described below) the calculated H_2O concentrations of the basaltic andesites are likely less robust; however, we emphasize that the calculated basaltic andesite viscosities do not play a role in the results and interpretations of this manuscript. The H_2O concentration used for Mt. Hood was 3.8 wt% following Kent et al. (2010) and Cooper and Kent (2014).

4.5. RESULTS

The program MELTS was used to calculate liquidus temperatures for whole-rock compositions of Mutnovsky basaltic and dacitic lavas, and these liquidus compositions were then were cooled in 1°C increments, recording residual liquid compositions, mineral phases crystallizing, and mineral compositions for each temperature increment. For the modeled basalts

and dacites the plagioclase compositions show less variability but are generally consistent with the observed An content. The modeled basaltic andesites only crystallize one population of plagioclase compositions and do not recreate the bimodal distribution observed in the natural samples. The viscosity of the melt at each temperature increment was calculated by using the viscosity model of Hui and Zhang (2007). Reported here are the results of modeling the Mutnovsky I-III samples examined in Chapter III. The effect of crystals on magma viscosity was calculated by using the Einstein-Roscoe equation (Roscoe 1952) using a packing-fraction of 0.6 (Marsh 1981) and the crystal fraction calculated by MELTS for each temperature increment. As temperature decreases from 1200 to 900°C, the viscosity of the residual melts, reported as log η, increases from ~1 to 4.2 for the basalt and basaltic andesite, and from ~2 to 4.5 for dacite (Figure 4.2). The calculated melt viscosity of the basalts and basaltic andesites is never greater than the calculated viscosity of the dacitic melt. However, the calculated magma (i.e., melt + crystals) viscosities exhibit a crossover at ~1125°C, where the viscosity of the basaltic and basaltic andesite magmas exceeds the viscosity of the dacitic magmas (Figure 4.2). This is a critical point as it is the viscosity of the magma, and not only the melt phase, that determines whether or not mixing may occur.

4.6. ASSESSING THE PLAUSIBILITY OF PHYSICAL MIXING OF BASALT AND DACITE

Sparks and Marshall (1986) described the ability of compositionally and thermally disparate magmas to mix in terms of the rate of heat transfer relative to the rate of mass transfer via chemical diffusion. They emphasized that heat transfer is significantly faster than chemical diffusion, such that two magmas will come to thermal equilibrium rapidly and yet still be in a state of chemical disequilibrium. The ability for the two magmas to chemically homogenize (i.e.,

mix) is dictated by the evolution of their physical properties after the attainment of thermal equilibrium. Since their pioneering study, experimental investigations have demonstrated that strong differences in magma viscosity are a physical barrier to mixing. Magmas with a $\Delta \log \eta$ ($\log(\eta_{basalt}/\eta_{dacite})$) < 0.5 may effectively mix, magmas with $\Delta \log \eta > 0.5$ will not mix, and magmas with $\log \eta > 7.5$ do not effectively mix (Scaillet et al., 2013; Laumonier et al., 2014a,b).

The development of the MELTS computational thermodynamics software allows for improved constraints on the work of Sparks and Marshall (1986). In their study, crystallinity was estimated by using the Zr concentrations of a suite of samples to estimate the degree of crystallization required to move from one composition to another, magma viscosity was calculated by using the method of Shaw (1972) and the estimated crystallinity, and the heat capacity of the magmas were assumed. The method used to approximate the crystallinity is not applicable to places where mixing has been proposed and mafic endmember compositions have not been observed, preventing a test of mixing. Given constraints on pressures and water contents, the MELTS program quantitatively determines crystallinity, melt composition, and heat capacity of melt and crystals for a starting composition from any initial to final temperature. We have compared MELTS output of the same starting composition used in Sparks and Marshall (1986) with the estimated crystallinity data presented in Sparks and Marshall (1986) in Figure 4.3. The MELTS calculated crystal fraction is consistent with Sparks and Marshall (1986) for higher MgO contents, but deviates at lower MgO contents. This increased crystallinity with decreasing MgO is apparent at greater than 60% crystals, suggesting that the MELTS results are similar to the Sparks and Marshall (1986) as applied to an investigation of magma mixing, as crystallinity >60% is thought to behave as a partially molten solid, effectively preventing mixing (Van der Molen and Paterson 1979; Shaw 1980; Marsh 1981; Marsh 1984). With this

comparison and with the wealth of data output by MELTS, we suggest that the data generated by MELTS allow for a more robust assessment of the physical plausibility of magma mixing.

To evaluate the plausibility that Mutnovsky basalt and dacite physically mixed to produce the basaltic andesites, we calculated viscosities for Mutnovsky I-III basaltic and dacitic magmas (melt + crystals) and assessed whether the viscosities of the basaltic and dacitic magmas satisfied the $\Delta\log \eta$ ($\log(\eta_{basalt}/\eta_{dacite})$) < 0.5 criteria for mixing during their evolution. The results are shown in Figure 4.2. The results indicate that the viscosities of Mutnovsky basalt and dacite overlap at temperatures on the order of 1100 – 1140 °C, which along with the criterion that $\Delta\log \eta$ ($\log(\eta_{basalt}/\eta_{dacite})$) < 0.5, defines the viscosity-temperature window where physical mixing is plausible. The ability to mix magmas of different initial viscosities and temperatures was assessed by using the heat capacity of the magmas, which was calculated by MELTS for every temperature increment. The thermal response of each magma to mixing was calculated ideally, using the equation $X_{dacite}\ \Delta T_{dacite}\ C_{P\ dacite} = X_{basalt}\ \Delta T_{basalt}\ C_{P\ basalt}$, where X is the proportion of magma, ΔT is the temperature change of the magma when thermal equilibrium has been reached, and C_P is the integrated heat capacity of the magma from $T_{initial}$ to T_{final} at constant pressure. Using this equation, the model-based mixing ratio of 9:1 basalt:dacite reported by Simon et al. (2014), and the magma viscosity mixing window for each set of magmas mixing, we calculated mixing scenarios for basalt and dacite erupted from Mutnovsky I, II and III. The temperature-viscosity model results are shown in Figures 4.4a, b and c, respectively. For Mutnovsky I, the results indicate that the interaction of a 1009°C plagioclase-bearing dacitic magma (B′ in Figure 4.4a) physically interacting with a 1112°C basaltic magma (B in Figure 4.4a) results in the two magmas reaching thermal equilibrium at 1102°C (Figure 4.4a, Table 4.2). For Mutnovsky II, the results indicate that the interaction of a 1025°C plagioclase-bearing dacitic magma (B′ in Figure

4.4b) physically interacting with a 1123°C basaltic magma (B in Figure 4.4b) results in the two magmas reaching thermal equilibrium at 1113°C (Figure 4.4b, Table 4.2). For Mutnovsky III, the model results indicate that the interaction of a 1044°C plagioclase-bearing dacitic magma (B′ in Figure 4.4c) physically interacting with a 1140°C basaltic magma (B in Figure 4.4c) results in the two magmas reaching thermal equilibrium at 1130°C (Figure 4.4c, Table 4.2). These temperatures are all consistent with the two pyroxene temperatures of the same lavas, suggesting that they can efficiently mix as they approach thermal equilibrium.

As mentioned previously, diffusion of heat is orders of magnitude faster than chemical diffusion. Thus, for the conditions where basalt dominates the mixing assemblage (basalt:dacite = 9:1), heat transfer from basalt with an initial temperature of ~1140°C to dacite with an initial temperature of ~1040°C results in increasing the temperature of the dacite on the order of 100°C while the basalt cools by only ~10°C. Thus, both the basaltic and dacitic magmas coexist within the viscosity-defined thermal mixing window. In turn, while thermal equilibration is approached, progressive crystal-melt disequilibrium results in progressive resorption of plagioclase phenocrysts from the dacite endmember. The preservation of the strongly bimodal plagioclase populations in the basaltic andesites at Mutnovsky indicates that eruption occurred prior to complete chemical equilibration of the two mixed magmas. These model results indicate that dacitic magmas over a large range of temperatures can thermally equilibrate with basaltic magmas and end up in the viscosity-defined mixing window, allowing for the physical hybridization of initially compositionally and thermally distinct dacitic and basaltic magmas. Physical mixing and hybridization of dacitic and basaltic magmas, where the basaltic magma is dominant volumetrically, would result in resorption of An-poor plagioclase from the dacitic

magma, consistent with the textures observed in Mutnovsky basaltic andesites (cf. Tsuchiyama, 1985).

To investigate the broader applicability of this model, we applied it to the mixing of basaltic and rhyolitic magmas proposed by Kent et al. (2010) as mixing endmembers for intermediate magmas erupted at Mount Hood, Oregon (mafic and felsic compositions provided in Table 4.1). The authors invoke the mixing of ~75-40% basalt with ~25-60% rhyolite to explain the compositional variability at Mt. Hood by mixing alone, and suggest the mafic and felsic endmember magmas were 1100°C and 800°C, respectively. Figure 4.5 illustrates that our model predicts that mixing is physically plausible at a ratio of 70:30 basalt:rhyolite, though the model temperature of the felsic endmember must be 850-900°C (A′ in Figure 4.5) in order to efficiently mix with the 1100°C mafic endmember (A in Figure 4.5). Mixing becomes less likely as the percent mafic component decreases, consistent with previous studies (cf. Sparks and Marshall, 1986). This model can also be used to estimate the ratio of magmas mixed if the endmember temperatures are known or fixed. If we use the proposed temperatures of 1100°C and 800°C for basalt and rhyolite, respectively, from Kent et al. (2010) we calculate effective mixing of 100-75% basalt and 0-25% rhyolite. This suggests that some of the higher silica andesites may be the product of fractional crystallization after the mixing of 75:25 basalt:rhyolite rather than generation by mixing alone.

The model results for physical mixing of Mutnovsky mafic and felsic magmas are consistent with thermal models for the development of silicic magmas by successive emplacement of basaltic sills (Annen et al., 2006a,b, 2008; Annen, 2011) and with the recent experimental data of Laumonier et al. (2014b). Repeated emplacement of basaltic sills provides thermal energy sufficient to partially melt underplated basaltic rock to generate dacitic melts that

can subsequently cool and crystallize over relatively short timescales. Subsequent injections of basaltic magma can then intrude through or into these dacitic lenses, allowing for the hybridization of the two compositionally distinct magmas, provided that they mix in appropriate volumes at appropriate temperatures. The remobilization of a crystal-rich dacitic magma is consistent with the work of Cooper and Kent (2014), who demonstrated that most of the phenocrysts found in Mt. Hood lavas spent a majority of their existence at temperatures below their MELTS-calculated lock-up temperature. These crystals were essentially un-eruptible until injection of new, hot magma remobilized and erupted the previously locked crystal-mush. This suggests that dacitic lenses generated by partial melting caused by repeated basaltic underplating could cool below lock-up temperature, and be remobilized by subsequent injection(s) of basaltic magmas. Dacitic and basaltic magmas can in turn mix physically provided that the mixing ratio allows the magmas to enter the viscosity mixing window. The thermal-viscosity model presented here indicates that this process was plausibly responsible for formation of basaltic andesites erupted at Mutnovsky, and intermediate composition magmas erupted at stratovolcanoes worldwide.

4.7. CONCLUSIONS

In light of the significant advances in computational thermodynamics over the last decade, as well as an ever increasing number of experimental studies, the seminal work of Sparks and Marshall (1986) deserved to be revisited. A thermal and viscosity model integrating the thermodynamic data generated through the MELTS model demonstrates the physical plausibility of the mixing of basaltic and dacitic magmas to produce basaltic andesite erupted at Mutnovsky. The use of the MELTS model eliminates many of the uncertainties in calculating viscosity, crystallinity, and thermodynamic parameters for phases present at a given P-T.

Investigating another location of proposed mixing (Kent et al. 2010), this model supports the mixing origin for intermediate magmas at Mt. Hood, Oregon. The viscosity and thermal modeling presented here provides a straightforward way to quantify the plausibility of physical magma mixing and assess its role to produce intermediate composition lavas at arc volcanoes worldwide.

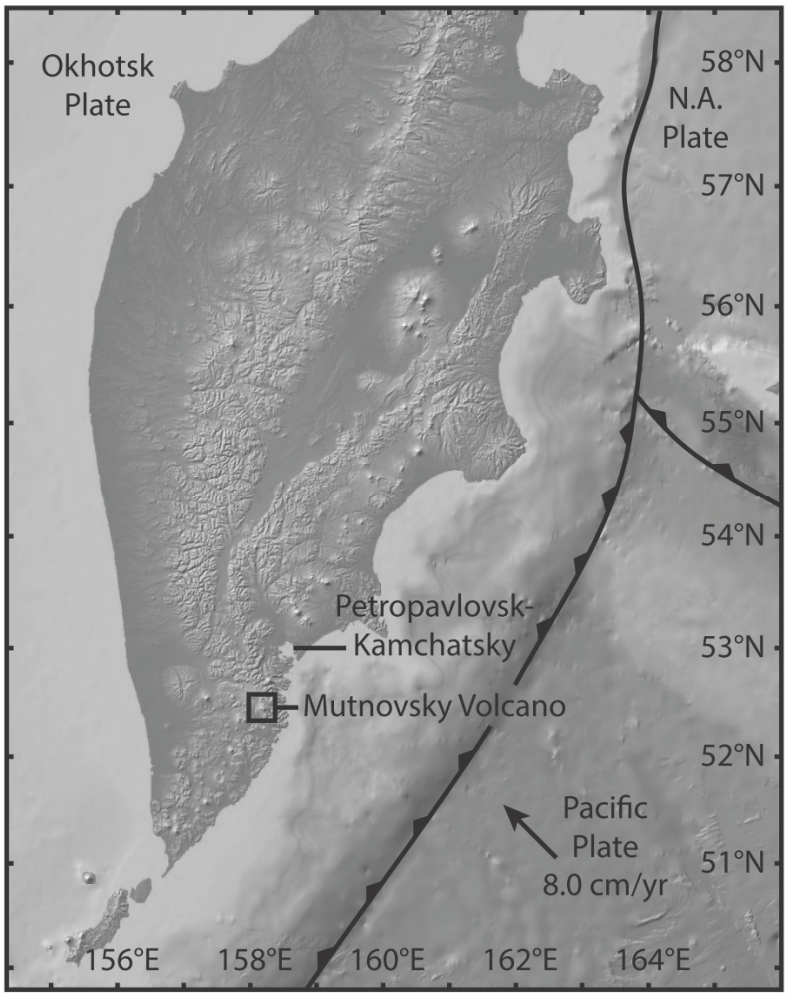

Figure 4.1 A map of the Kamchatka Peninsula showing the location of Mutnovsky Volcano. Map from GeoMapApp (www.geomapapp.org)

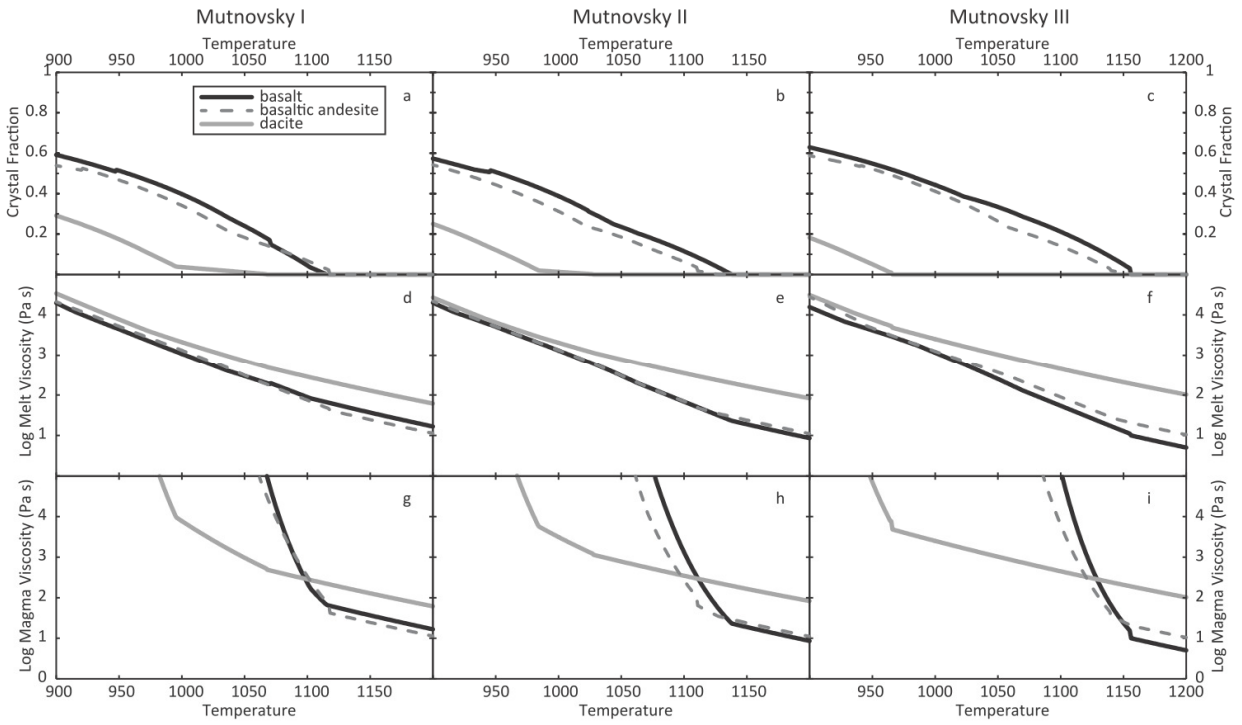

Figure 4.2 Crystal fraction (a-c), melt viscosity (d-f), and magma viscosity (g-i) calculated by using MELTS and the viscosity model of Hui and Zhang (2007) for basalt, basaltic andesite, and dacite from Mutnovsky I-III. Calculated melt viscosities show no crossover between basalt and dacite. The addition of crystals drastically changes the viscosities such that basaltic and dacitic magma cross over at 1100-1130°C

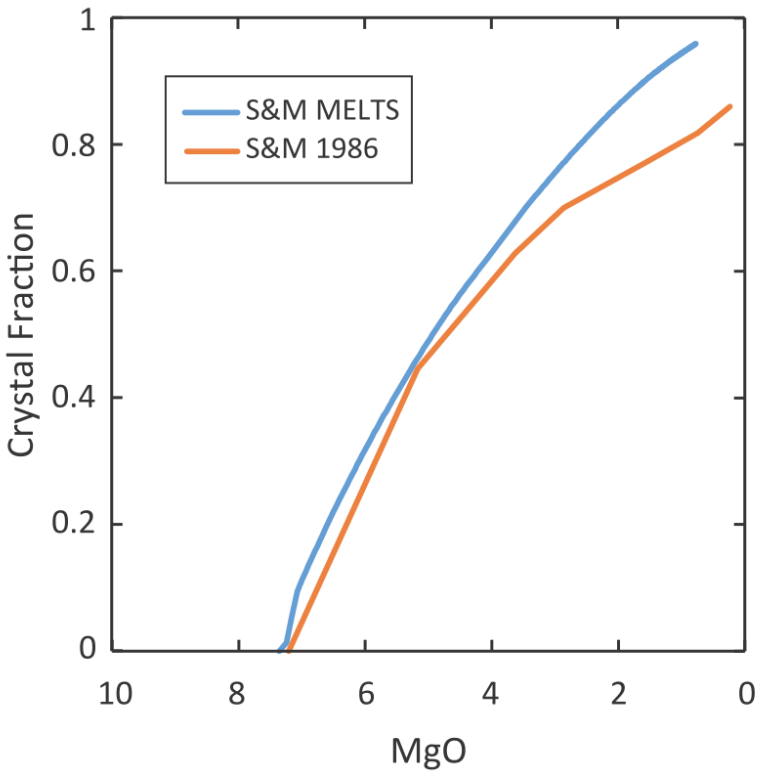

Figure 4.3 Comparison of MELTS produced crystal fraction vs. MgO of St. Kilda mafic endmember, SK27, with Zr-estimated crystal fraction vs. MgO calculated by Sparks and Marshall (1986). The crystal fraction estimated by MELTS is similar to the data reported in Sparks and Marshall (1986), but reports higher crystal fractions at lower MgO contents. Given that a magma with crystal fraction greater than 0.6 becomes effectively solid (Marsh 1981), we suggest that the MELTS model effectively reproduces the estimation of Sparks and Marshall (1986)

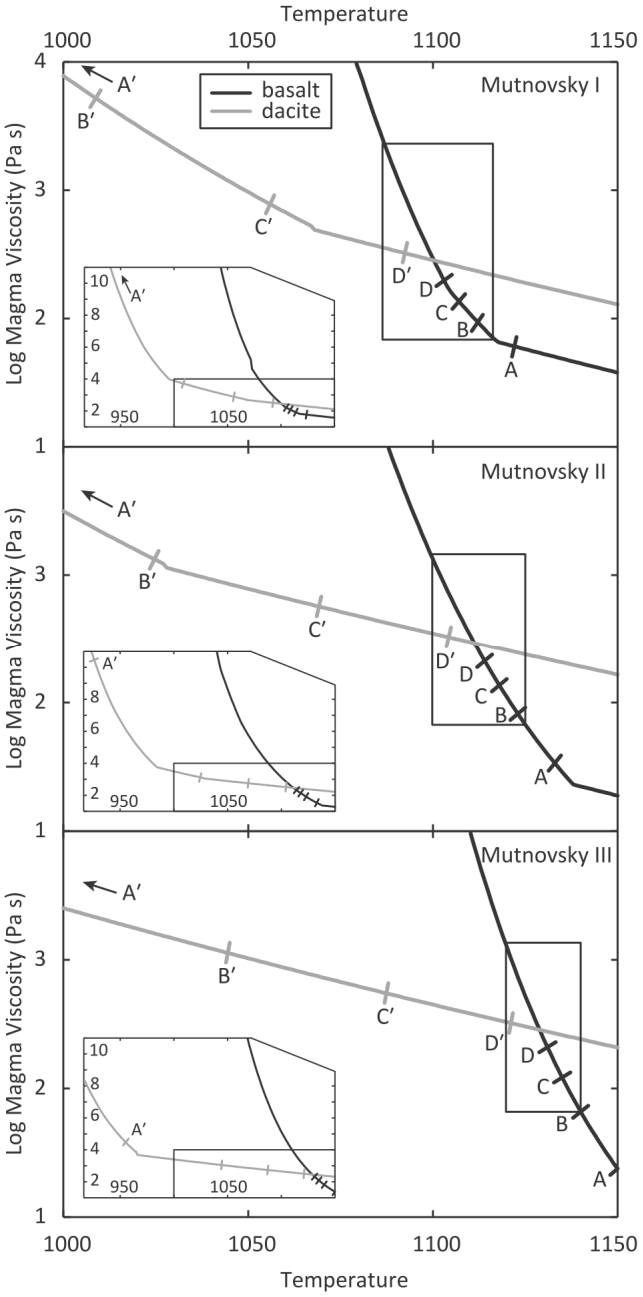

Figure 4.4 Log magma viscosity vs temperature for Mutnovsky I-III and Mt. Hood. The Mutnovsky III inset shows a larger range of temperature and viscosity, and the box in the inset represents the portion displayed in the main figure. The vertical rectangular box on the right side of each figure illustrates the window of temperature and viscosity within which magma viscosities are <0.5 log Pa s of each other and can physically mix after attaining thermal equilibrium. Tick marks labeled A-A′, B-B′, etc. represent a basalt (A, B, C, D) and dacite or rhyolite (A′, B′, C′, D′) that will reach thermal equilibrium at the viscosity crossover (Table 4.2). As described in the text, these plots illustrate that a Mutnovsky basaltic magma at B mingling with a Mutnovsky dacitic magma at B′, for a ratio of 9:1 basalt:dacite, results in thermal equilibrium at within the viscosity-defined mixing window, and allows for efficient mixing

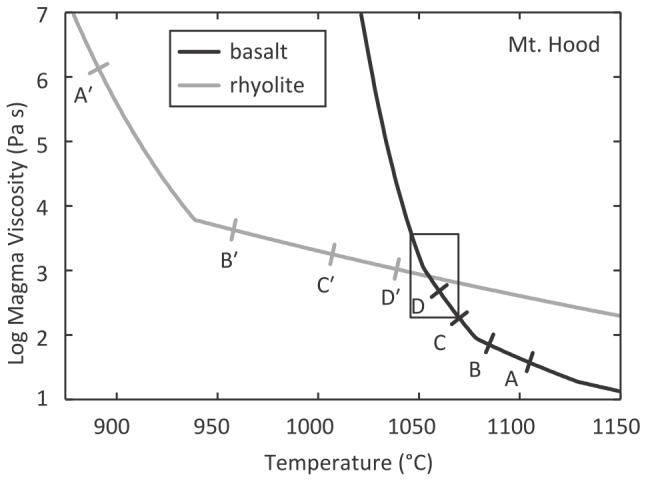

Figure 4.5 Log magma viscosity vs. temperature for proposed Mt. Hood mafic and felsic end-members from Kent et al. (2010), similar to Figure 4.4. These results indicate that a basaltic magma at 1105°C (A) mingling with a rhyoltic magma at 891°C (A′), at a ratio of 7:3 basalt:rhyolite, results in efficient mixing at ~1055°C

Table 4.1 Samples used as MELTS starting compositions

Sample	SiO_2 (wt%)	TiO_2 (wt%)	Al_2O_3 (wt%)	FeO_T (wt%)	MnO (wt%)	MgO (wt%)	CaO (wt%)	Na_2O (wt%)	K_2O (wt%)	P_2O_5 (wt%)	Total (wt%)
Mutnovksy I											
CM-33	51.56	1.04	22.55	7.39	0.21	3.18	8.56	2.82	0.59	0.15	98.05
CM-5	52.38	1.18	18.18	8.91	0.16	3.88	8.36	3.08	0.72	0.24	97.09
CM-47	64.68	0.91	16.04	5.34	0.15	1.62	4.02	3.76	1.98	0.22	98.72
Mutnovsky II											
CM-187	50.96	1.20	18.54	9.21	0.15	4.48	9.26	2.80	0.66	0.19	97.45
CM-186	53.36	1.35	17.05	9.72	0.18	3.92	7.86	3.31	0.78	0.23	97.76
CM-113	67.53	0.47	14.63	4.72	0.11	1.05	3.31	4.55	2.10	0.10	98.57
Mutnovsky III											
CM-29	49.20	1.13	17.63	9.83	0.15	5.67	10.77	2.59	0.45	0.15	97.57
CM-9a	52.80	0.79	19.00	7.82	0.14	5.38	9.18	2.49	0.66	0.15	98.41
CM-8a	69.40	0.63	14.61	3.65	0.10	0.75	3.09	4.18	3.18	0.12	99.71
Mt. Hood											
Mafic	50.7	1.6	20.3	9.3	0.0	5.8	8.2	4.1	0.1	0.0	100.0
Felsic	70.9	0.3	14.6	1.6	0.0	0.1	3.6	4.4	2.8	0.0	98.3

Note: Mafic and Felsic endmembers for Mt. Hood from Kent et al. (2010)

Table 4.2 Calculated magma temperatures and viscosities resulting in efficient mixing

Mutnovsky I	Basalt		Dacite	
Figure labels	Temperature (°C)	log η (Pa s)	Temperature (°C)	log η (Pa s)
A-A′	1122	1.77	895	23.85
B-B′	1112	1.92	1009	3.71
C-C′	1107	2.08	1056	2.89
D-D′	1103	2.21	1092	2.51
Mixing T	1102	2.25	1102	2.44
Mutnovsky II				
A-A′	1133	1.53	926	10.46
B-B′	1123	1.91	1025	3.12
C-C′	1118	2.13	1069	2.76
D-D′	1114	2.33	1104	2.51
Mixing T	1113	2.38	1113	2.46
Mutnovsky III				
A-A′	1150	1.38	955	4.49
B-B′	1140	1.82	1044	3.06
C-C′	1135	2.08	1087	2.74
D-D′	1131	2.32	1121	2.51
Mixing T	1130	2.38	1130	2.45
Mt. Hood	Basalt		Rhyolite	
A-A′	1105	1.57	891	6.13
B-B′	1085	1.85	958	3.63
C-C′	1070	2.26	1007	3.25
D-D′	1060	2.68	1039	3.02
Mixing T	1055	2.91	1055	2.91

Note: Mt. Hood data were modeled by using the proposed mafic and felsic endmembers from Kent et al. (2010).

4.8. REFERENCES

Anderson AT (1976) Magma mixing: petrological process and volcanological tool. J Volcanol Geotherm Res 1:3–33. doi: 10.1016/0377-0273(76)90016-0

Annen C (2011) Implications of incremental emplacement of magma bodies for magma differentiation, thermal aureole dimensions and plutonism–volcanism relationships. Tectonophysics 500:3–10. doi: 10.1016/j.tecto.2009.04.010

Annen C, Blundy JD, Sparks RSJ (2006a) The Genesis of Intermediate and Silicic Magmas in Deep Crustal Hot Zones. J Petrol 47:505–539. doi: 10.1093/petrology/egi084

Annen C, Blundy JD, Sparks RSJ (2006b) The sources of granitic melt in Deep Hot Zones. Trans R Soc Edinb Earth Sci 97:297–309. doi: 10.1017/S0263593300001462

Annen C, Pichavant M, Bachmann O, Burgisser A (2008) Conditions for the growth of a long-lived shallow crustal magma chamber below Mount Pelee volcano (Martinique, Lesser Antilles Arc). J Geophys Res 113:B07209. doi: 10.1029/2007JB005049

Cooper KM, Kent AJR (2014) Rapid remobilization of magmatic crystals kept in cold storage. Nature 506:480–3. doi: 10.1038/nature12991

Ghiorso M, Sack R (1995) Chemical mass transfer in magmatic processes IV. A revised and internally consistent thermodynamic model for the interpolation and extrapolation of liquid-solid equilibria in magmatic systems at elevated temperatures and pressures. Contrib to Mineral Petrol 119:197–212.

Ghiorso MS, Evans BW (2008) Thermodynamics of Rhombohedral Oxide Solid Solutions and a Revision of the FE-TI Two-Oxide Geothermometer and Oxygen-Barometer. Am J Sci 308:957–1039. doi: 10.2475/09.2008.01

Gualda GAR, Ghiorso MS, Lemons R V., Carley TL (2012) Rhyolite-MELTS: A modified calibration of MELTS optimized for silica-rich, fluid-bearing magmatic systems. J Petrol 53:875–890. doi: 10.1093/petrology/egr080

Hui H, Zhang Y (2007) Toward a general viscosity equation for natural anhydrous and hydrous silicate melts. Geochim Cosmochim Acta 71:403–416. doi: 10.1016/j.gca.2006.09.003

Kent AJR, Darr C, Koleszar AM, et al (2010) Preferential eruption of andesitic magmas through recharge filtering. Nat Geosci 3:631–636. doi: 10.1038/ngeo924

Lange RA, Frey HM, Hector J (2009) A thermodynamic model for the plagioclase-liquid hygrometer/thermometer. Am Mineral 94:494–506. doi: 10.2138/am.2009.3011

Laumonier M, Scaillet B, Arbaret L, Champallier R (2014a) Experimental simulation of magma mixing at high pressure. Lithos 196-197:281–300. doi: 10.1016/j.lithos.2014.02.016

Laumonier M, Scaillet B, Pichavant M, et al (2014b) On the conditions of magma mixing and its bearing on andesite production in the crust. Nat Commun 5:1–12. doi: 10.1038/ncomms6607

Marsh B (1981) On the crystallinity, probability of occurrence, and rheology of lava and magma. Contrib to Mineral Petrol 78:85–98.

Marsh B (1984) Mechanics and energetics of magma formation and ascension. In: Boyd FR (ed) Explos. Volcanism Inception, Evol. Hazards. National Academy Press, Washington, D. C., pp 67–83

Robertson K, Simon a., Pettke T, et al (2013) Melt inclusion evidence for magma evolution at Mutnovsky volcano, Kamchatka. Geofluids 13:421–439. doi: 10.1111/gfl.12060

Robertson KL (2011) Magma Chamber Processes at Mutnovsky Volcano, Russia. University of Nevada, Las Vegas

Roscoe R (1952) The viscosity of suspensions of rigid spheres. Br J Appl Phys 3:267–269.

Scaillet B, Laumonier M, Arbaret L, Champallier R (2013) Magma Mixing in Arc Contexts. Abstr. V52B-08 Present. 2013 Fall Meet. AGU, San Fr. Calif., 9-13 Dec.

Selyangin O (1993) Mutnovsky Volcano, Kamchatka: New Evidence on Structure, Evolution, and Future Activity. Volcanol Seismol 15:17–38.

Shaw HR (1972) Viscosities of magmatic silicate liquids; an empirical method of prediction. Am J Sci 272:870–893. doi: 10.2475/ajs.272.9.870

Shaw HR (1980) The fracture mechanisms of magma transport from the mantle to the surface. Phys. Magmat. Process.

Simon A, Yogodzinski GM, Robertson K, et al (2014) Evolution and genesis of volcanic rocks from Mutnovsky Volcano, Kamchatka. J Volcanol Geotherm Res 286:116–137. doi: 10.1016/j.jvolgeores.2014.09.003

Smith PM, Asimow PD (2005) Adiabat_1ph: A new public front-end to the MELTS, pMELTS, and pHMELTS models. Geochemistry, Geophys Geosystems. doi: 10.1029/2004GC000816

Sparks RSJ, Marshall L (1986) Thermal and mechanical constraints on mixing between mafic and silicic magmas. J Volcanol Geotherm … 29:99–124.

Tsuchiyama A (1985) Dissolution kinetics of plagioclase in the melt of the system diopside-albite-anorthite, and origin of dusty plagioclase in andesites. Contrib to Mineral Petrol 89:1–16.

Van der Molen I, Paterson MS (1979) Contributions to Mineralogy and Experimental Deformation of Partially-Melted Granite. Contrib to Mineral Petrol 70:299–318.

CHAPTER V

CONCLUSIONS

Sorby (1858) suggested that the investigation of the minute can be just as informative of large scale processes as observations in the field. With the refinement of analytical techniques and the development of new technologies such as the field emission source for electron microscopy, NanoSIMS, and atom probe tomography, we find a whole new wealth of nanometer-scale information directly relating back to large scale petrogenetic processes. Our ability to tie together the smallest of observations with millimeter-, meter-, and kilometer-scale observations is crucial in furthering our understanding of the origin of rocks, from the mantle to the crust. The goal of the chapters presented in this dissertation is to use new melt inclusion and phenocryst data to better understand magmatic processes during rifting and subduction, and ultimately, to apply these finding to larger questions in igneous petrogenesis.

The investigation of olivine-hosted melt inclusions in **Chapter II** showed volatile enrichments much greater than would be expected in a plume or rift environment, trace-elements concentrations that looked less like OIB sources and more like the same rock type erupted in arc settings, and were enriched in fluid-mobile elements often used as slab fluid tracers. We highlighted that this subduction-like signature may have been caused by lithospheric modification during Pan-African subduction at ~600 Ma, but emphasize that our data is by no means a smoking gun. While similar to what would be expected in subduction zones, we cannot demonstrate that these findings are inconsistent with mantle modification by low-degree partial melts caused by extension, or low-degree partial melts caused by plume ascension. An

investigation of mantle xenoliths found in the area may shed more light into the source of lithospheric modification in the East African mantle. Understanding the source of these volatile-rich mantle metasomes will add to our growing understanding of where volatiles reside in the mantle, where they came from, and how they are stored.

The work in **Chapter III** and **Chapter IV** focuses on Mutnovsky Volcano, a stratovolcano in southern Kamchatka with four super-imposed eruptive centers. The overlapping eruptive centers provide the ideal opportunity for combining melt inclusion data, mineral chemistry, mineral textures, and whole-rock compositions to elucidate magma chamber processes resulting in the formation of intermediate lavas. Plagioclase phenocryst compositions measured in Mutnovsky basalts, basaltic andesites, and dacites generally described two chemical populations, a high-anorthite population and a low-anorthite population. The basalts host a high-An population, dacites a low-An population, and the basaltic andesites contain both populations, with a compositional gap between them. All plagioclase observed were euhedral crystals except for those in the low-An population of the basaltic andesites, which were partially resorbed. We emphasize that this cannot be explained by degassing, crystal fractionation, or magma recharge, and is only consistent with mixing. Microlite compositions more An-rich than the low-An phenocryst population in some of the basaltic andesites is also indicative of mixing. These finding are also consistent with melt inclusion evidence and geochemical models of magma mixing at Mutnovsky, suggesting that intermediate lavas at Mutnovsky are primarily generated through the mixing of a basaltic and dacitic magmas.

The work presented in **Chapter IV** brings new data, new models, and the advances in computational thermodynamics to an old problem, understanding the conditions at which magmas can mix. We demonstrate that the MELTS program (Ghiorso and Sack 1995) provides

quantitative constraints for the melt composition, viscosity, crystallinity, and heat capacity of magma over any range of temperatures, improving upon the constraints used in the seminal work of Sparks and Marshall (1986). These data can then be directly used to investigate the ability of thermally and compositionally distinct magmas to mix. When applied to lavas erupted at Mutnovsky we observe that the range of temperatures at which a basalt and a dacite could physically mix is consistent with the two-pyroxene temperatures of Mutnovsky basalts and dacites. We then demonstrate the broader applicability of this model by applying it to previously published data from Mt. Hood, Oregon (Kent et al 2010), where the endmembers mixed are estimated, not observed. We find our model results are similar to their proposed temperatures and volumes of mixing, but that other processes may also be at play, such as crystal fractionation.

This body of work, while varied in tectonic setting, scope, and technique, show that there is almost always a wealth of information to be found by using microanalytical techniques, and that these minute data can be readily interpreted with investigations into kilometer-scale processes. Each chapter addresses some larger fundamental questions regarding igneous processes, from the generation of mantle metasomes and their ability to store volatiles in the mantle to questions concerning the origin of intermediate lavas. Ultimately, the results of this work does not solve any of these questions, in fact this work raises many more.

REFERENCES

Ghiorso M, Sack R (1995) Chemical mass transfer in magmatic processes IV. A revised and internally consistent thermodynamic model for the interpolation and extrapolation of liquid-solid equilibria in magmatic systems at elevated temperatures and pressures. Contrib to Mineral Petrol 119:197–212.

Kent AJR, Darr C, Koleszar AM, et al (2010) Preferential eruption of andesitic magmas through recharge filtering. Nat Geosci 3:631–636. doi: 10.1038/ngeo924

Sorby HC (1858) On the Microscopical Structure of Crystals, indicating the Origin of Minerals and Rocks. Q J Geol Soc London 14:453–500.

Sparks RSJ, Marshall L (1986) Thermal and mechanical constraints on mixing between mafic and silicic magmas. J Volcanol Geotherm … 29:99–124.

APPENDIX A

Table A1 Average compositions of Fe-Ti oxides from the East African Rift

Sample	08WR-7	08WR-8	08WR-16	08WR-20
Phase	ilmenite	ilmenite	ilmenite	ilmenite
No. of analyses	2	2	2	13
SiO_2	0.89	0.17	2.00	0.05
TiO_2	47.93	49.27	47.46	48.88
Al_2O_3	0.75	0.17	0.69	0.33
Fe_2O_3	11.82	7.30	7.54	10.53
V_2O_3	0.35	0.46	0.54	0.53
Cr_2O_3	0.03	0.12	0.23	0.06
FeO	31.84	36.82	35.07	34.37
MnO	0.85	0.85	0.71	0.56
MgO	3.06	2.48	2.52	3.28
CaO	1.44	0.29	0.26	0.26
Total	98.95	97.94	97.02	98.85
$X_{ilmenite}$	75.9	81.8	81.7	76.8
$\pm 1\sigma$ $X_{ilmenite}$	9.9	1.6	1.4	4.8
Phase	magnetite	magnetite	magnetite	magnetite
No. of analyses	34	15	6	20
SiO_2	0.16	0.16	0.17	0.10
TiO_2	26.24	19.96	22.64	23.40
Al_2O_3	2.99	4.90	4.24	3.18
Fe_2O_3	14.55	18.91	21.16	19.11
V_2O_3	0.53	0.41	0.53	0.92
Cr_2O_3	0.84	6.17	0.08	0.75
FeO	49.97	43.96	45.16	47.89
MnO	0.73	0.75	0.73	0.55
MgO	2.79	2.70	3.82	2.49
CaO	0.23	0.35	0.24	0.21
Total	99.02	98.27	98.77	98.60
$X_{ulvospinel}$	72.0	54.9	61.6	64.7
$\pm 1\sigma$ $X_{ulvospinel}$	3.2	9.4	3.1	2.8
T(°C) $\pm 1\sigma$	959 ± 36	954 ± 29	896 ± 33	1024 ± 49
ΔNNO $\pm 1\sigma$	-1.8 ± 0.1	-1.2 ± 0.2	-1.4 ± 0.02	-1.0 ± 0.2

Table A2 Titanomagnetite compositions from the East African Rift

	SiO_2	TiO_2	Al_2O_3	Fe_2O_3	V_2O_3	Cr_2O_3	FeO	MnO	MgO	CaO	Total
08WR-7-1	0.13	24.51	4.70	14.63	0.68	2.39	48.15	0.55	3.75	0.07	99.57
08WR-7-2	0.14	26.84	1.76	14.71	0.35	0.16	50.78	0.74	2.18	0.25	97.91
08WR-7-3	0.14	26.52	2.50	15.02	0.37	0.19	50.57	0.84	2.35	0.24	98.73
08WR-7-4	0.22	27.03	2.31	13.13	0.40	0.46	51.09	0.73	2.06	0.31	97.76
08WR-7-5	0.17	26.98	2.52	12.94	0.53	0.83	50.94	0.79	2.35	0.24	98.29
08WR-7-6	0.09	27.01	2.62	14.19	0.47	0.82	50.77	0.73	2.81	0.22	99.74
08WR-7-7	0.10	26.35	3.01	14.52	0.57	0.94	51.00	0.73	2.59	0.13	99.96
08WR-7-8	0.08	26.12	3.47	14.65	0.59	1.11	49.76	0.62	3.28	0.16	99.83
08WR-7-9	0.09	25.49	3.77	14.76	0.67	1.39	49.40	0.68	3.20	0.11	99.56
08WR-7-10	0.10	23.35	4.90	17.16	0.75	2.41	45.21	0.53	4.74	0.14	99.30
08WR-7-11	0.16	26.21	2.36	15.23	0.51	0.44	50.04	0.82	2.34	0.28	98.40
08WR-7-12	0.11	25.70	2.63	16.28	0.50	0.75	49.20	0.81	2.58	0.33	98.87
08WR-7-13	0.12	26.55	2.28	15.48	0.42	0.39	49.73	0.75	2.77	0.31	98.78
08WR-7-14	0.26	26.22	2.26	15.25	0.43	0.27	50.04	0.83	2.00	0.42	97.98
08WR-7-15	0.09	26.63	3.12	13.19	0.57	0.94	49.68	0.58	3.34	0.15	98.28
08WR-7-16	0.11	26.39	3.28	13.28	0.72	1.41	49.89	0.75	3.41	0.06	99.31
08WR-7-17	0.15	28.22	2.09	11.50	0.36	0.14	52.55	0.80	1.74	0.30	97.84
08WR-7-18	0.08	25.45	3.51	15.40	0.55	1.19	48.92	0.69	2.91	0.27	98.96
08WR-7-19	0.15	26.03	2.69	15.35	0.47	0.83	49.65	0.72	2.59	0.32	98.79
08WR-7-20	0.08	26.23	2.92	15.18	0.62	1.07	49.68	0.83	2.57	0.38	99.56
08WR-7-21	0.06	25.80	2.71	16.07	0.55	0.63	49.26	0.75	2.82	0.23	98.88
08WR-7-22	0.66	26.21	2.68	14.26	0.45	0.35	50.05	0.81	2.57	0.38	98.43
08WR-7-23	0.06	25.52	3.61	15.33	0.61	1.02	49.52	0.62	3.12	0.11	99.53
08WR-7-24	0.09	27.47	2.62	13.01	0.50	0.62	51.48	0.75	2.71	0.15	99.41
08WR-7-25	0.03	26.05	3.26	15.71	0.61	0.84	49.23	0.63	3.57	0.14	100.07
08WR-7-26	0.04	26.09	2.92	15.93	0.52	0.61	49.52	0.80	2.64	0.34	99.41
08WR-7-27	0.13	26.25	2.88	15.00	0.55	0.74	49.71	0.75	2.65	0.34	98.98
08WR-7-28	0.09	27.37	2.79	12.59	0.52	0.70	50.82	0.68	2.88	0.19	98.63
08WR-7-29	0.28	26.43	3.17	13.25	0.57	0.73	50.36	0.77	2.68	0.22	98.46
08WR-7-30	0.49	27.02	3.31	11.15	0.52	0.88	51.88	0.68	2.58	0.12	98.63
08WR-7-31	0.16	26.24	2.63	14.83	0.48	0.72	50.84	0.86	2.08	0.25	99.09
08WR-7-32	0.12	25.52	3.60	15.73	0.59	1.16	48.97	0.73	3.39	0.17	99.98
08WR-7-33	0.08	27.33	2.44	13.65	0.42	0.18	52.15	0.73	2.01	0.20	99.20
08WR-7-34	0.44	24.88	4.37	16.28	0.68	1.10	47.97	0.63	3.76	0.34	100.44
08WR-8-1	0.17	20.74	4.55	18.33	0.46	4.84	44.74	0.77	2.60	0.30	97.50
08WR-8-2	0.19	22.69	3.82	19.86	0.48	0.96	46.84	0.76	2.54	0.28	98.41
08WR-8-3	0.26	22.62	3.72	19.52	0.47	1.88	46.35	0.86	2.32	0.48	98.49
08WR-8-4	0.22	20.55	4.20	20.22	0.50	4.11	45.14	0.73	2.29	0.34	98.30
08WR-8-5	0.12	14.62	7.68	16.61	0.33	15.94	39.10	0.69	3.16	0.34	98.60
08WR-8-6	0.10	13.09	7.74	16.09	0.36	18.45	37.71	0.66	2.91	0.35	97.46

08WR-8-7	0.15	22.40	3.91	18.95	0.44	2.66	46.45	0.76	2.30	0.41	98.42
08WR-8-8	0.12	15.99	6.55	18.01	0.38	12.82	40.36	0.66	3.16	0.26	98.32
08WR-8-9	0.14	20.03	4.71	20.03	0.30	5.53	43.18	0.79	3.04	0.40	98.14
08WR-8-10	0.20	21.46	4.03	21.40	0.42	2.03	45.13	0.70	2.57	0.45	98.40
08WR-8-11	0.08	18.20	5.60	19.14	0.42	9.04	42.17	0.81	2.90	0.35	98.70
08WR-8-12	0.22	21.34	4.35	18.91	0.43	4.13	45.82	0.77	2.35	0.37	98.69
08WR-8-13	0.08	18.75	5.05	19.92	0.34	7.80	42.39	0.72	3.07	0.33	98.45
08WR-8-14	0.13	22.13	3.99	19.65	0.39	2.31	46.10	0.86	2.40	0.35	98.30
08WR-8-15	0.16	24.81	3.52	17.05	0.46	0.02	47.96	0.70	2.89	0.31	97.88
08WR-16-1	0.12	21.58	3.96	23.90	0.64	0.14	43.86	0.72	4.17	0.19	99.28
08WR-16-2	0.21	21.33	4.99	22.34	0.62	0.18	44.29	0.74	3.76	0.21	98.66
08WR-16-3	0.19	22.51	4.16	20.73	0.58	0.01	45.09	0.75	3.47	0.28	97.76
08WR-16-4	0.11	23.55	4.49	18.46	0.59	0.10	46.73	0.79	3.02	0.29	98.14
08WR-16-5	0.24	24.13	3.94	19.35	0.22	0.00	46.02	0.73	3.93	0.35	98.92
08WR-16-6	0.14	22.77	3.92	22.17	0.51	0.08	44.95	0.65	4.58	0.10	99.87
08WR-20-1	0.08	22.27	2.72	21.55	0.59	0.04	48.86	0.68	0.95	0.18	97.93
08WR-20-2	0.12	22.79	2.43	20.52	0.64	0.06	48.95	0.58	1.48	0.08	97.64
08WR-20-3	0.08	22.85	2.68	20.85	0.79	0.43	48.89	0.66	1.66	0.12	99.01
08WR-20-4	0.10	24.39	2.33	17.07	0.80	0.76	50.05	0.51	1.82	0.07	97.89
08WR-20-5	0.11	22.87	3.87	25.38	1.07	0.41	37.22	0.44	3.93	2.26	97.56
08WR-20-6	0.11	25.21	2.99	16.10	0.80	0.42	49.59	0.54	2.16	0.31	98.23
08WR-20-7	0.09	24.32	4.11	15.48	1.05	0.71	49.06	0.52	2.23	0.22	97.79
08WR-20-8	0.13	20.83	2.54	24.16	0.59	0.07	47.22	0.68	1.40	0.07	97.68
08WR-20-9	0.15	22.74	2.57	21.11	0.57	0.09	49.29	0.58	1.43	0.09	98.62
08WR-20-10	0.10	22.99	4.12	18.49	1.14	1.99	46.35	0.53	4.07	0.03	99.82
08WR-20-11	0.07	23.51	3.91	17.56	1.16	2.00	47.25	0.44	3.88	0.00	99.79
08WR-20-12	0.19	23.61	3.34	17.29	1.14	1.67	48.52	0.53	2.99	0.00	99.28
08WR-20-13	0.01	23.24	3.41	18.69	1.13	1.65	47.63	0.48	3.23	0.02	99.49
08WR-20-14	0.11	24.55	2.68	16.38	0.96	0.86	49.36	0.56	2.42	0.06	97.94
08WR-20-15	0.05	23.78	3.90	18.40	1.20	0.40	47.35	0.52	3.31	0.18	99.11
08WR-20-16	0.10	23.55	3.90	19.00	1.13	0.42	47.09	0.58	3.34	0.20	99.29
08WR-20-17	0.14	22.30	3.07	20.99	0.92	0.60	48.13	0.51	2.03	0.10	98.78
08WR-20-18	0.10	24.98	2.33	16.74	0.77	0.53	50.45	0.60	1.90	0.11	98.51
08WR-20-19	0.10	23.31	3.11	18.73	0.85	0.67	48.50	0.55	2.06	0.15	98.03
08WR-20-20	0.09	23.89	3.63	17.73	1.13	1.15	48.00	0.53	3.41	0.04	99.60

Analytical methods for these data are the same as those described in Chapter 3.4.1

Table A3 Ilmenite compositions from the East African Rift

	SiO_2	TiO_2	Al_2O_3	Fe_2O_3	V_2O_3	Cr_2O_3	FeO	MnO	MgO	CaO	Total
08WR-7-1	1.64	46.06	1.34	16.91	0.30	0.03	26.03	0.75	3.82	2.54	99.41
08WR-7-2	0.14	49.80	0.16	6.73	0.40	0.04	37.65	0.95	2.30	0.33	98.49
08WR-8-1	0.21	48.74	0.18	7.88	0.53	0.21	36.00	0.75	2.67	0.25	97.40
08WR-8-2	0.14	49.80	0.16	6.73	0.40	0.04	37.65	0.95	2.30	0.33	98.49
08WR-16-1	0.21	48.74	0.18	7.88	0.53	0.21	36.00	0.75	2.67	0.25	97.40
08WR-16-2	3.79	46.19	1.21	7.20	0.55	0.25	34.15	0.67	2.37	0.27	96.65
08WR-20-1	0.02	50.34	0.56	12.72	0.60	0.10	28.63	0.47	6.76	0.05	100.25
08WR-20-2	0.09	48.74	0.36	10.88	0.46	0.05	34.99	0.58	2.86	0.35	99.35
08WR-20-3	0.04	48.81	0.28	10.43	0.55	0.05	35.70	0.60	2.56	0.23	99.25
08WR-20-4	0.06	48.42	0.33	10.52	0.51	0.05	35.31	0.57	2.65	0.12	98.54
08WR-20-5	0.06	48.85	0.36	10.33	0.52	0.04	34.31	0.59	3.29	0.18	98.52
08WR-20-6	0.04	48.67	0.34	10.92	0.53	0.10	34.59	0.50	2.97	0.36	99.03
08WR-20-7	0.10	48.51	0.38	11.50	0.56	0.07	33.23	0.55	3.34	0.63	98.86
08WR-20-8	0.01	49.25	0.29	9.30	0.60	0.08	35.49	0.56	2.92	0.08	98.57
08WR-20-9	0.06	48.62	0.35	10.39	0.52	0.05	34.62	0.58	2.92	0.31	98.42
08WR-20-10	0.07	49.68	0.41	11.18	0.56	0.03	31.84	0.52	4.83	0.37	99.46
08WR-20-11	0.09	48.55	0.19	8.86	0.37	0.01	37.01	0.63	2.24	0.22	98.17
08WR-20-12	0.05	48.23	0.24	10.67	0.63	0.10	34.74	0.49	2.79	0.31	98.25
08WR-20-13	0.02	48.80	0.19	9.21	0.51	0.09	36.36	0.61	2.50	0.15	98.44

Analytical methods for these data are the same as those described in Chapter 3.4.1

APPENDIX B

Table B1 Mutnovsky magnetite compositions

Magnetite	SiO_2	TiO_2	Al_2O_3	Fe_2O_3	V_2O_3	Cr_2O_3	FeO	MnO	MgO	CaO	Total
CM-47-1	0.15	15.47	1.75	36.76	0.74	0.01	43.44	0.57	1.24	0.02	100.14
CM-47-2	0.09	15.50	1.72	36.85	0.75	0.02	43.30	0.63	1.24	0.02	100.12
CM-47-3	0.10	15.17	1.78	37.23	0.85	0.02	43.08	0.61	1.21	0.02	100.06
CM-47-4	0.17	13.84	1.95	39.07	0.77	0.06	41.67	0.56	1.23	0.04	99.35
CM-47-5	0.16	17.62	1.47	32.12	0.52	0.01	44.54	0.67	1.33	0.04	98.47
CM-47-6	0.16	14.45	1.81	38.49	0.76	0.04	42.23	0.58	1.28	0.05	99.85
CM-47-7	0.13	12.42	2.58	41.78	0.72	0.02	38.55	0.51	2.35	0.07	99.14
CM-47-8	0.13	13.89	2.41	39.08	0.76	0.03	41.74	0.56	1.43	0.02	100.04
CM-47-9	0.39	17.98	1.41	31.24	0.42	0.00	45.00	0.67	1.31	0.10	98.51
CM-47-10	0.13	12.17	2.84	42.84	0.87	0.06	39.36	0.49	2.14	0.05	100.94
CM-47-11	0.10	13.52	2.63	40.11	0.78	0.05	41.05	0.49	1.85	0.00	100.57
CM-47-12	0.10	13.53	2.63	39.93	0.83	0.07	40.96	0.49	1.85	0.02	100.43
CM-47-13	0.09	13.69	2.58	39.79	0.77	0.07	41.10	0.47	1.84	0.02	100.43
CM-47-14	0.12	13.54	2.57	39.84	0.78	0.06	40.83	0.47	1.89	0.02	100.13
CM-47-15	0.14	13.73	2.44	39.56	0.77	0.04	41.42	0.52	1.62	0.02	100.27
CM-47-16	0.15	13.69	2.55	39.46	0.77	0.04	41.30	0.52	1.53	0.07	100.08
CM-47-17	0.55	16.94	1.41	35.22	0.41	0.03	39.14	0.70	1.18	1.35	96.92
CM-47-18	0.16	14.97	1.74	37.39	0.75	0.05	42.81	0.60	1.22	0.03	99.73
CM-47-19	0.12	13.55	2.30	38.52	0.77	0.04	40.93	0.52	1.43	0.00	98.18
CM-47-20	0.10	13.41	2.37	38.75	0.74	0.05	40.75	0.49	1.46	0.00	98.13
CM-47-21	0.15	13.83	2.51	39.42	0.73	0.04	42.02	0.51	1.45	0.00	100.65
CM-47-22	0.11	12.50	2.54	41.58	0.93	0.05	38.68	0.45	2.44	0.04	99.33
CM-47-23	0.12	15.00	1.93	37.76	0.68	0.04	43.06	0.59	1.23	0.02	100.42
CM-47-24	0.12	14.90	1.92	36.54	0.74	0.04	42.42	0.55	1.21	0.02	98.47
CM-47-25	0.14	14.44	1.95	38.41	0.76	0.09	42.48	0.58	1.22	0.02	100.08
CM-47-26	0.13	14.15	1.99	37.65	0.78	0.05	41.68	0.58	1.25	0.00	98.24
CM-47-27	0.30	17.29	1.38	36.50	0.48	0.00	39.15	0.67	1.28	1.43	98.48
CM-47-28	0.16	17.58	1.49	32.06	0.57	0.04	44.48	0.68	1.31	0.05	98.43
CM-47-29	0.14	15.16	1.73	36.33	0.50	0.00	42.35	0.61	1.23	0.05	98.07
CM-47-30	0.14	15.36	1.76	36.98	0.49	0.01	43.05	0.63	1.24	0.04	99.71
CM-186-1	0.13	6.12	0.71	54.35	0.75	0.10	35.25	0.50	0.05	0.16	98.12
CM-186-2	0.14	7.60	0.91	51.32	0.67	0.03	36.28	0.31	0.32	0.18	97.76
CM-186-3	0.11	7.61	0.82	51.37	0.76	0.02	36.25	0.43	0.26	0.17	97.79
CM-186-4	0.14	8.34	0.90	50.25	0.73	0.04	36.66	0.37	0.27	0.28	97.99
CM-186-5	0.14	7.70	0.70	51.43	0.84	0.02	36.80	0.51	0.09	0.15	98.36
CM-186-6	0.14	7.83	0.83	50.29	0.80	0.05	36.57	0.31	0.19	0.16	97.16
CM-186-7	0.11	9.55	0.65	47.73	0.79	0.01	38.12	0.50	0.14	0.17	97.77
CM-186-8	0.10	8.78	0.63	49.50	0.81	0.02	36.89	0.57	0.11	0.29	97.68
CM-186-9	0.14	7.31	0.81	52.09	0.74	0.05	35.98	0.43	0.18	0.22	97.97
CM-186-10	0.16	8.54	0.96	48.86	0.85	0.02	36.79	0.37	0.55	0.13	97.22
CM-186-11	0.10	6.33	0.71	53.57	0.76	0.05	35.39	0.36	0.10	0.13	97.51
CM-186-12	0.11	10.69	0.65	44.20	0.66	0.03	38.30	0.48	0.43	0.13	95.68

CM-186-13	0.10	6.96	0.73	52.82	0.71	0.02	35.86	0.37	0.17	0.17	97.90
CM-186-14	0.10	8.09	0.70	50.49	0.63	0.02	36.70	0.45	0.17	0.17	97.50
CM-186-15	0.11	8.22	0.91	49.79	0.66	0.00	36.48	0.30	0.30	0.21	96.97
CM-186-16	0.39	8.78	0.95	47.35	0.65	0.05	36.95	0.38	0.52	0.15	96.16
CM-186-17	0.13	7.87	0.85	50.67	0.74	0.04	36.76	0.45	0.20	0.13	97.85
CM-29-1	0.27	19.47	1.34	28.25	1.15	0.04	45.76	0.68	1.09	0.30	98.34
CM-29-2	0.76	18.79	1.53	28.71	1.34	0.10	46.32	0.73	1.29	0.19	99.76
CM-29-3	0.32	13.71	2.69	38.08	1.31	0.05	41.96	0.37	1.05	0.18	99.71
CM-29-4	0.51	17.11	1.58	32.30	1.32	0.08	45.40	0.52	1.09	0.09	100.00
CM-29-5	0.37	15.43	2.29	34.99	1.31	0.07	44.33	0.61	0.64	0.11	100.15
CM-29-6	0.29	16.67	1.46	34.29	1.25	0.03	44.26	0.73	1.13	0.15	100.26
CM-29-7	0.16	14.04	1.79	39.73	1.22	0.10	42.80	0.36	0.88	0.13	101.21
CM-29-8	0.30	16.43	1.83	34.50	1.07	0.06	44.23	0.52	1.26	0.12	100.32
CM-9a-1	0.16	14.28	1.80	41.24	0.57	0.04	42.23	0.62	1.68	0.06	102.67
CM-9a-2	0.18	14.18	1.78	41.18	0.57	0.04	42.19	0.58	1.70	0.04	102.44
CM-9a-3	0.21	14.34	1.93	40.62	0.54	0.03	42.52	0.52	1.53	0.08	102.33
CM-9a-4	0.14	14.48	1.96	40.93	0.62	0.02	42.82	0.54	1.57	0.06	103.14
CM-9a-5	0.08	13.46	1.74	41.51	0.55	0.07	40.69	0.49	1.88	0.02	100.49
CM-9a-6	0.31	13.65	1.86	41.46	0.55	0.07	41.38	0.50	1.79	0.09	101.66
CM-9a-7	0.26	13.76	1.92	41.39	0.53	0.04	41.26	0.53	1.84	0.10	101.64
CM-9a-8	0.27	13.60	1.91	41.46	0.55	0.06	41.17	0.55	1.83	0.08	101.48
CM-8a-1	0.43	16.68	1.65	35.00	0.38	0.01	45.25	0.62	1.09	0.06	101.17
CM-8a-2	0.37	15.05	1.52	38.63	0.35	0.04	43.56	0.65	0.91	0.15	101.22
CM-8a-3	0.33	16.08	1.61	36.80	0.42	0.03	44.96	0.70	1.01	0.03	101.96
CM-8a-4	0.63	13.82	1.53	41.20	0.14	0.00	41.88	0.68	0.78	0.41	101.06
CM-8a-5	0.36	16.39	1.75	36.56	0.35	0.00	45.08	0.67	1.11	0.09	102.37
CM-8a-6	0.32	16.95	1.64	34.11	0.31	0.00	44.85	0.71	1.15	0.06	100.08
CM-8a-7	0.23	16.68	1.68	36.41	0.36	0.01	45.49	0.67	1.09	0.03	102.64
CM-8a-8	0.34	17.34	1.62	33.30	0.33	0.04	45.39	0.71	1.15	0.03	100.25
CM-8a-9	0.20	17.59	1.67	33.24	0.37	0.01	45.20	0.65	1.35	0.04	100.32
CM-8a-10	0.26	16.82	1.71	34.59	0.39	0.02	44.77	0.62	1.34	0.01	100.53
CM-8a-11	0.43	16.63	1.52	35.77	0.42	0.00	44.38	0.63	1.36	0.17	101.30

Analytical methods for these data can be found in Chapter 3.4.1

Table B2 Mutnovsky ilmenite compositions

Ilmenite	SiO_2	TiO_2	Al_2O_3	Fe_2O_3	V_2O_3	Cr_2O_3	FeO	MnO	MgO	CaO	Total
CM-47-1	1.91	44.81	0.82	14.37	0.44	0.00	32.35	0.83	2.33	0.39	98.26
CM-47-2	0.25	44.82	0.25	21.45	0.44	0.00	25.20	0.78	1.44	7.60	102.22
CM-47-3	0.17	46.16	0.17	17.56	0.39	0.00	30.56	0.81	1.77	4.18	101.77
CM-47-4	0.15	46.11	0.15	16.85	0.21	0.05	31.99	0.49	1.25	4.44	101.69
CM-186-1	0.08	44.93	0.05	14.12	0.32	0.00	36.28	0.80	1.14	0.20	97.90
CM-186-2	0.13	45.31	0.08	13.60	0.35	0.00	36.07	0.84	1.22	0.35	97.94
CM-186-3	0.23	43.93	0.05	16.61	0.38	0.00	35.83	0.69	0.91	0.25	98.88
CM-186-4	0.08	44.27	0.04	15.92	0.46	0.04	36.38	0.66	0.63	0.18	98.66
CM-186-5	0.58	44.50	0.09	13.64	0.38	0.00	36.89	0.69	0.77	0.24	97.73
CM-186-6	0.10	43.10	0.07	16.77	0.41	0.04	35.39	0.68	0.65	0.14	97.35
CM-186-7	0.85	42.27	0.08	16.64	0.34	0.07	34.82	0.78	1.03	0.20	97.08
CM-186-8	0.08	42.18	0.05	17.25	0.38	0.00	34.76	0.57	0.66	0.17	96.10
CM-186-9	0.08	41.81	0.04	17.29	0.42	0.02	34.32	0.67	0.56	0.26	95.45
CM-186-10	0.08	44.63	0.05	15.39	0.39	0.00	37.16	0.62	0.47	0.24	99.02
CM-186-11	0.13	45.05	0.10	13.70	0.33	0.06	35.52	0.87	1.54	0.13	97.44
CM-186-12	0.20	45.05	0.06	14.17	0.40	0.03	36.27	0.75	1.15	0.20	98.30
CM-186-13	0.48	45.45	0.12	12.84	0.34	0.00	37.34	0.86	0.83	0.21	98.44
CM-29-1	0.28	49.36	0.13	11.17	0.50	0.02	36.94	0.50	2.88	0.13	101.91
CM-29-2	0.13	47.98	0.11	11.69	0.41	0.01	36.94	0.62	2.10	0.26	100.25
CM-9a-1	18.67	31.61	6.30	20.71	0.35	0.01	17.36	0.30	1.43	2.25	98.99
CM-9a-2	11.97	37.34	3.54	15.74	0.50	0.00	26.99	0.39	1.47	1.16	99.10
CM-8a-1	0.17	47.00	0.17	12.57	0.29	0.00	36.95	0.79	1.76	0.03	99.73
CM-8a-2	0.39	46.33	0.21	12.51	0.31	0.00	36.09	0.81	1.92	0.03	98.59
CM-8a-3	0.18	47.32	0.22	12.72	0.32	0.03	36.51	0.76	2.00	0.06	100.12
CM-8a-4	0.19	47.13	0.18	12.92	0.28	0.00	36.95	0.86	1.77	0.03	100.30
CM-8a-5	0.25	47.48	0.21	12.45	0.29	0.00	36.83	0.78	2.03	0.04	100.35
CM-8a-6	0.14	47.39	0.19	12.60	0.29	0.02	36.62	0.81	2.06	0.03	100.15
CM-8a-7	0.21	47.37	0.20	12.74	0.31	0.00	36.82	0.76	1.95	0.05	100.40

Analytical methods for these data can be found in Chapter 3.4.1